ELECTROMECHANICAL RESPONSE OF TEXTURED FERROELECTRIC PZT THIN FILM STACKS

BY

DEBASHISH DAS

DISSERTATION

Submitted in partial fulfillment of the requirements
for the degree of Doctor of Philosophy in Aerospace Engineering
in the Graduate College of the
University of Illinois at Urbana-Champaign, 2017

Urbana, Illinois

Doctoral Committee:

Professor Ioannis Chasiotis, Chair and Director of Research
Professor John Lambros
Professor Nancy R. Sottos
Professor Philippe H. Geubelle

ABSTRACT

Thin film piezoelectric materials with high piezoelectric coefficients such as $PbZr_{0.52}Ti_{0.48}O_3$ (PZT) offer several advantages to microelectromechanical systems (MEMS) due to their low power requirements, large displacements, high work and power densities, as well as high sensitivity in a wide dynamic range. The performance of PZT-based MEMS can be further improved by increasing the piezoelectric response of PZT polycrystals via texture control. However, freestanding PZT films, in particular for MEMS, are comprised of several other films forming a stack. These additional layers serve as seeding (TiO_2), buffer (SiO_2), and conducting (Pt) layers with substantial thickness and stiffness compared to the main PZT layer. As a result, quantitative understanding of the mechanical behavior of each layer is required in order to extract the electromechanical response of the PZT layer itself in a stack.

This dissertation research investigated (a) the mechanical behavior of highly {111} textured Pt films grown on {100}-TiO_2 which is required to achieve ~100% (001)-textured PZT films, and (b) the electromechanical behavior of freestanding textured PZT film stacks, with PZT texture varying from 100% (001) to 100% (111). PZT stacks in the form of d_{31}-type actuators were comprised of an elastic SiO_2 layer, an adhesion layer of {100}-textured rutile TiO_2, a metallization layer of highly {111}-textured Pt, a seed layer of $PbTiO_3$, the PZT layer, a second Pt metallization layer, and, finally, a thin ALD layer of Al_2O_3 and HfO_2 deposited by atomic layer deposition.

Microscale uniaxial tension tests were carried out on patterned SiO_2 films and combinations of layers, such as TiO_2-Pt, SiO_2-TiO_2-Pt, SiO_2-TiO_2-Pt-PZT and SiO_2-TiO_2-Pt-PZT-Pt-ALD to determine the properties of each layer. Experiments on TiO_2-Pt stacks with different Pt thickness showed that a reduction in film thickness increases the flow stress of Pt. The evolution of flow stress with plastic strain as a function of film thickness and grain size was successfully modeled, providing insight into the deformation behavior of polycrystalline metal films grown epitaxially on polycrystalline underlayers. Mechanical experiments on (SiO_2-TiO_2-Pt-PZT) and full PZT stacks (SiO_2-TiO_2-Pt-PZT-Pt-ALD) showed that the mechanical, piezoelectric and ferroelastic properties of PZT

thin films depend strongly on grain orientation. The open circuit PZT modulus varied linearly with %(001) and %(111) texture factors between the two texture bounds: a lower bound for 100% (001) and an upper bound for 100% (111). Pure (001) texture exhibited maximum non-linearity and ferroelastic domain switching, contrary to pure (111) texture with more linear behavior and the least amount of switching. A micromechanics model based on the Eshelby inclusion problem was employed to calculate the strain due to domain switching. The model reproduced the experimentally observed non-linearities in the stress vs. strain curves of (001) and (111) textured PZT films. Finally, the linear piezoelectric and ferroelectric properties of textured PZT films at low and high electric fields, respectively, were calculated using laser Doppler vibrometer measurements on PZT unimorphs. All samples, except one comprised of 73% (001) and 27% (111) texture, demonstrated saturation in transverse piezoelectric coefficients beyond ~150 kV/cm. Notably, the sample with the combination of 73% (001) and 27% (111) textures showed stable transverse piezoelectric coefficients at all electric field values with technologically significant implications to ultra-low-power MEMS. The ferroelectric and linear piezoelectric coefficients (with the exception of the aforementioned sample with stable linear properties) depended strongly on film texture, and the effective transverse strain and stress coefficients varied linearly with %(001) and %(111) texture factors. PZT films with 100% (001) orientation displayed 150%, 140%, and 80% larger linear piezoelectric strain coefficient, saturated strain coefficient and saturated stress coefficient, respectively, compared to films with 100% (111) orientation for the same electric bias and the same film thickness. Finally, PZT films with pure (001) texture showed 20% higher dielectric constant and 50% higher figure of merit in sensing than films with pure (111) texture.

This dissertation research provided insight into material microstructure-electromechanical property relationships for freestanding PZT film stacks. The results will assist the development of reliable low power PZT-based MEMS devices with higher actuation and better sensing characteristics.

ACKNOWLEDGEMENTS

I am grateful to my advisor, Prof. Ioannis Chasiotis, for his constant support and guidance which not only proved invaluable for the successful completion of this dissertation but also helped me develop the skill-sets in the field of nanomechanics which was initially a steep learning curve for me being from a material science background. He showed extreme patience and helped me through tough times during the completion of this dissertation research. I would also like to acknowledge the ARO grant # W911NF-12-1-0204 for supporting my research.

I would like to extend my sincere gratitude to our collaborators, Dr. Ronald Polcawich of Army Research Laboratory (ARL), Adelphi, MD for providing me the samples, providing insightful discussions and suggestions and help me carry out experiments at ARL. I am also indebted to Dr. Ryan Rudy of ARL for showing me the facilities at ARL and helping me carry out the electrical characterization of the PZT films at ARL. I will like to thank Prof. Sottos, Prof. Lambros, and Prof. Geubelle for agreeing to serve on my doctoral committee and providing invaluable feedback during my preliminary examination that was crucial to improving this dissertation.

Many thanks are due to all my present and past lab mates from Prof. Chasiotis's research group, especially Mr. Korhan Sahin, Dr. Pavan Kolluru, Dr. Sivakumar Yagnamurthy, Dr. Nikhil Karanjgaokar, Mr. Dimitrios Antartis and Mr. Fan Yang for their invaluable discussions which have always helped bring in a fresh perspective to the problems at hand.

I would like to sincerely thank the Aerospace Department staff for their constant support, especially the machine shop members Mr. Greg Milner and Mr. Lee Booher for their valuable suggestions to improve the design of parts, and to Ms. Staci McDannel and Ms. Kendra Lindsey for help with administrative issues. I also extend my thanks to the staff at Material Research Laboratory for training me on several necessary instruments, primarily to Dr. Jim Mabon for FIB and SEM training, Dr. Mauro Sardela for XRD training, and Dr. Scott Maclaren for AFM training.

I am forever grateful to my parents, my wife, Pikee Priya and my relatives for the constant encouragement, support and for believing in me. Finally, I would like to thank my friends Esperanto, Chaitanya, Shamiparna, Alok, Avinash, Anand and many others for supporting and being there for me.

TABLE OF CONTENTS

CHAPTER 1

Introduction

Microelectromechanical systems (MEMS) integrate miniaturized elements with combined mechanical and electrical functionalities via microfabrication techniques that produce typical feature sizes in the 1-100 μm range. The field of MEMS has grown significantly with the advent of modern electronics and recent advances in fabrication technologies by which both sensing and actuation elements could be realized on-chip. Motion in MEMS can be generated by different means, such as thermal, electrostatic, magnetostrictive, and piezoelectric. However, most current MEMS devices are actuated electrostatically which requires significant actuation voltage that necessitates large external sources. The alternative piezoelectric actuation, particularly based on lead zirconate titanate (PZT) films, offers several benefits, such as the unique combination of high work and power densities, superior power efficiency, and low voltage actuation. PZT thin film actuators with very high piezoelectric coefficients can achieve significant forces and structural displacements at small voltages, thus eliminating the need for bulky power conditioning circuits. PZT sensors, on the other hand, do not require external energy sources, offering the possibility of ultra-low-power miniaturized systems. PZT transduction has also been utilized for energy harvesting [1]. Other examples of PZT-MEMS devices include radio frequency (RF) switches [2], ultra-low power mechanical logic [3], inkjet printer heads [4], biosensors [5] and millimeter scale robotics [6].

The performance of PZT-MEMS devices hinges upon the piezoelectric response of the PZT films that is quantified by the piezoelectric coefficients. Epitaxial and strong-oriented piezoelectric films with a well-defined polar axis orientation may further increase the actuation force produced by PZT-based MEMS. The electromechanical

properties of PZT thin films depend on the fabrication process [7] and, thus, differ significantly from bulk PZT. The key differentiating factor of freestanding PZT thin films fabricated for MEMS devices is the significant thickness of all auxiliary films acting as electrodes or support relative to the thickness of the PZT film itself, which affects the maximum output displacement. Furthermore, epitaxial PZT films grown on silicon substrates need suitable seed and buffer layers that act as structural templates and barriers against Pb cation migration into Si. Epitaxial PZT films are usually deposited thinner than randomly oriented films since the thinner textured/epitaxial films require lower coercive voltages while displaying comparable remnant polarizations. Because of their multilayer structure, PZT films fabricated for MEMS are henceforth referred to as PZT stacks. The grain structure and texture of underlying films in a PZT stack bias and control the texture of the PZT layer itself, requiring mechanical characterization of each layer in the stack to ensure the mechanical performance and reliability of PZT-MEMS.

1.1 Motivation and Approach

Epitaxial films may be deposited with several different textures and their combinations which directly influences their piezoelectric and mechanical properties. A large number of possible textures and the difficulty in preparing and testing PZT films with different texture have limited the number of available comprehensive studies [8-14]. Even more scarce are data on freestanding PZT films. Prior studies of PZT films using uniaxial tension [15], nanoindentation [8-10], membrane deflection techniques [16,17] and resonance frequency techniques [11] have reported a broad range of values for the elastic modulus, ranging between 37 GPa [18] and 400 GPa [19]. The lack of a large and consistent base of experimental modulus data has implications in the calculation of other important properties of PZT films. For instance, determination of the piezoelectric strain coefficient, d_{31}*, requires explicit knowledge of the elastic modulus [20-22]. Inaccuracies

* Piezoelectric strain coefficient (d_{ijk}) is the linear coupling factor between polarization (P_i) and applied stress (σ_{ij}) for the direct piezoelectric effect, $P_i = d_{ijk}\sigma_{jk}$. Alternately, it is the linear coupling factor between strain (ε_{ij}) and electric field (E_i) for the converse piezoelectric effect, $\varepsilon_{ij} = d_{kij}E_k$.

in the values of the latter could be responsible for the vast disparities in the values of d_{31} reported in the literature, in the range of 30 pmV^{-1} [23] to 180 pmV^{-1} [24]. Furthermore, existing literature on PZT films with {100} or {111} preferred orientation lack quantitative texture data: for instance, the fraction of (001), (110) and (111) oriented grains or the distribution of misalignment of (001), (110) and (111) oriented grains relative to the substrate normal. Such data would allow to establish fabrication-structure-property relations and support further progress in PZT thin films.

Recently, it has been shown that large amounts of excess Pb in a $PbTiO_3$ seed layer and a highly {111} textured Pt layer grown on {100} TiO_2 promoted ~100% (001)-textured PZT films [25] with the highest reported transverse piezoelectric coefficients. However, there are no prior studies on the mechanical response of the polycrystalline Pt films grown epitaxially on polycrystalline TiO_2 seed layer resulting in grain-to-grain {111}Pt ||{100}TiO_2 heteroepitaxy. While the elastic properties of such textured Pt layers may be possible to compute fairly accurately, the inelastic behavior would depend on the interplay between film thickness, grain size, texture, the structure of the underlying layer (amorphous or polycrystalline). These factors are known to influence the mechanical behavior of epitaxially grown single crystal face-centered cubic (FCC) metal films [26] and non-epitaxial polycrystalline films deposited on amorphous deformable underlayers [27,28].

Because of its ferroelectricity, PZT displays both intrinsic and extrinsic response. The intrinsic response is associated with ionic deformation of unit cells in the crystalline material, whereas the extrinsic response is associated with the motion of non-180˚ domain walls or phase boundaries. Several studies [29-31] have demonstrated that the intrinsic response of PZT thin films depends on grain orientation. However, prior literature quantified only the extreme cases of (111), (001) or (110) film texture, leaving all intermediate cases of different textures unexplored. Moreover, the available literature data show discrepancies in the orientation dependence of piezoelectric properties, as different studies have reported an improved response for (001) [29,30], Figure 1.1(a),

{111} [32], (110), Figure 1.1(b) [33] or even randomly oriented, Figure 1.1(c) [34] PZT films near the morphotropic phase boundary (MPB[†]).

These inconclusive results are further shrouded by the fact that the majority of prior studies had examined PZT films that were bonded to thick Si substrates with various PZT thicknesses and grain sizes and without always accounting for the effect of residual stresses on the piezoelectric response, especially when those stresses were large. Significant residual stresses, on the order of several hundred MPa [35,36], develop in sol-gel derived PZT which originate from the constrained shrinkage of the wet film as it gels and dries and then pyrolyzed, densified, crystallized, and finally cooled to room temperature on a rigid substrate. Biaxial tensile residual stresses, which are most common for PZT films deposited on platinized silicon (Si-SiO_2-Ti-Pt), create an in-plane clamping effect on domains [35-37] leading to lower field-induced in-plane and out-of-plane strains, consequently altering the piezoelectric behavior, Figure 1.2(a). This is further complicated by the fact that residual stresses are closely related to the film texture. Tuttle *et al*. [38] demonstrated that the stress experienced by a PZT film during cooling through the Curie temperature, T_c[‡] controls the orientation of the domain structure. Tensile stresses during the cooling process tend to orient the polar vector approximately parallel to the substrate ("a" domain configuration), and compressive stresses tend to orient the polar vector perpendicular to the substrate ("c" domain configuration). Hence, residual stresses could be different for films with different texture that are deposited on rigid substrates, which could be the reason for the difference in reported linear and nonlinear ferroelectric properties [31,39]. PZT film thickness is another variable which affects the effective properties of films bonded to thick substrates. Thin films have higher residual stresses when compared to thicker films and show lower piezoelectric coefficients [35,39], Figure 1.2(b). Interestingly, films with different thicknesses and comparable residual stress had similar piezoelectric responses, Figure 1.2(b) [35]. This implies that

[†] Tetragonal to rhombohedral phase transition occurs at the morphotropic phase boundary (MPB) near the Zr^{+4}/Ti^{+4} ratio of 52/48.

[‡] The Curie temperature, T_c, is the temperature below which a centrosymmetric cubic crystal structure at nonpolar paraelectric state spontaneously changes to a non-centrosymmetric distorted crystal structure having a polar ferroelectric state.

the residual stress and not the film thickness controls the film's ferroelectric response. The grain size is another important parameter which might alter ferroelectric properties [31] since larger grains show more complicated domain structure within individual grains whereas smaller grains can accommodate only a limited number of domain variants. Thus, films with larger grains are less susceptible to reduction in piezoelectric response: Figure 1.2(c) shows an increase in piezoelectric properties with increased grain size of $Pb(Ni_{1/3}Nb_{2/3})O_3$ – $Pb(Zr_xTi_{1-x}O_3)$ PMN-PZT films [40], although the increase is only ~11% for ~150% increase in grain size.

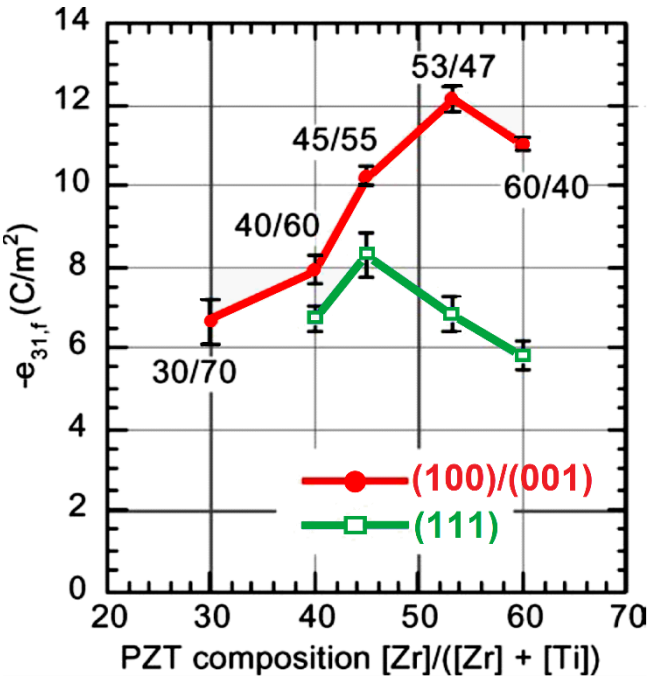

(a)

(figure continues on next page)

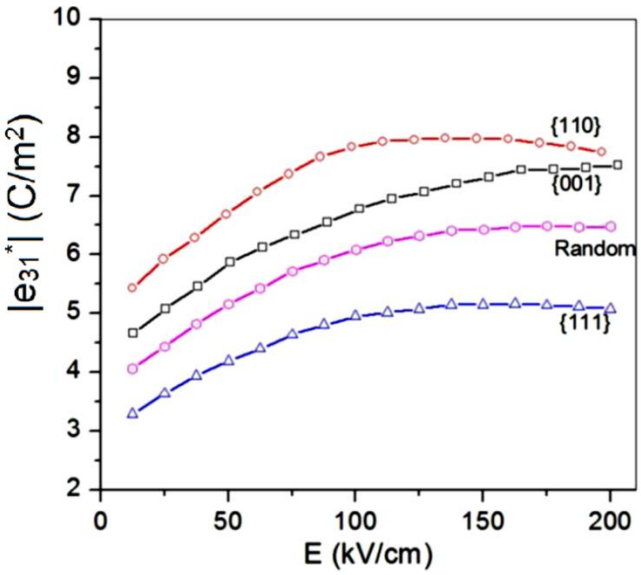

(b)

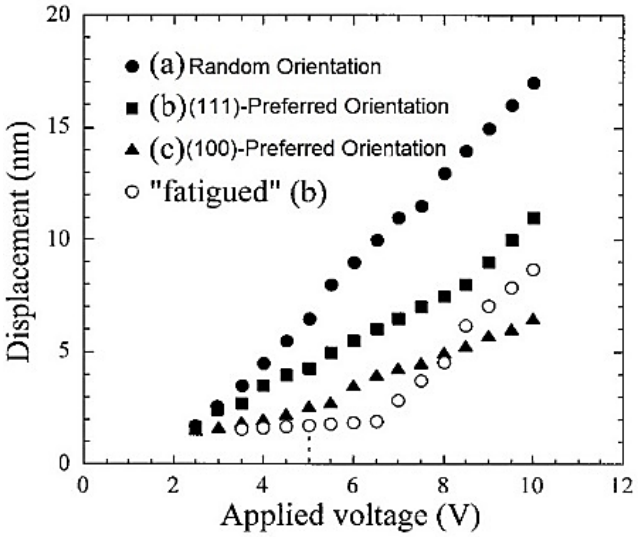

(c)

Figure 1.1 Orientation dependence of transverse piezoelectric stress coefficient, $e_{31,f}$[§] of PZT thin films showing better response from **(a)** {100} [29], **(b)** (110) [33] and **(c)** random [34] textured PZT films. Reprinted from references [29], [33] and [34] with permission from Elsevier, VBRI Press, and John Wiley and Sons, Inc, respectively.

[§] Piezoelectric stress coefficient (e_{ijk}) is the linear coupling factor between polarization (P_i) and applied strain (ε_{ij}) for the direct piezoelectric effect, i.e. $P_i = e_{ijk}\varepsilon_{jk}$. Alternately, it is the linear coupling factor between stress (σ_{ij}) and electric field (E_i) for the converse piezoelectric effect, $\sigma_{ij} = e_{kij}E_k$.

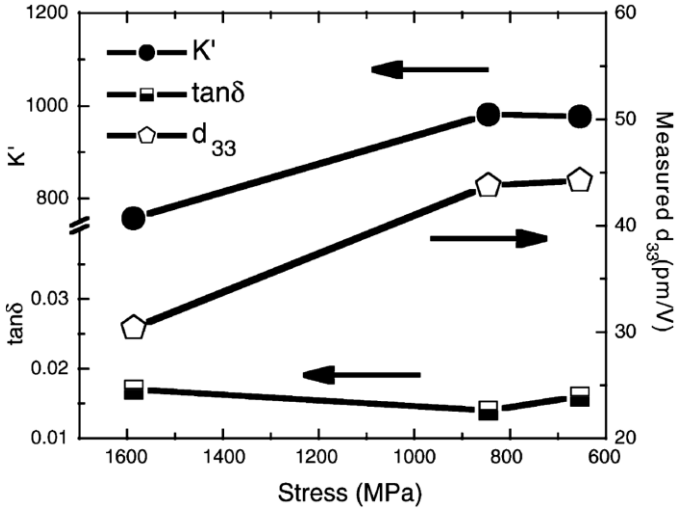

(a)

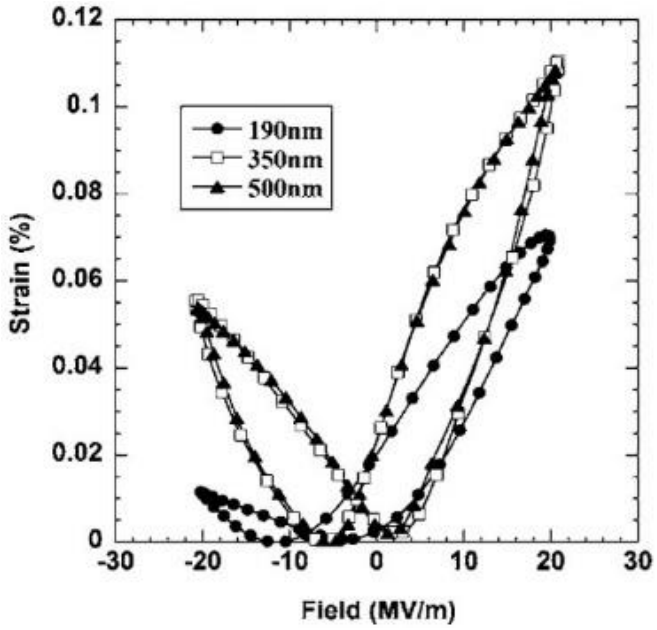

(b)

(figure continues on next page)

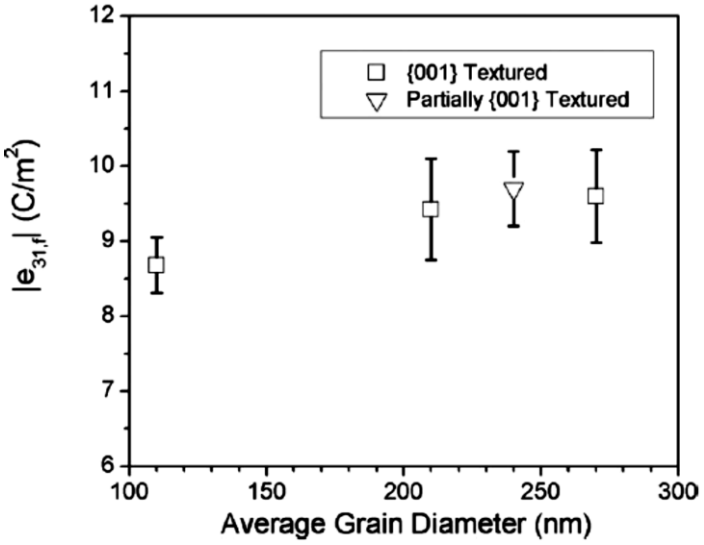

(c)

Figure 1.2 (a) Dielectric constant, dissipation factor, and piezoelectric strain coefficient as a function of residual stress: the piezoelectric and dielectric properties increase with decreasing residual stresses [36]. Reprinted with permission from Elsevier. **(b)** Effect of film thickness is shown: the thinnest film with the highest residual stress shows the minimum strain [35]. Reprinted with permission from AIP Publishing LLC. **(c)** Piezoelectric stress coefficient as a function of average grain diameter in PMN-PZT films showing an increase in $e_{31,f}$ with grain size [40]. Reprinted with permission from AIP Publishing LLC.

1.2 Structure and Recent Advances in Fabrication of PZT Films

PZT can be considered as a solid solution of $PbZrO_3$ and $PbTiO_3$ with *perovskite* crystal structure of the kind ABO_3, where A and B represent the divalent and tetravalent cations, Pb^{+2}, and Ti^{+4} or Zr^{+4}, respectively, and O represents the divalent anion, O^{2-}. PZT exists in a nonpolar paraelectric state with a centrosymmetric cubic crystal structure above the Curie temperature, T_c, of 230-490˚C [41]. At T_c, there is a structural transition to a polar ferroelectric state with a noncentrosymmetric distorted crystal structure. This distorted crystal structure, depending on the Zr^{+4}/Ti^{+4} ratio, can possess tetragonal,

rhombohedral, or monoclinic symmetry when the cubic unit cell expands along one of the 6, 8 and 12 equivalent <001>, <111> and <011> directions, respectively. These distortions induce a dipole moment as a result of the shift between the center of the negative and positive charges formed by the oxygen and the cation sublattices, respectively. Thus, spontaneous polarization along the six and eight equivalent directions in tetragonal and rhombohedral symmetry develops in each unit cell upon cooling below T_c and domain boundaries form between adjacent domains with different polarization directions. Figure 1.3(a) shows the structural changes occurring in PZT as a function of temperature and compositional variations. Tetragonal to rhombohedral shift occurs at the morphotropic phase boundary (MPB) near the Zr^{+4}/Ti^{+4} ratio of 52/48. Phase equilibrium at the MPB requires the co-existence of both tetragonal and rhombohedral structures in the region and results in an increased number, 14 of possible polarization directions. Thus, compositions near the MPB result in heightened dielectric and piezoelectric properties as shown in Figure 1.3 (b,c).

Apart from the MPB composition, it has also been recognized that controlling the crystallographic grain orientation in PZT films is critical to achieving desirable electromechanical properties [29,30] since perovskite ferroelectric materials are strongly anisotropic. However, controlling the texture and specifically achieving (001), or c-axis orientation, in PZT is not straightforward. The growth of PZT is strongly nucleation controlled [42]. The substrate structure and chemistry [43-47], thermal treatment [43,48], solution stoichiometry and content of excess lead [43,46], and chemical composition of the first monolayers [43], all play essential roles in determining thin film orientation. With so many parameters affecting texture, a textured Pt (111) electrode would be a good starting point for achieving textured PZT. PZT with a lattice constant close to Pt (2-3% mismatch [31]) would be expected to grow with an (111) orientation of Pt. However, when deposited on Pt (111), PZT can have many different orientations [43]. Aoki *et al*. [49] showed that pure Pt is not the ideal substrate to nucleate the perovskite structure because of low nucleation density and consequently high leakage currents. As a result, thin seeding layers of the type $(TiO_2)_x(PbO)_y$ have been reported [46] to yield specific PZT textures successfully. Ti-rich and TiO_2 seed layers yield (111) PZT orientation [45,46] whereas Pb-rich seed layers yield {100} PZT orientation [46] as shown in Figure

1.4(a). Two distinct regions with pure {100} phase at high PbO concentrations and (111) PZT phase at high TiO_2 concentrations are separated by a narrow region of random PZT growth. It is thought that excess PbO is needed to nucleate (100) textured $PbTiO_3$ which has a lower surface energy with the PbO nuclei [46] and subsequently {100} textured PZT grows on top of (100) textured $PbTiO_3$. Chen *et al*. [43] showed that the formation of PbO requires Pb excess because the driving force for PbO formation decreases as the amount of Pb excess is reduced. Figure 1.4(b) shows that PZT {100} is more favored by an excess Pb composition consistent with this idea.

There have been many literature accounts [33,43-48,50,51] on processing, microstructure and electromechanical properties of PZT thin films. Recent focus has been on orientation control and, in turn, the piezoelectric and dielectric properties [33,44-46,51]. A recently patented microfabrication process [25] allows for the fabrication of PZT layers with the ability to control texture from 100% (001) texture to 100% (111) texture as well as various combinations of the two textures.

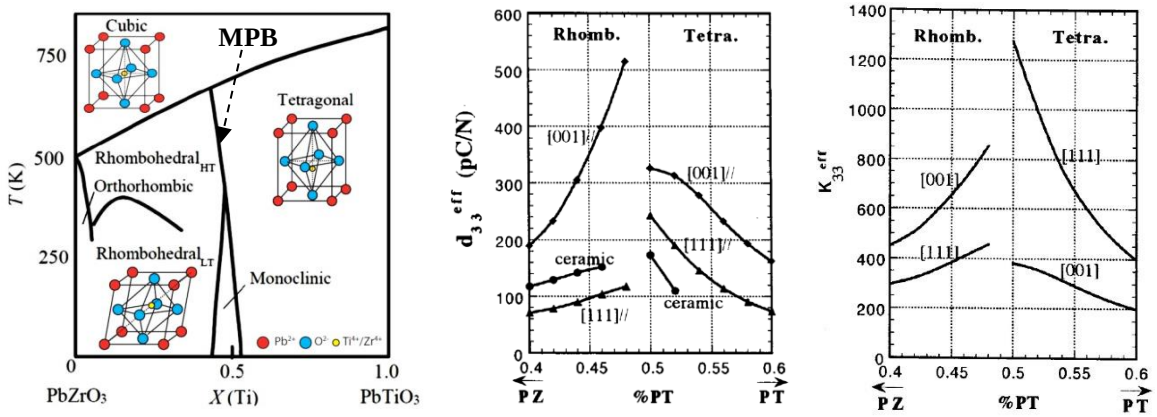

Figure 1.3 (a) Phase diagram for $PbZrO_3$-$PbTiO_3$ solid solution showing the MPB composition at a Zr^{+4}/Ti^{+4} ratio of 52/48. Figure adapted from [52] **(b,c)** Effective piezoelectric strain coefficient, d_{33} and dielectric constant, K_{33}, of PZT, respectively, vs. composition showing a maximum at the MPB [30]. Reprinted with permission from AIP Publishing LLC.

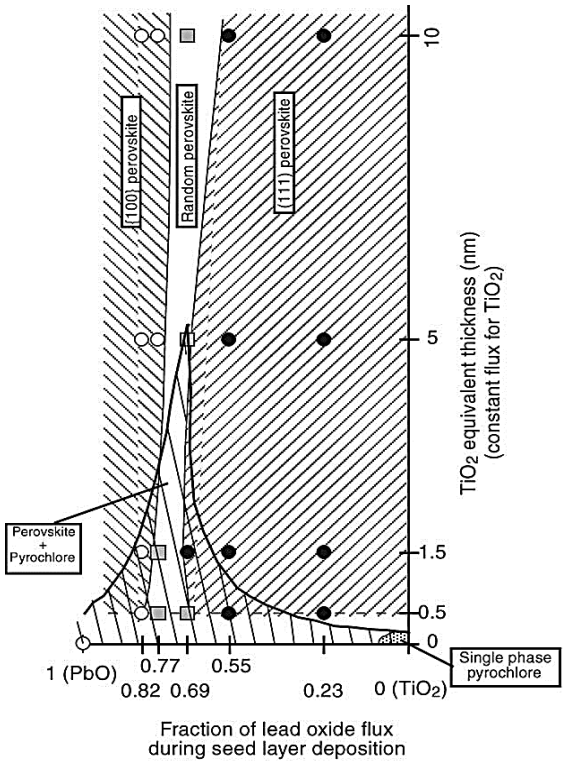

(a)

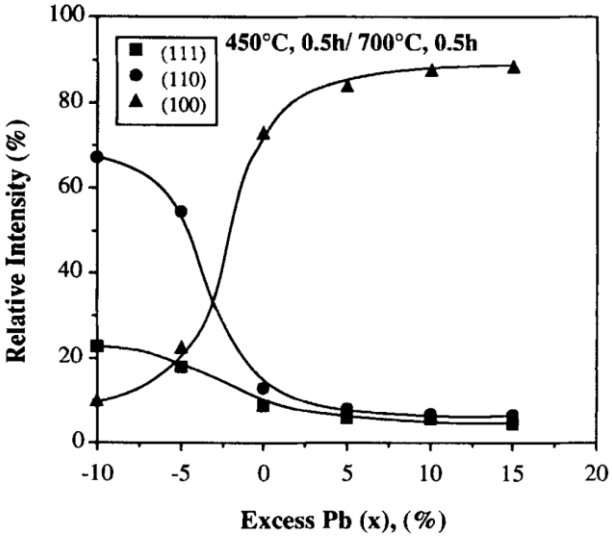

(b)

Figure 1.4 (a) PZT texture as a function of seed layer composition and thickness [46]. Reprinted with permission from Elsevier. **(b)** Effect of Pb-excess on (111), (110) and (100) PZT textures [43]. Reprinted with permission from John Wiley and Sons, Inc.

The use of a highly {111}-textured Pt layer grown on {100}-TiO_2 and a $PbTiO_3$ (PTO) seed layer played a significant role in improving the PZT orientation. This improvement was not possible with Ti-Pt layers alone [44] which were used in numerous previous studies [8,15,53]. It was even shown that the PZT deposited on TiO_2-Pt-PTO showed an increase in {100} Lotgering factor** by ~15% when compared to the one deposited on Ti-Pt-PTO [44]. Experiments further revealed that varying the amount of excess lead in the PTO seed layer controlled the PZT texture, with 30% Pb-excess giving rise to ~100% (001) texture which is of major technological importance.

1.3 Mechanical Behavior of Textured Thin Films

The elastic and inelastic mechanical response of the top and bottom thin film Pt electrodes in the aforementioned PZT stacks needs to be quantified in order to deduce the mechanical behavior of PZT films inside the stacks. Both Pt electrodes are comprised of textured Pt grown on an underlying textured ceramic polycrystal. This microstructure requires special considerations in understanding the initiation and evolution of inelastic deformation in Pt films, especially the scaling of inelastic properties with the coupled role of Pt film thickness and grain size.

The mechanical behavior of metallic thin films depends on a variety of factors, such as texture [28], grain size and film thickness [27], the structure of the underlying layer [26], etc. Of primary importance in determining the structure and, in turn, the mechanical properties of metallic films are the film thickness and the structure of the underlying layer. These parameters can be controlled during film deposition. For metallic films deposited on substrates, the flow stress has been shown to increase with decreasing film thickness, and mechanistic models have been developed to explain this inverse dependence. For example, based on the threading dislocation concept by Freund for single crystal films bonded to a substrate with some mismatch strain [54], Nix [55] developed a quantitative model considering film/substrate interface acting as an

** Lotgering Factor provides an estimate of the degree of orientation in a textured material, a value of 0 indicates random, non-oriented sample and a value of 1 represents a fully oriented sample.

impenetrable obstacle to dislocation motion, thus, necessitating the deposition of misfit dislocations at the interface. Later, Thompson [56] extended the Nix-Freund model to polycrystalline films with grain diameters that are at least twice the film thickness by including grain boundaries (GBs) as additional obstacles to dislocation motion. Blanckenhagen *et al*. used dislocation dynamics [57] to model the flow stress in thin films by considering dislocation sources in non-epitaxial polycrystalline metal films to be rare and, therefore, Frank-Read sources inside grains requiring to operate several times to generate more dislocations to achieve the imposed deformation. This approach successfully modeled the flow stress vs. film thickness in non-epitaxial polycrystalline metal films deposited on amorphous and deformable substrates, whereas the approach by Nix and Freund was found to be better suited in modeling the flow stress in epitaxial single crystal thin films.

In-situ TEM studies of thermally strained and epitaxially grown single crystal Al [58] and Cu films [26] on (0001) α-Al_2O_3 substrates revealed the motion of threading dislocations on inclined {111} planes with eventual deposition of interfacial dislocation segments at Al/α-Al_2O_3 and Cu/α-Al_2O_3 interfaces. It was further observed, Figure 1.5, that epitaxial film-substrate interfaces act as dislocation sources, and dislocation half-loops are emitted from the interfacial dislocation network. In contrast, no such phenomena were observed in polycrystalline Al and Cu films deposited on amorphous oxide or nitride layers on Si substrates. The amorphous underlayers did not promote the formation of stable interfacial dislocation networks because they permitted atomic rearrangements that allowed for dislocation segments arriving at the interface to escape [59]. Consequently, in the absence of interfacial dislocations, the Nix-Freund or the Thompson model underestimated the flow stress in polycrystalline films deposited on amorphous layers [60,61] where initiation of plastic deformation is delayed due to the scarcity of dislocation sources as envisioned in the Blanckenhagen model.

Thus, the underlying layer in a metallic film such as Pt plays a major role in determining the inelastic deformation of thin metal films: the source controlled deformation model works well for polycrystalline films in the absence of interfacial dislocation networks, whereas the Nix-Freund model describes well epitaxially grown

single crystal metal films. However, there are hardly any studies on the inelastic deformation of polycrystalline metal films grown epitaxially on polycrystalline layers, which is expected to be significantly different from that of metallic films deposited on amorphous layers. Furthermore, the Nix-Freund or the Thompson model which should be applicable to epitaxially grown metal films also do not model the evolution of flow stress with plastic strain, which remains an open question.

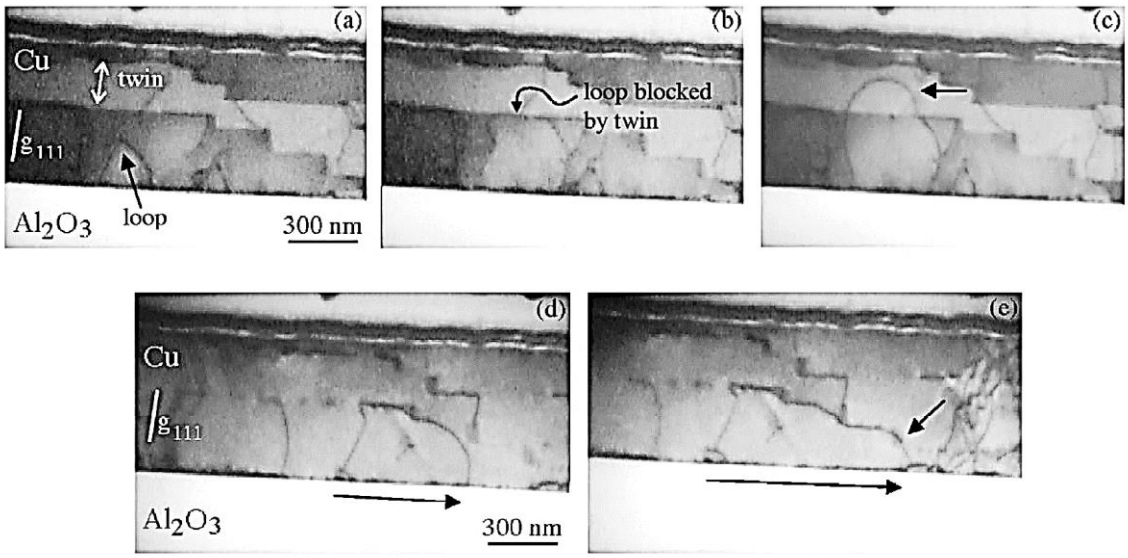

Figure 1.5 Dislocation half-loops in single crystal epitaxial Cu films on Al_2O_3 substrate, originating in the film/substrate interface and expanding during thermal cooling [26]. Reprinted with permission from Elsevier.

1.4 Research Objectives and Approach

The aim of this dissertation research is to investigate the electromechanical response of $Pb(Zr_{0.52}Ti_{0.48})O_3$ thin films, fabricated for low power MEMS devices, as a function of texture ranging from strong (111) texture to strong (001) texture. The composition of PZT 52/48 (52% $PbZrO_3$ and 48% $PbTiO_3$) which is near the MPB has been selected, for which improved properties have been reported in the past [30,62]. In

this work, material microstructure-electromechanical property relationships for PZT film stacks are obtained for different textures and combinations of those. As discussed in Section 1.1, several factors, such as chemical composition, nature and type of interfaces, grain orientation and texture, film thickness, and residual stresses could control the piezoelectric properties of PZT films. However, this study aimed at isolating the effect of film texture on the electromechanical response, and therefore, several of the aforementioned parameters needed to remain constant across different films. Towards this goal, the same MPB composition ratio 52/48, and interfaces (stacking sequence) SiO_2-TiO_2-Pt-PTO-PZT-Pt were utilized. A uniform thickness of ~500 nm for the PTO-PZT layers was targeted during fabrication to eliminate thickness effects. Maintaining uniform grain size was also a goal, but the average measured grain size across different samples was 95 ± 20 nm with the maximum and minimum grain size being 73 ± 4 nm and 125 ± 3 nm, respectively. The important effect of residual stresses on the measured piezoelectric/ferroelectric properties was moderated by etch-releasing and rendering the textured PZT stacks (SiO_2-TiO_2-Pt-PTO-PZT-Pt), initially bonded to thick Si substrates, as freestanding. As a result of the release of the mean and the gradient residual stresses, all test specimen films had an initial curvature. Furthermore, with the release of residual stresses, the effect of the small differences in film thickness would not affect the ferroelectric response, as discussed in Section 1.1.

Thin multilayered freestanding stacks, similar to a d_{31}-mode actuator, with the textured PZT layer deposited via a recently patented microfabrication process [25], were used to characterize and quantify the electromechanical behavior. The stacks were comprised of an elastic SiO_2 layer, an adhesion and seeding layer of {100}-textured rutile (TiO_2) to grow a highly {111}-textured Pt electrode serving as the metallization layer, a seed layer of $PbTiO_3$ with 0-30% excess Pb, the PZT layer with 0-10% excess Pb, a second Pt metallization layer, and, finally, an ALD layer consisting of Al_2O_3 and HfO_2. The excess Pb in the $PbTiO_3$ layer controlled the texture of the PZT film. The film stacks were in the form SiO_2-TiO_2-Pt-PTO-PZT-Pt-ALD, as described in Figure 1.6.

Microscale uniaxial tension experiments were carried out to determine the mechanical properties of the PZT films. Due to the presence of multiple layers,

mechanical characterization of each layer had to be performed to extract both the mechanical and the piezoelectric coefficients for the textured PZT films at hand. The proposed experiments quantified the open circuit mechanical response of textured PZT films and the mechanical behavior of highly (111) textured Pt electrodes in terms of microstructure and size parameters (e.g. grain size, texture, and film thickness).

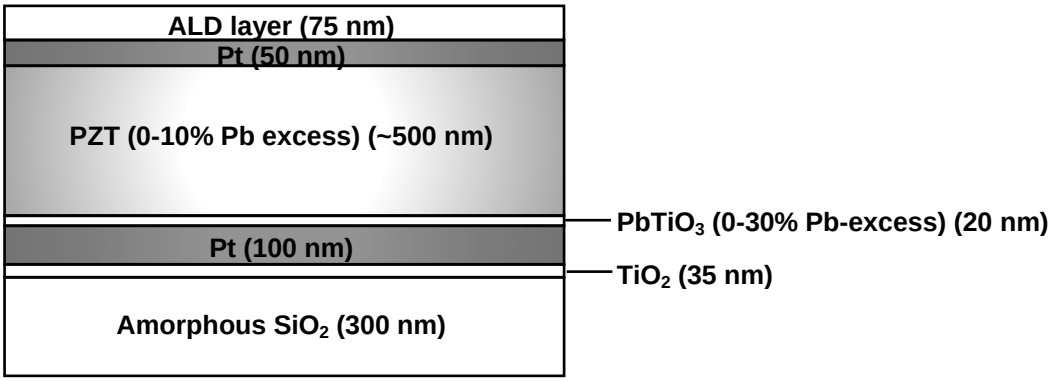

Figure 1.6 Schematic of a PZT stack with layer thicknesses.

Evaluation of the effective piezoelectric coefficients, $d_{31,f}$ and $e_{31,f}$, as a function of electric field for various textures was carried out by obtaining the deflection of cantilevers comprised of PZT stacks, via a laser Doppler vibrometer (LDV). Unlike in bulk PZT ceramics, the rest of the layers in multilayer stacks containing thin PZT films impose constraints on the PZT films thereby reducing the d_{31} coefficient to the "effective piezoelectric strain coefficient" $d_{31,f}$ [63]. Similarly, the measured piezoelectric stress coefficient, e_{31}, which is related to the piezoelectric strain coefficient is termed the "effective stress coefficient" $e_{31,f}$. These effective coefficients are also used to account for other nonlinearities due to the high-field operation of PZT films in MEMS applications [64].

1.4.1 Research Methods and Tasks

The following major tasks were carried out in this research to achieve the aforementioned goals:

1. The mechanical response of {111}-textured Pt thin films with thicknesses ranging between 50-1000 nm on 35-50 nm thick {100}-textured TiO_2 was quantified as a function of film thickness and grain size via microscale uniaxial tension experiments at different strain rates on patterned dog-bone and microscale thin film specimens.
2. The open circuit mechanical response, i.e. the stress-strain response of PZT film stacks was quantified as a function of texture via microscale uniaxial tension experiments on SiO_2, SiO_2-TiO_2-Pt, SiO_2-TiO_2-Pt-PTO-PZT and SiO_2-TiO_2-Pt-PTO-PZT-Pt-ALD stacks.
3. The piezoelectric and ferroelectric response of textured PZT film stacks were evaluated as a function of texture. Experiments were carried out with unimorphs, and the out-of-plane bending response was measured via a laser Doppler vibrometer (LDV).

1.5 Outline of this Dissertation

This thesis consists of six chapters describing the experimental techniques, measurements, data analysis and analytical models developed for the evaluation of the electromechanical and mechanical response of PZT and Pt thin films. The second Chapter describes the experimental techniques that facilitate reliable electromechanical experiments with freestanding thin film materials.

Chapter 3 discusses the elastic/plastic mechanical behavior of freestanding polycrystalline {111}-textured Pt films with thicknesses 50-1000 nm and different combinations of grain size and film thickness, grown epitaxially on a 35-50 nm thick polycrystalline (100)-TiO_2 (rutile) seed layer. Experiments showed that the flow stress increased, while the plastic strain accumulation at failure decreased with decreasing Pt

film thickness. It was revealed that the mismatch strain between the {111}-Pt films and the underlying (100)-TiO_2 seed layer gives rise to an interfacial dislocation network, which, in turn, determined the initiation of plastic deformation in Pt. A modified Thompson model that accounted for the combined effect of film thickness and grain size provided good predictions for the elastic limit of Pt films. A Taylor strain hardening model was superimposed to the modified Thompson model to account for additional hardening as a result of dislocation interactions during plastic deformation, which provided good predictions for the evolution of flow stress with plastic strain.

The fourth Chapter discusses the effect of texture on the mechanical response and linearity in the stress vs. strain behavior of PZT thin films. The open circuit mechanical properties of PZT films with a controlled texture varying from 100% (001) to 100% (111) were quantified for freestanding thin film specimens. The mechanical and ferroelastic properties of 500 nm thick PZT (52/48) films were found to be strongly dependent on grain orientation. A micromechanics model was employed to calculate the strain due to domain switching, which fitted well the non-linearity in the experimental stress-strain curves of (001) and (111) textured PZT films.

The ferroelectric behavior of textured PZT film stacks is presented in the fifth Chapter. The ferroelectric response was derived from deflection measurements of ~500 nm thick PZT unimorphs obtained using an LDV. It was found that the ferroelectric properties were strongly dependent on grain orientation: PZT films with higher %(001) texture content demonstrated more pronounced ferroelectric response than those with high %(111) texture content. Finally, the Conclusions Chapter discusses the results obtained in this dissertation research vis-à-vis the initially stated objectives.

This thesis builds on two journal publications by the author [65,66]. Chapter 3 includes material from Ref. [65] with permission of Elsevier. Chapter 4 includes material from Ref. [66] with permission of AIP Publishing LLC. Some material from both journal publications is incorporated into Chapter 1 and material from Ref. [66] is incorporated into Chapter 2.

CHAPTER 2

EXPERIMENTAL METHODS

In this Chapter, the experimental methods for mechanical testing of thin film specimens and their limitations are presented and discussed, followed by a description of experiments carried out in this dissertation to study the electroactive response of PZT films.

2.1 Experimental Methods for Mechanical Testing of Thin Films

Design and analysis of MEMS devices require extensive mechanical characterization of the constituent materials to ensure failure reliability. The micron or submicron thickness of films deposited for MEMS applications reduces the available options for mechanical testing. Specialized techniques have been developed in the past to measure the mechanical response of thin films and stacks of thin films, such as uniaxial microscale tension [15,67], nanoindentation [8-10,68-72], wafer-deflection [17,73], resonant frequency [7,74,75], surface acoustic wave-based [76], residual stress measurement via X-ray diffraction [77], and surface curvature measurement [78] techniques. An early review can be found at [79].

Instrumented nanoindentation is often the most convenient technique to measure the elastic modulus and hardness of thin films attached to a substrate, requiring no special specimen preparation [80]. However, nanoindentation measurements on thin films can be influenced by substrate effects [81], while in polycrystalline films, the length scales introduced by the grain size and the indentation size can complicate the derivation of equivalent bulk-scale properties. Limiting the indentation depth to less than 10% of the

film thickness has been shown to minimize the effect of the substrate [82], but this rule cannot be practically applied to films with thicknesses of the order of 100 nm because the scatter in the measured modulus is quite large at smaller depths of penetration and applied loads [83]. In such thin films, surface roughness and grain size play a key role in determining the average film properties; for the same indentation depth, it has been shown that standard deviation in the elastic modulus increases with increasing surface roughness [84]. Finally, the nature and magnitude of residual film stresses, film texture, and the presence of thin surface oxide layers, etc. influence the properties measured by nanoindentation.

For freestanding films, the bulge test has been extensively used to obtain the mechanical properties [17,73]. In this type of testing, uniform pressure is applied to one side of a freestanding thin film membrane, formed by back-etching portion of the wafer, resulting in film bulging in a state of plane strain. This technique removes most substrate effects and involves a well-defined stress and strain profile to compute elastic and plastic/failure properties. However, bulge tests require a model and perhaps different types of film geometries to extract the elastic modulus, Poisson's ratio, and residual stress. Also, the accuracy of measured properties through bulge test is reduced when the magnitude of strain due to residual stresses dominates the overall strain. Additionally, stress concentrations at the corners of rectangular or square shaped membranes result in early yielding or failure of brittle films.

Unlike the quasi-static load applied in the film bulge technique, resonance methods have been employed to measure the elastic modulus of thin films, e.g. by monitoring the shift in cantilever resonance frequency [7,74]. The resonance frequency shift, albeit small, could be easily measured from sharp frequency peaks and be used to calculate the thin film modulus. However, most models require precise determination of the geometrical dimensions of the cantilevers and the density of the film and the substrate materials, which may not be easy to measure for micrometer long cantilevers with sub-micrometer thicknesses. Furthermore, this technique is very sensitive to environmental conditions and measurements should be performed inside a vacuum chamber.

Other, less common, techniques have employed surface acoustic waves (SAW), substrate curvature measurements and X-ray diffraction. In the case of SAW, short laser pulses are focused into a line to create wide-band surface acoustic waves on the surface of a thin film which propagate as a pulse along the surface and detected at a different location with a time-resolving detector system. Dispersion causes a change in the pulse shape with distance from the source, which can be harnessed to determine material properties: The frequency dependence is related to the mechanical properties of the film and the substrate and a fit between the experimental data and the theoretical dispersion curves provides the material properties. Other groups have utilized X-ray diffraction [77] to measure the mechanical properties of thin films attached to substrates, and changes in substrate curvature [78] to determine residual thermal stresses.

Of the aforementioned methods, microscale uniaxial tension is the most straightforward method to generate the stress-strain response of a material with the least number of assumptions and measurement uncertainty. Uniaxial tension tests produce macroscopically uniform stress and strain fields that can be directly measured. Several important mechanical properties, such as elastic modulus, fracture stress and strain, yield stress, Poisson's ratio, etc. can be directly extracted unlike other inverse methods where the properties are extracted from the response of a model test structure. A custom-built microscale tension apparatus for freestanding thin films developed by this group in the past [67], was employed for the experiments in this dissertation research as described in detail in the following Sections.

2.2 Microscale Tension Experiments with Thin Films

A custom-built modular apparatus for microscale tension tests with freestanding thin films, described in detail in references [67,85,86] and shown in Figure 2.1, was employed to apply strain rates in the range of 10^{-6} to 10^{1} s^{-1}. Two types of force sensors were employed: a strain gauge load cell for slow rates (10^{-6} to 10^{-3} s^{-1}) and a piezoelectric load cell for higher rates (10^{-3} to 10^{1} s^{-1}). Piezoelectric actuators were used to induce strain to the thin film specimens shown in the figure. The load cell and actuator were

mounted on linear and rotational micro-positioners to control the specimen alignment. The fixed end of the tensile specimen was attached to the load cell using a fixture, while the freestanding end was bonded using UV curable adhesive to the PZT actuator via a glass grip. The apparatus was placed under an optical microscope to record high-resolution images of the specimen surface during loading. The microscope was equipped with two types of digital cameras: a camera with a pixel resolution of 2448×2048 and 15 fps for slow loading rates and a high-speed camera with a pixel resolution of 512×80 and 35,000 fps for higher strain rates. Strains were directly obtained from the specimen gauge section using a fine random speckle pattern deposited on the films by dispersing 1-μm Si particles [67]. The Si particles adhered to the specimen surface due to van der Waals forces and followed the surface points as the film deformed. Application of Digital Image Correlation (DIC) to speckle patterned surfaces provided full-field displacements in the axial and transverse directions.

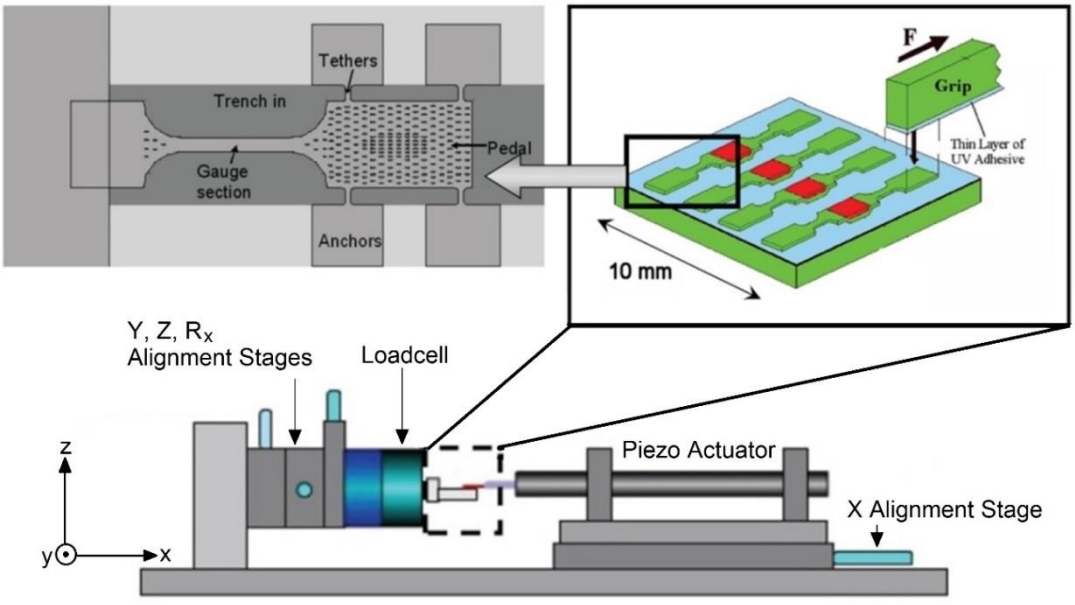

Figure 2.1. Schematic of the apparatus for uniaxial tension experiments with thin film specimens. Figure adapted from Ref. [67,86] with permission from Springer.

The DIC algorithm divides the image into subsets, and point displacements are computed by correlating images taken during deformation with a reference image taken prior to deformation. The reference subset size, chosen to be 15-20 μm as shown in Figure 2.2(a), controls the subset of pixels around the point of interest in the image where displacement is computed. The subset of 15×15 μm^2 contains several grains with average grain size of ~75 nm. At the scale of the DIC subset, the local microstructural features are well averaged out away, as shown in Figure 2.2(b) on the left, the microstructure is not distinguishable at the scale of the subset. As a result, strain heterogeneity at triple junctions and grain boundaries could not be captured by DIC using optical images. Figure 2.2(b) on the right shows a highly magnified area of the PZT top surface where some microstructural features are shown.

To minimize the uncertainty in the displacements calculated using DIC to sub-pixel accuracy, a fine speckle pattern providing smooth grayscale gradients is needed. Si particles resulted in a fine grayscale pattern when imaged by an optical microscope in dark and bright field conditions, e.g. Figure 2.3(a,b). This pattern was highly effective at slow and high imaging rates. It may be noted that the PZT film stacks in Figure 2.3(c) have some curvature unlike the Pt films in Figure 2.3(a,b).

The strain was calculated from the axial displacement field, *u*, via DIC and the procedure outlined in [86]. Figure 2.4(a) shows an optical image of a SiO_2-TiO_2-Pt-PTO-PZT multilayer stack with 2,448 pixels per horizontal line resolution and the superimposed axial displacement contours derived via DIC. The average film strain was computed as the average slope of all axial contour lines in the contour plot in Figure 2.4(a) as described in [86]: Figure 2.4(b) shows the u-displacement as a function of location for 25 horizontal lines of the displacement contours in Figure 2.4(a). The dashed line in Figure 2.4(b) is the average of the best-fit lines to all experimental displacements, and its slope was used as the average strain in the specimen for the particular stress at which Figure 2.4(a) was obtained. The uncertainty in strain calculation is affected by the uncertainty in displacement resolution of DIC. The latter was quantified by rigid body translations of a patterned surface using a PZT actuator with a step size of 12 nm for a total distance of 1,200 nm [67,87]. A comparison with the cumulative rigid body

displacement computed by DIC showed that the uncertainty is of the order of 25 nm (0.15 pixels), and is not cumulative, i.e. remains the same regardless of the total displacement. The experimental surface strains at the top PZT and Pt layers in a PZT stack as computed via DIC were assumed to be the same in every layer in a PZT stack, namely isostrain conditions hold and that the strain is uniform through the thickness of the PZT layer (500 nm). Figure 2.5 shows the stress vs. strain curves of two SiO_2-TiO_2-Pt-PTO-PZT film stacks for two extreme textures with the error bars corresponding to one standard deviation in the strain calculation described in Figure 2.4(b). The uncertainty bars are barely discernible in the plots and therefore omitted when multiple curves are shown in the same chart.

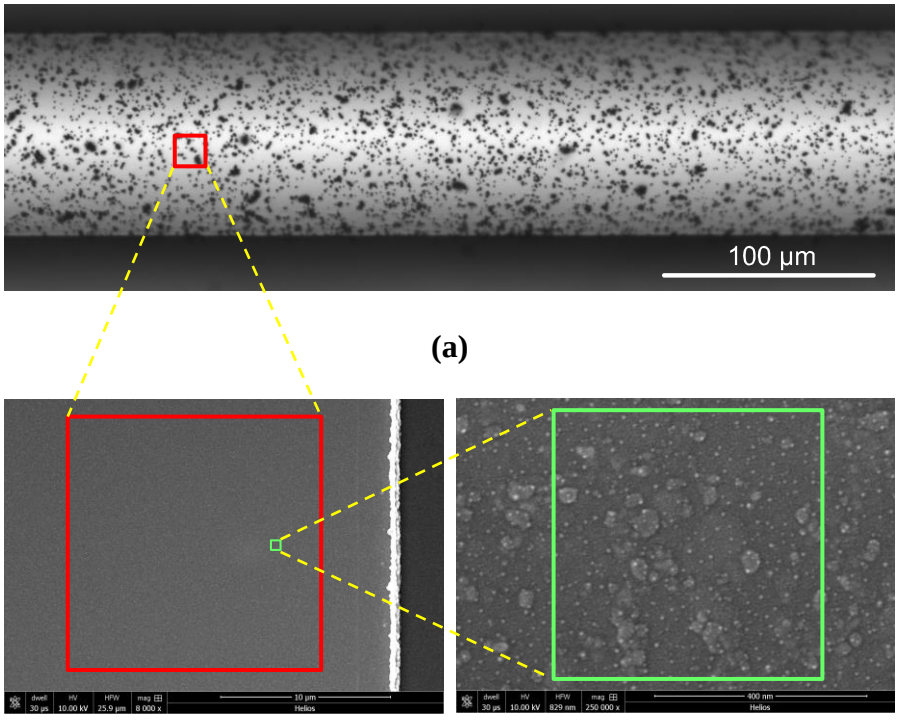

(a)

(b)

Figure 2.2 (a) Top surface of the gauge section of a SiO_2-TiO_2-Pt-PTO-PZT specimen with a speckle pattern. The red box represents the subset chosen to perform DIC. **(b) (Left)** Magnified image of the subset where no microstructural features can be discerned. **(Right)** The grain structure can be distinguished only by high magnification SEM.

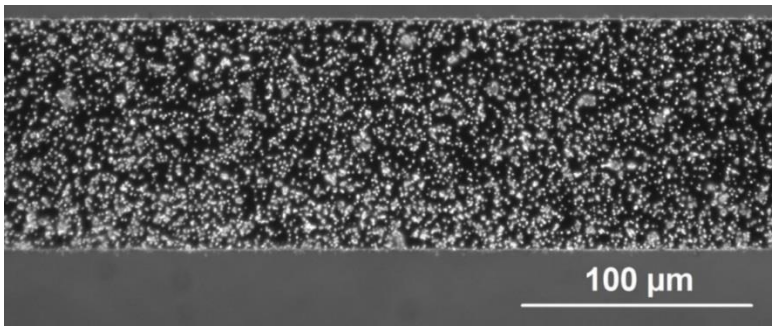

(a)

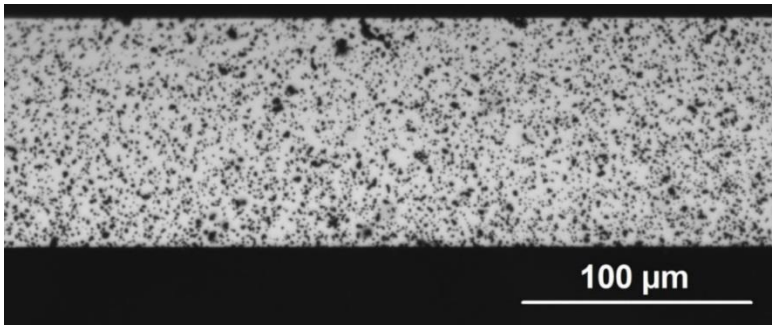

(b)

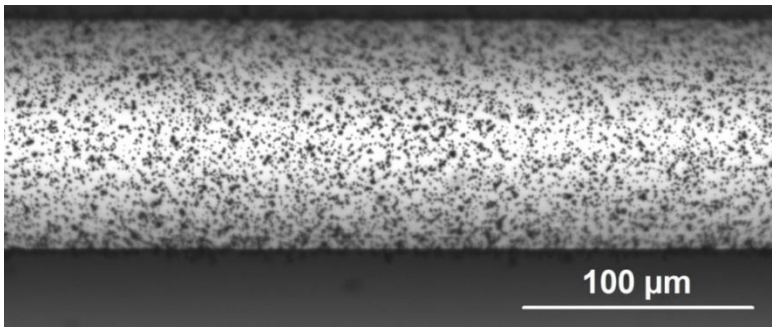

(c)

Figure 2.3. Speckle pattern on the gauge section of 500 nm Pt specimen imaged in **(a)** dark field, **(b)** bright field, **(c)** a multilayer film SiO_2-TiO_2-Pt-PTO-PZT imaged in bright field conditions.

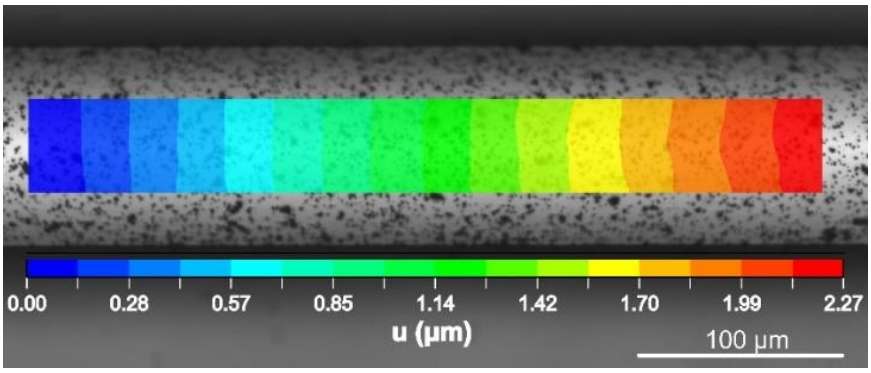

(a)

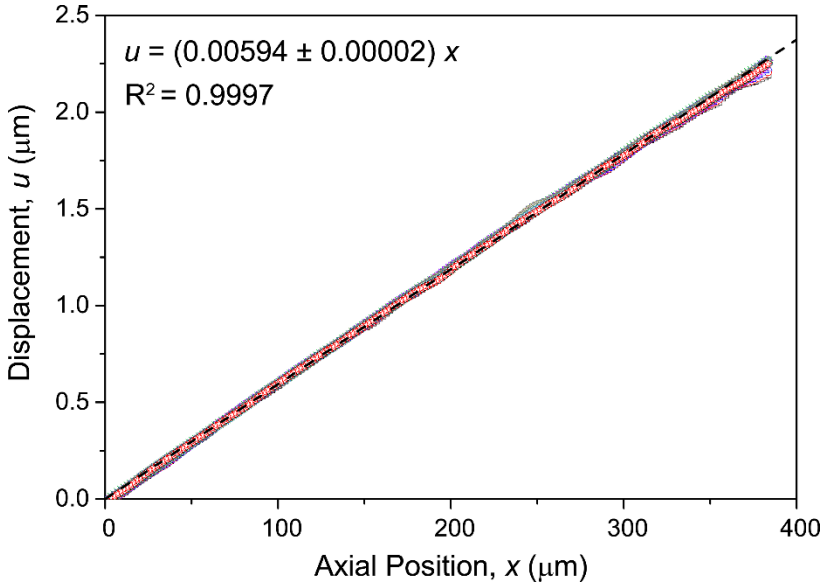

(b)

Figure 2.4. **(a)** SiO_2-TiO_2-Pt-PTO-PZT film stack with speckle pattern on the gauge section. The superposed axial displacement field computed by DIC shows excellent specimen alignment. **(b)** Axial displacement as a function of position for 25 lines of the displacement contours. The slope of the line profiles is the strain in the axial direction, and the average value is given by the dashed line.

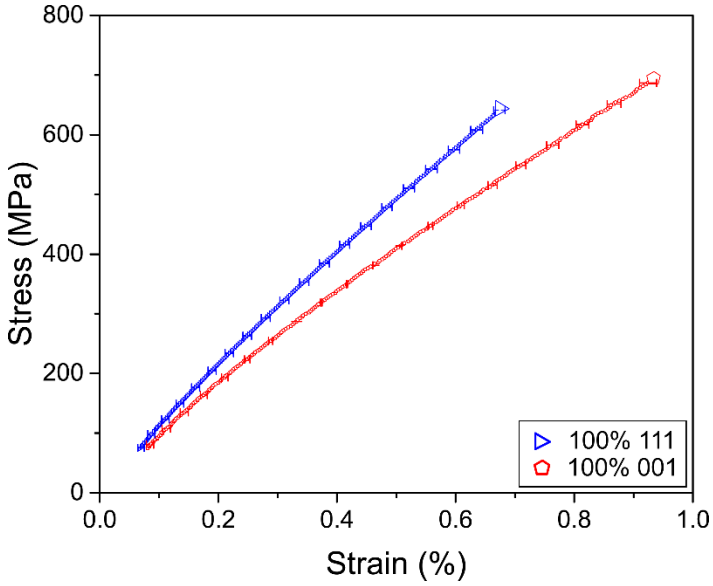

Figure 2.5. Stress vs. strain response of a SiO_2-TiO_2-Pt-PTO-PZT film stack for two extreme textures of PZT with the error bars in strain, computed using the approach shown in Figure 2.4, corresponding to one standard deviation. The uncertainty bars are barely discernible in the plots and, therefore, are omitted when multiple curves are shown in the same chart.

2.3 Ferroelectric Characterization of Thin Film PZT Stacks

Design and analysis of PZT-based MEMS devices require extensive knowledge of electromechanical parameters. Several piezoelectric coefficients are in use in PZT MEMS devices which can be designed either in d_{33} or d_{31} mode depending on whether the longitudinal or the transverse piezoelectric response, respectively, is harnessed as explained in Figure 2.6. For thin film PZT, modest but potentially useful [88] surface displacements are generated in d_{33} mode, Figure 2.6(a). The d_{33} mode could also be utilized in a flexural structure with interdigitated electrodes patterned on the PZT film, Figure 2.6(b). Applying an electric field between the electrodes, a modest in-plane strain can be induced in the plane of the film which leads to large out-of-plane displacements. Figure 2.6(c) shows the most commonly used d_{31} or e_{31} modes [2,6] to achieve large deflections of thin films.

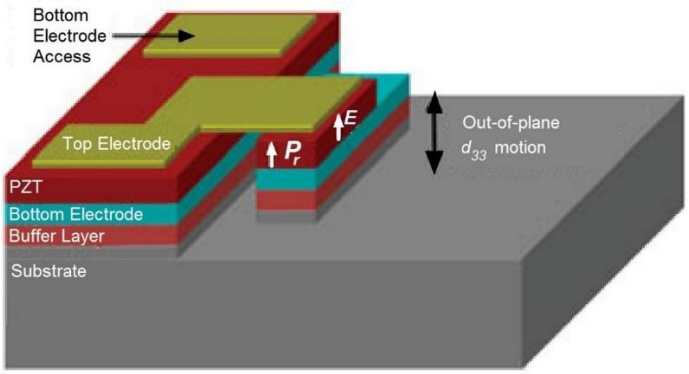

(a)

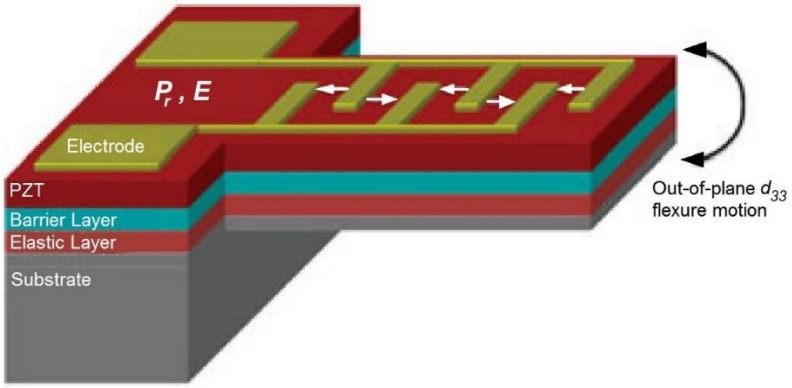

(b)

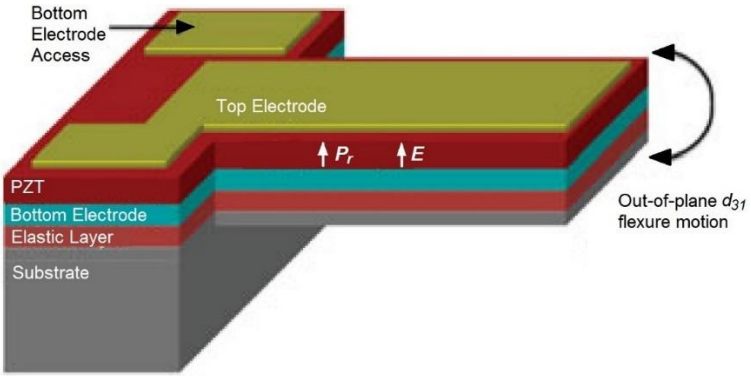

(c)

Figure 2.6. Schematic of common sensing and actuation modes in piezoelectric MEMS. **(a)** Out-of-plane piston mode, **(b)** bending d_{33} mode, and **(c)** bending d_{31} or e_{31} mode. Figures adapted from [89].

In Figure 2.6(c), an electric field applied in the PZT thickness direction between the top and bottom electrodes induces strain in the thickness direction which, in turn, gives rise to in-plane strain. The unimorph structure then bends due to the mechanical asymmetry of the structure about the piezoelectric layer. Since the thickness of the PZT films used in this study was only 500 nm, the d_{31} mode was utilized.

In this dissertation research, cantilevers with d_{31} configuration were fabricated. As described in Chapter 1, the piezoelectric coefficient $d_{31,f}$ depends on several factors, such as chemical composition, nature and type of interfaces, grain orientation and texture, film thickness, and residual stresses. Although several attempts were made in the past to measure d_{31} of PZT thin films, by measuring the charge generated by a laterally deformed PZT film on a Si wafer [29,90] or from the out-of-plane deflection of PZT cantilevers, universally accepted standard methods for the evaluation of the piezoelectric coefficient, d_{31} have not been established yet. The following Section describes the experimental methods used in this study to determine the ferroelectric and dielectric parameters of the PZT films at hand. Details about the fabrication of the PZT stacks and Pt films are provided in the respective Chapters in this dissertation.

2.3.1 Measurement of Ferroelectric and Dielectric Properties

Periodic oscillation of cantilever arrays fabricated from PZT stacks was induced by applying triangular wave voltage signals between the upper and bottom Pt electrodes in PZT stacks. Then, non-contact displacement measurements along the length of each cantilever were measured using a Polytec MSV-400 microscope scanning laser Doppler vibrometer (LDV) described in the schematic in Figure 2.7. The LDV was made available for this research by the US Army Research Laboratory (ARL) in Adelphi, MD. The out-of-plane displacement resolution of the LDV system was ~10 nm with a lateral resolution of ~2 μm using a 20× objective lens. An internal function generator created the triangular wave signals at 2 Hz, which is much lower than the mechanical resonant frequencies of the cantilevers, which are of the order of 100s of kHz. Voltage was applied to the top electrode while the bottom electrode was grounded. The out-of-plane

displacement and velocity were obtained using an interferometer that utilized a helium neon laser, which compared the reflected laser beam to a reference beam. The frequency and phase difference provided the instantaneous velocity and displacement, respectively. The displacement values along the length of the cantilevers were used to calculate the transverse piezoelectric properties of the textured freestanding PZT films. Additionally, polarization vs. electric field (*P*-*E*) hysteresis loops were measured at 100 Hz using a Radiant Technologies RT-66A measurement unit, and capacitance versus voltage (C-V) sweeps were performed using the Agilent Technologies B1500A device analyzer.

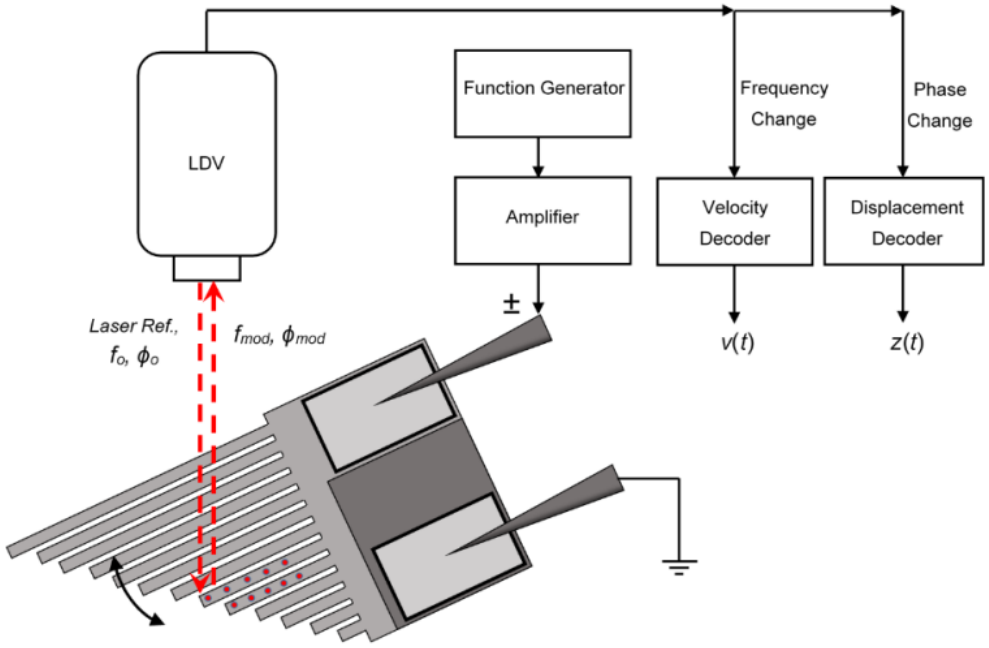

Figure 2.7. Displacement and velocity measurement principles using an LDV. Figure adapted from [91].

2.4 Summary

The experimental methods employed to achieve the objectives of this dissertation research, outlined in Chapter 1 were presented and discussed. A custom built modular tensile testing apparatus was employed to study the mechanical response of Pt films and PZT film stacks in the wide range of strain rates 10^{-6} – 10^{1} s^{-1}. Uniaxial tension experiments were performed under an optical microscope, and DIC was employed to compute local displacements with a resolution of ~25 nm. An LDV setup was used to measure out-of-plane deflections of microfabricated cantilevers which were then used to compute ferroelectric and linear piezoelectric coefficients of textured PZT.

CHAPTER 3

Mechanical Behavior of Epitaxially Grown {111} Textured Pt Films

Pt thin films with thicknesses ranging between 50 nm and 8 μm [92] are frequently used as contact electrodes in piezoelectrically actuated MEMS. Most high conductivity metals, such as Al or Au, have a low melting point and hence low thermal stability and show creep deformation even at room temperatures [93,94]. High melting point materials, such as Ti and Ta, suffer from decreased chemical inertness and higher electrical resistivity. On the other hand, Pt is a relatively hard material with high melting point (T_m~1768°C), good conductivity and excellent chemical resistance. It is, therefore, utilized either as structural or contact material in MEMS devices with high resistance to plastic deformation at elevated temperatures while providing good electrical conductivity [95]. In connection with PZT materials, Pt films provide a sharp interface that suppresses diffusion of Pb and prevents the formation of lead silicate phases which would otherwise leach Pb from the ferroelectric and severely degrade its electrical properties [96]. It was recently shown that {001}-textured PZT with high transverse piezoelectric coefficient could be grown on a {111}-textured Pt layer [97]. Thus, piezoelectric properties which are strongly crystal structure dependent [30] may be tuned with appropriate choice of Pt film texture leading to an enhancement of PZT-based MEMS performance.

Previous studies on the mechanical behavior of Pt thin films utilized various techniques including resonance [75], nanoindentation [68-72] and uniaxial tension [67,98]. Salvadori *et al*. [75] measured the resonance frequencies of atomic force microscope (AFM) cantilevers before and after coating them with Pt films with thicknesses between 18 and 73 nm; the authors used beam theory to determine the elastic

moduli of Pt as 139.7 ± 2.7 GPa. Mencik and Swain [68, 69], Lee *et al*. [70], Hyun *et al*. [71], and Romasco *et al*. [72] applied instrumented nanoindentation to quantify mechanical properties of Pt thin films with thicknesses in the range of 200 - 1500 nm and reported elastic moduli in the range 154 - 190 GPa. Jonnalagadda *et al*. [67] performed uniaxial tension tests at strain rates between 10^{-6} - 10^{1} s^{-1} on 400 nm thick freestanding Pt films and reported an elastic modulus of 182 ± 8 GPa. They also showed that inelastic properties of nanocrystalline Pt films were rate-sensitive with tensile strength reaching almost 2 GPa at the fastest strain rate of 10 s^{-1} which is several times that of bulk, large grain Pt. Meirom *et al*. [98] also performed uniaxial tension tests on 460 nm thick freestanding Pt films and reported an elastic modulus of 158 ± 5 GPa with a yield strength of 1.5 ± 0.1 GPa and ultimate strength of 1.75 ± 0.05 GPa.

Most previous studies on Pt thin films were concentrated on a single film thickness or treated different thicknesses individually providing no correlation between film thickness, grain size, and mechanical response. Furthermore, the available literature on Pt thin films [68-70] has not always documented the details about film structure, i.e. film texture and grain size, which makes it difficult to establish the interplay between microstructural parameters in the mechanical response of Pt thin films.

Experiments with other face-centered cubic (FCC) Ag, Al, Au, Cu, Ni, Pb films with thicknesses of 50-2,000 μm have shown that the flow stress increases with decreasing film thickness [26-28,60,61,99-102]. In the case of metal films deposited on substrates, mechanistic models have been developed to explain this inverse film thickness dependence of flow stress. Based on the threading dislocation concept by Freund for a film bonded to a substrate with some mismatch strain [54], Nix [55] developed a quantitative model considering the film/oxide and film/substrate interfaces acting as impenetrable obstacles to dislocation motion, thus necessitating the deposition of misfit dislocations at interfaces. Later, Thompson [56] extended the Nix-Freund model to polycrystalline films with grain diameters that are at least twice as large as the film thickness by including grain boundaries (GBs) as additional obstacles to dislocation motion. The two models combined could qualitatively explain the inverse film thickness and grain size dependence of flow stress that was reported for Al films deposited on Si

substrates with an anodic oxide layer at the top surface [27]. Both the Nix-Freund and the Thompson models showed that the film texture influenced the yield stress.

The Nix-Freund model could quantitatively capture the flow stress of epitaxial metal films. Furthermore, epitaxial film-substrate interfaces acted as dislocation sources, and dislocation half-loops were emitted from the interfacial dislocation network. In contrast, no such phenomena were observed in polycrystalline films deposited on amorphous oxide or nitride layers on Si substrates. The amorphous underlayers did not promote the formation of stable interfacial dislocation networks because they permitted atomic rearrangements at the interface, thus allowing for dislocation segments arriving at the interface to escape [59]. Consequently, in the absence of interfacial dislocations, the Nix-Freund or the Thompson model underestimated the flow stress in polycrystalline films deposited on amorphous layers [60,61] where initiation of plastic deformation is delayed due to the scarcity of dislocation sources.

Von Blanckenhagen *et al*. [57] used the aforementioned idea to model the deformation response of polycrystalline metal films. They considered dislocation sources in polycrystalline metal films to be rare and, therefore, each Frank-Read source inside a grain had to operate several times to generate more dislocations and achieve the resulting plastic deformation. Their approach using discrete dislocation dynamics reproduced the experimentally measured flow stresses in polycrystalline Cu films deposited on amorphous and deformable polyimide layers. Thus, the underlying layer plays a major role in determining the plastic deformation of metal films: source controlled deformation models work well for polycrystalline films in the absence of interfacial dislocation networks, whereas epitaxially grown single crystal metal films are well described by the Nix-Freund model. However, there are hardly any studies on the deformation behavior of polycrystalline metal films grown epitaxially on polycrystalline layers. Although many metal films are deposited on amorphous diffusion barrier layers that are on top of single crystal silicon to prevent the formation of metal silicides [103,104], there are cases when polycrystalline metal films were grown epitaxially on polycrystalline layers in order to achieve specific textures [105]. The deformation behavior of such films is expected to be significantly different than of those films deposited on amorphous layers. Furthermore,

the Nix-Freund or the Thompson models which should be applicable to epitaxially grown metal films do not model the evolution of flow stress with plastic strain.

This dissertation investigated the inelastic response of highly {111}-textured epitaxial polycrystalline Pt films grown on 35-50 nm thick (100)-textured polycrystalline rutile TiO_2 underlayers. Specifically, this research focused on relationships between the film thickness, grain size, strain rate and the plastic mechanical response of textured Pt films in the form of bilayers with an underlying TiO_2 seeding layer and total thicknesses ranging between 50 nm and 1000 nm. The role of high aspect ratio columnar grain structure, which is not captured by previous models, was also addressed. To this goal, existing dislocation-based mechanistic models, modified to account for strain hardening, were applied to predict the evolution of flow stress with plastic strain and were compared with the experimental measurements obtained in this research.

3.1 Experimental Methods

3.1.1 Specimen Preparation and Materials Characterization

Micro and nanometer thick freestanding Pt film specimens were fabricated at the US Army Research Laboratory (ARL) in Adelphi, MD using a combination of DC magnetron sputtering and etching on Si (100) substrate. The fabrication process, described in detail in [106], began with the deposition of a base layer of Ti on a 500 ± 25 nm thermally grown SiO_2 layer on a silicon wafer to serve as an adhesion layer using DC magnetron sputtering with a 99.99% pure Ti target at 40˚C. The Ti films had a strong {0001} texture with the basal plane of hexagonal close-packed (HCP) structure lying in the plane of the substrate. The Ti films were then converted to rutile through oxygen annealing for 30 minutes inside a tube furnace at 750˚C. The TiO_2 films had measured thicknesses of 35 nm and 50 nm, and X-Ray diffraction studies showed (100) texture for TiO_2. Next, sputter deposition of Pt was carried out for thicknesses of 1000, 500, 200, 100 and 50 nm onto the TiO_2 with a 99.99% pure Pt target at a substrate temperature of 500°C as shown in step (A) in Figure 3.1(a). The resulting {111}Pt||(100)TiO_2 grain-to-grain heteroepitaxy has been established before for 100 nm thick Pt films [105,106] with

the underlying (100)-textured TiO_2 acting as the seed layer for the growth of {111}-textured Pt. Patterning of the Pt films to specimen geometries and dimensions was done using Ar ion milling, as shown in Figure 3.1 steps (B) and (C). Prior to isotropic etching of the Si substrate to release the test structures, the wafer was exposed to a 20-second reactive ion etching with CHF_3 and O_2 to remove the surface oxide developed on the exposed silicon surfaces. Next, the film was subjected to xenon difluoride (XeF_2) isotropic etching to remove the Si underneath as shown in step (D). Finally, freestanding Pt/TiO_2 bilayers were prepared by treatment with a solution of buffered hydrofluoric acid (HF) which removed the SiO_2 layer, step (E). After release, the wafer was diced using Mahoh dicing from Accretech America to prepare individual dies containing dog-bone specimens with 1035 nm and 535 nm thicknesses, Figure 3.1 (b), and micro-tensile specimens of 250 nm, 150 nm and 100 nm thickness, Figure 3.1 (c). The dog-bone specimens had gauge width and length of 100 and 1000 μm, respectively, whereas the chosen micro-tensile specimens had three gauge widths of 13, 19 and 30 μm, and lengths varied in the range of 150 - 350 μm.

Focused ion beam (FIB), scanning electron microscopy (SEM), atomic force microscopy (AFM) and X-ray diffraction (XRD) studies were conducted to determine the thickness, average grain size, surface morphology and texture of the Pt films, respectively. The mean grain size and standard deviation were measured from SEM micrographs, such as those shown in Figure 3.2(a-e), by using the intercept method and taking into account ~2,000 columnar grains in each film. The unimodal curves in Figure 3.2(f) fit log-normal distribution functions well and broaden with increasing film thickness. As shown in Table 3.1, the average planar grain size scaled with Pt film thickness, which may be due to a specimen thickness effect [107] occurring as a result of pinning of GBs by surface grooves when the mean size of columnar grains approaches the film thickness [108]. Studies have also revealed that GB grooving affects the grain size distribution of stagnant grain structures in thin films, as in the case of pinned GBs, and these distributions are well described by log-normal probability distributions [109,110].

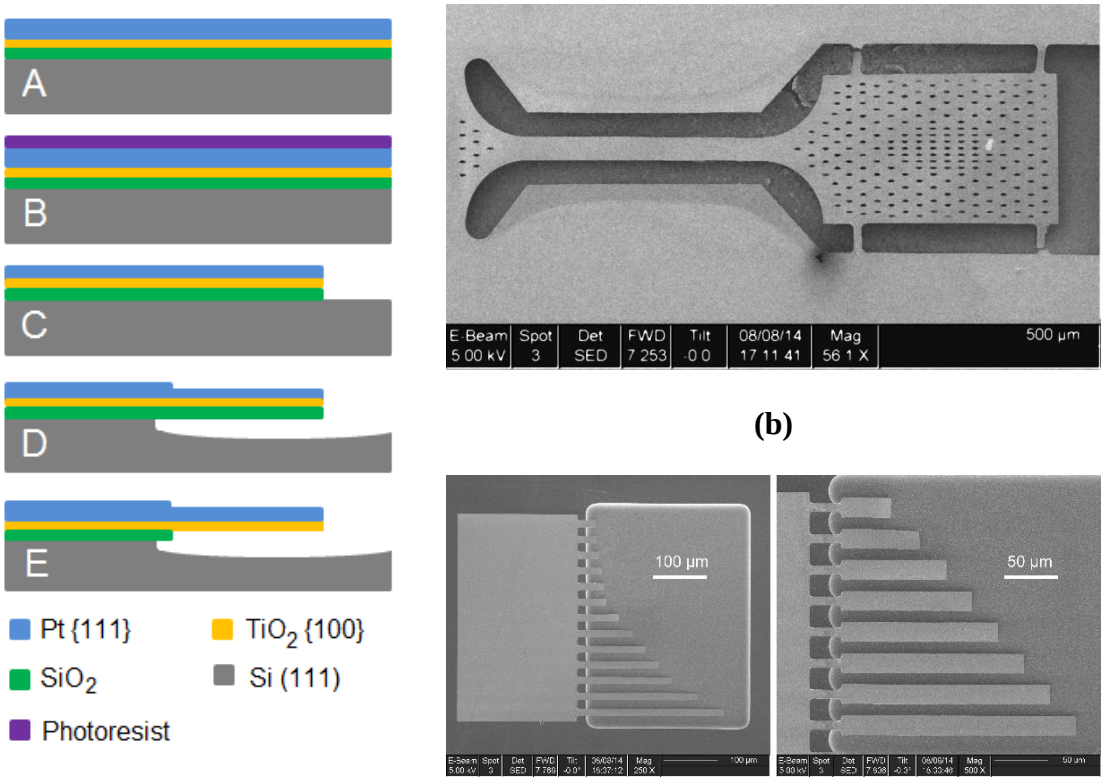

(a) **(b)** **(c)**

Figure 3.1 (a) Fabrication steps of freestanding Pt/TiO_2 specimens for mechanical experiments: (A) deposition of Pt by DC magnetron sputtering on TiO_2, (B) and (C) patterning via Ar ion milling, (D) etching of the underlying Si layer with XeF_2, and (E) removal of the SiO_2 layer via HF. **(b)** SEM micrograph of a dog-bone specimen for microscale tensile testing of 500-1000 nm thick Pt films. **(c)** SEM micrographs of micro-tensile specimens for mechanical testing of 50 – 200 nm thick Pt films. Note that the same specimen geometry as in (b) was used in microscale experiments with SiO_2, TiO_2-Pt, SiO_2-TiO_2-Pt, SiO_2-TiO_2-Pt-PTO-PZT and SiO_2-TiO_2-Pt-PTO-PZT-Pt-ALD stacks.

It may be noted that previous studies on Pt films reported in-plane grain sizes of 20-50 nm [72], 25±3 nm [67], and 25±10 nm [98] for 450 nm, 400 nm and 450 nm thick films, respectively. The small grain sizes reported previously were due to film deposition at substrate temperature of 50°C (~0.15 $T_{m,Pt}$); it has been suggested that at these low

homologous temperatures, continued “renucleation” of grains occurs athermally during deposition and the resulting grain size (5-20 nm) is governed by the density of crystalline nuclei [111]. In this study, Pt deposition was carried out at a substrate temperature of 500°C (~0.37 $T_{m,Pt}$) when GBs are relatively mobile and thin columnar structures (d/h < 1) with uniform grain diameter are produced [111]. Low current milling and cross-sectional imaging using a FIB revealed such columnar grains: Figures 3.3(a,b) show FIB-milled cross-sections of 1000 and 200 nm thick Pt films revealing a columnar grain structure approaching near-equiaxed shape.

Figure 3.4(a) provides the X-ray diffractograms for Pt films of various thicknesses. The XRD spectrum showed highly {111}-textured Pt films with only {111} and {222} peaks for Pt. In addition to omega-2theta scans, rocking curve measurements on {111} and {222} Pt peaks revealed {111}-texture. Table 3.1 reports the full width at half maximum (FWHM) values obtained from the rocking curves. The {222}-FWHM values between 1.5° and 2.3° indicate excellent alignment of {111} planes parallel to the film surface.

Finally, pole figure analysis revealed {111} fiber texture for all Pt films. Figure 3.4(b,c) show pole figure plots for {111} and {200} planes in a 500 nm thick Pt film. The {111} plot shows concentrated intensity distribution at the center and an encircled ring at an angle of 70.5° from the center. Thus, {111} planes are mostly aligned parallel to the film surface, with the angles between {111} planes being either 0° or 70° 32´. {200} planes make an angle of 54° 74´ with {111} planes and hence the {200} pole figure shows concentrated intensity distribution in a ring at an angle 54.7° from the center. Also, since the {111} and {200} pole density distributions are uniform in the form of radially symmetrical rings at 70.5° and 54.7° respectively, the film has in-plane isotropy.

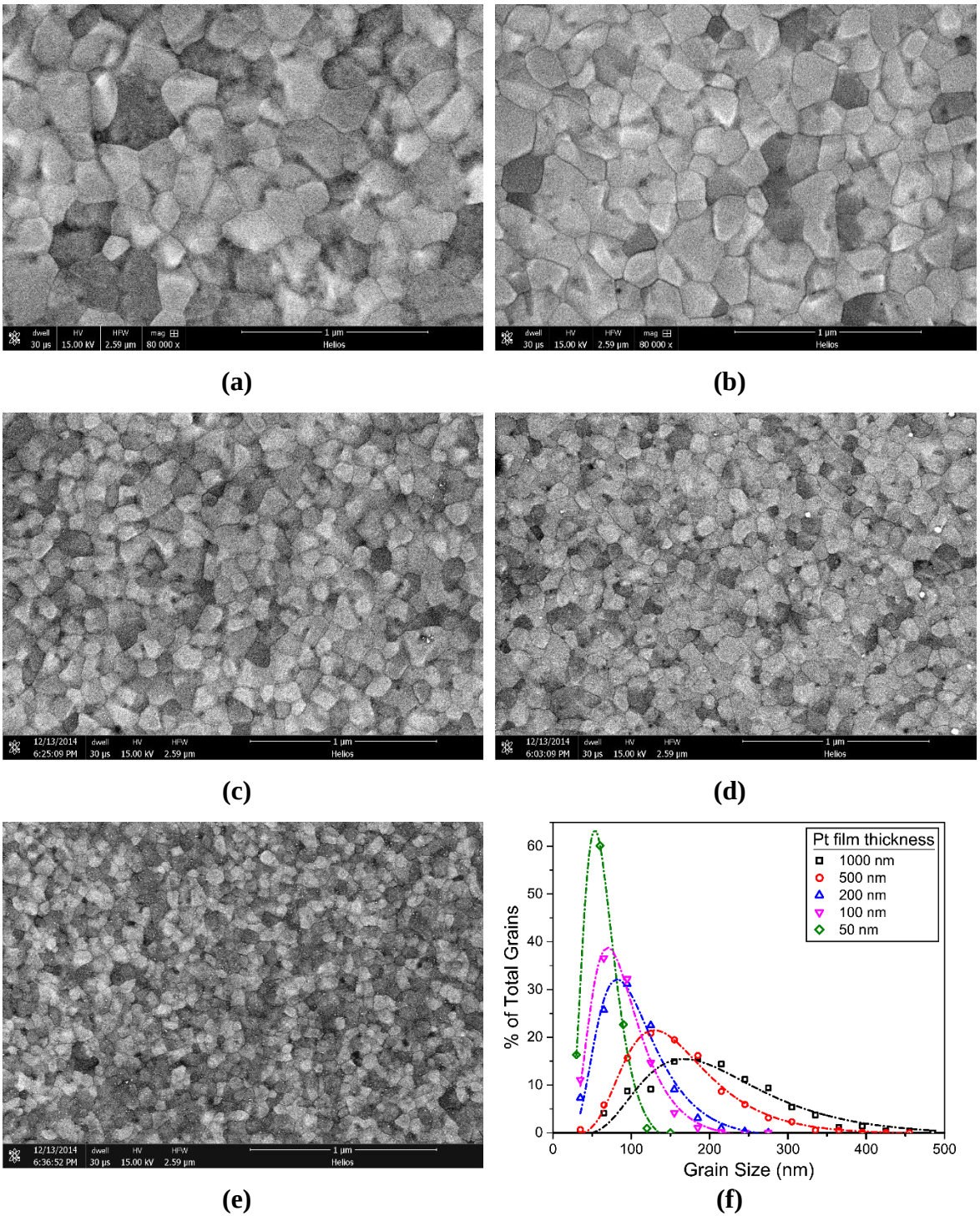

Figure 3.2 In-plane SEM micrographs for Pt films with thickness **(a)** 1000 nm, **(b)** 500 nm, **(c)** 200 nm, **(d)** 100 nm, and **(e)** 50 nm. **(f)** Grain size distributions obtained by the intercept method.

Table 3.1. In-plane grain size and {222}-FWHM of Pt films with various thicknesses.

Pt Thickness (nm)	TiO_2 Thickness (nm)	Mean Grain Size (nm)	Standard Deviation (nm)	{222}-Pt FWHM from Rocking Curves (degrees)
1000	35	200	75	1.518
500	35	160	60	1.662
200	50	100	35	1.933
100	50	85	30	2.011
50	50	50	20	2.335

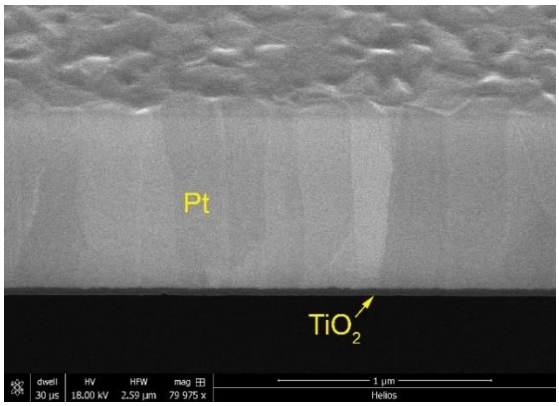

(a)

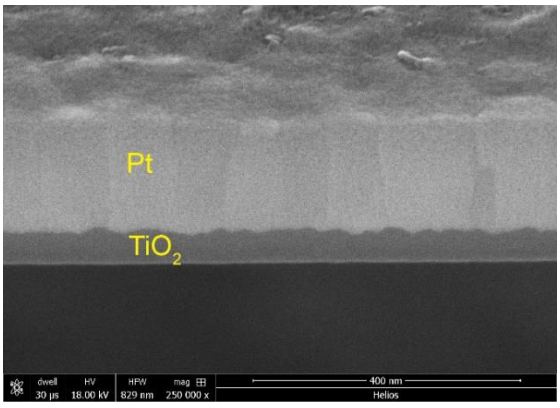

(b)

Figure 3.3 Columnar grains in **(a)** 1000 nm, and **(b)** 200 nm thick Pt films.

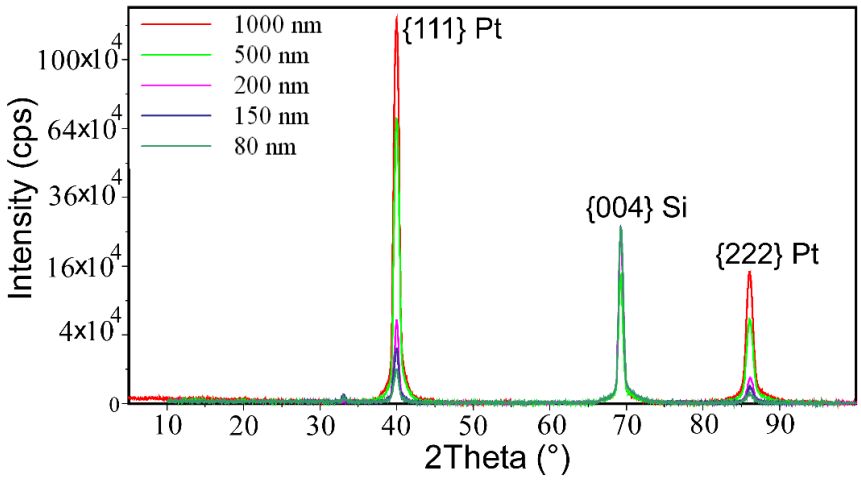

(a)

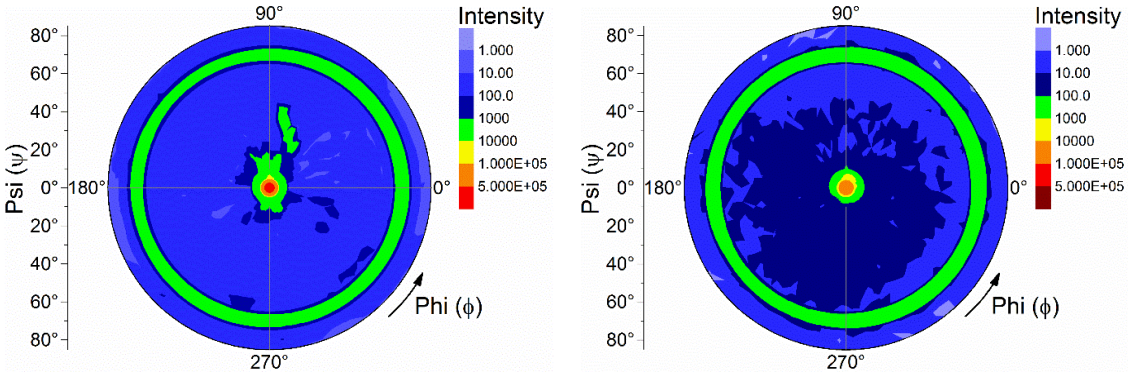

(b) **(c)**

Figure 3.4 (a) XRD (ω-2θ) scans of Pt films showing only {111} and {222} Pt peaks. **(b,c)** 2D surface plots of pole figures of {111} planes for a (b) 1000 nm and (c) 200 nm thick Pt film.

The surface morphology of the Pt film surfaces was investigated with AFM, and average values for the major surface roughness parameters were obtained in three different areas, each with dimensions 5×5 μm^2, 4×4 μm^2, 3×3 μm^2, 2.5×2.5 μm^2 and 2.5×2.5 μm^2 for 1000 nm, 500 nm, 200 nm, 100 nm and 50 nm films thick, respectively. Figure 3.5(a) shows the surface topography of a 5×5 μm^2 area in a 1000 nm thick film. Figure 3.5(b) shows the linear increase of the mean (Sa) and the root mean square (Sq) roughness of different film surfaces as a function of film thickness.

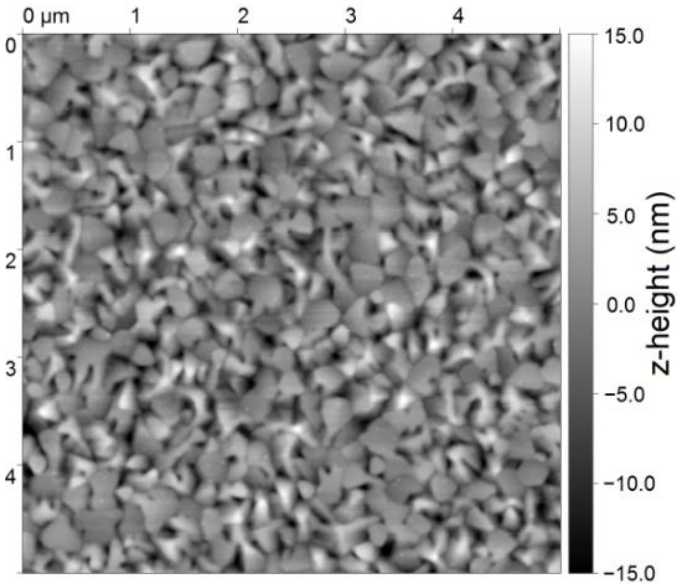

(a)

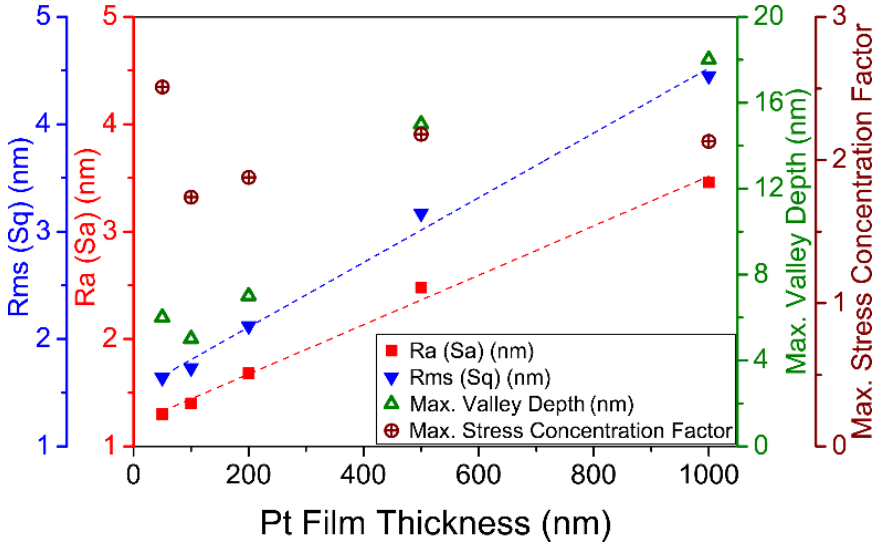

(b)

Figure 3.5 (a) Surface topography of a 1000-nm thick Pt film, and **(b)** surface roughness parameters Sa, Sq, maximum valley depth and computed maximum stress concentration factors (see later Section 3.3.1) at the surface vs. Pt film thickness. The dashed line fits show a linearly increasing roughness with film thickness.

3.2 Elastic Properties of Pt and TiO_2 Films

A custom-built microscale tension apparatus for freestanding thin films, described in detail in Section 2.2, was employed to apply strain rates in the range of 10^{-6} to 10^{1} s^{-1}. Figure 3.6 shows the engineering stress vs. strain curves for Pt/TiO_2 bilayers tested at 10^{-3} s^{-1}. The elastic moduli computed from the initial slopes of all stress vs. strain curves are reported in Table 3.2. The initial unloading moduli of Pt/TiO_2 bilayers were the same as the initial loading moduli. The Pt/TiO_2 bilayer modulus increased slightly with decreasing film thickness due to the contribution of the relatively higher modulus of TiO_2. The elastic moduli of the Pt and TiO_2 layers were extracted from the Pt/TiO_2 bilayer moduli by assuming isostrain deformation:

$$E_{Pt} = \frac{Et{t_2}' - E't't_2}{(t_1{t_2}' - {t_1}'t_2)} \tag{3.1a}$$

$$E_{TiO_2} = \frac{Et{t_1}' - E't't_1}{({t_1}'t_2 - t_1{t_2}')} \tag{3.1b}$$

where E and E' are the elastic moduli of two Pt/TiO_2 bilayers with thicknesses t and t' respectively, t_1 and t_2 are the thicknesses of the Pt and TiO_2 layers, respectively, in the film with total thickness t, and ${t_1}'$ and ${t_2}'$ are the thicknesses of the Pt and TiO_2 layers, respectively, in the film with total thickness t'. Using Equations (3.1a) and (3.1b) and taking the average value of the elastic modulus for each Pt/TiO_2 thickness combination, the elastic moduli of Pt and TiO_2 films were computed as 167 ± 2 GPa and 195 ± 5 GPa, respectively.

Pt has FCC crystal structure, and the Pt films at hand had columnar grains with {111}-fiber texture. The TiO_2 films had (100) or (010) texture and body-centered tetragonal rutile crystal structure. The elastic moduli of single crystal cubic and tetragonal systems along a crystallographic $\langle hkl \rangle$ direction [112] are given by:

$$E_{\langle hkl \rangle\ cubic} = \frac{1}{s_{11} - 2\left(s_{11} - s_{12} - \frac{s_{44}}{2}\right)(\alpha^2\beta^2 + \beta^2\gamma^2 + \gamma^2\alpha^2)} \tag{3.2a}$$

$$E_{\langle hkl\rangle\ tetragonal} = \frac{1}{(\alpha^4+\beta^4)s_{11}+\gamma^4 s_{33}+\alpha^2\beta^2(2s_{12}+s_{66})+\gamma^2(1-\gamma^2)(2s_{13}+s_{44})} \quad (3.2b)$$

where α, β and γ are the direction cosines and s_{ij} are the compliance coefficients. The compliance coefficients, s_{ij} for single crystal Pt at 300 K and for single crystal rutile TiO_2 were obtained from [113] and [114], respectively, and are given in Table 3.3. By invoking transverse isotropy, Equation (3.2) is averaged for an aggregate of columnar grains to obtain an estimate for the effective in-plane modulus of {111}-textured Pt and (100)-textured TiO_2:

$$\overline{E}_{Pt} = \frac{1}{2\pi}\int_{-\pi}^{\pi} \frac{d\theta}{\left(s_{11}-2\left(s_{11}-s_{12}-0.5s_{44}\right)\left(0.25\right)\right)} = 166 \text{ GPa} \quad (3.3a)$$

$$\overline{E}_{TiO_2} = \frac{1}{2\pi}\int_{-\pi}^{\pi} \frac{d\theta}{\left(\cos^4\left(\theta\right)s_{11}+\sin^4\left(\theta\right)s_{33}+\sin^2\left(\theta\right)\cos^2\left(\theta\right)\left(2s_{13}+s_{44}\right)\right)} = 224 \text{ GPa} \quad (3.3b)$$

For {111} Pt, the term $(\alpha^2\beta^2+\beta^2\gamma^2+\gamma^2\alpha^2)$ reduces to 0.25 without any angular dependence, and as a result, the Pt films exhibit in-plane isotropy even at the level of individual columnar grains. Substituting s_{ij} to Equations (3.3a) and (3.3b) yields the in-plane elastic modulus $\overline{E}_{Pt}$=166 GPa for {111}-texture and $\overline{E}_{TiO_2}$= 224 GPa for (100)-texture. The theoretical value of $\overline{E}_{Pt}$ compares well with the experimental result of 167 ± 2 GPa, whereas there is a 15% difference between the theoretical modulus, $\overline{E}_{TiO_2}$, and the experimental result of 195 ± 5 GPa. The calculated elastic moduli values of the thin TiO_2 films are very sensitive to film thickness measurements. As inferred from the cross-sectional SEM micrograph in Figure 3.3(b), the interface between Pt and TiO_2 is rough, with the amplitude roughness accounting for a significant fraction of the thickness of the TiO_2 layer. For example, an overestimate of the thickness of the TiO_2 layer by 5 nm would result in 10% underestimate in the computed modulus of TiO_2.

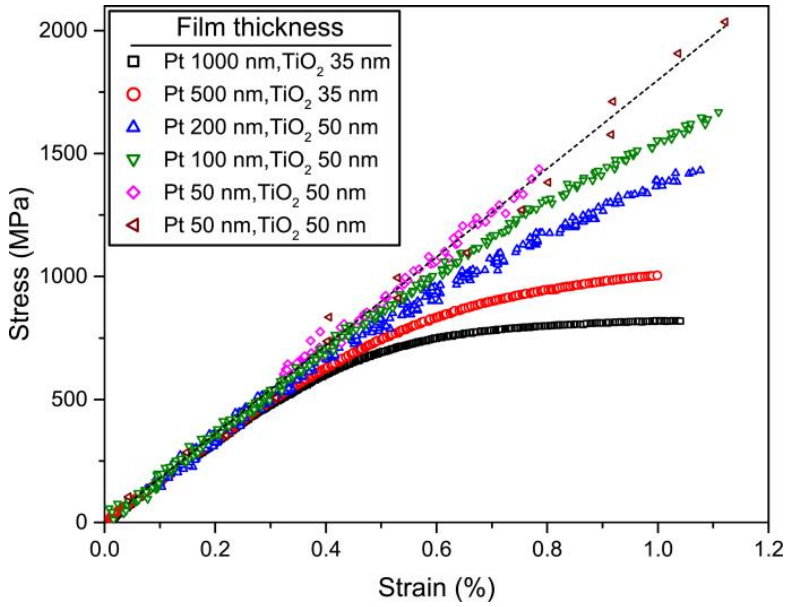

(a)

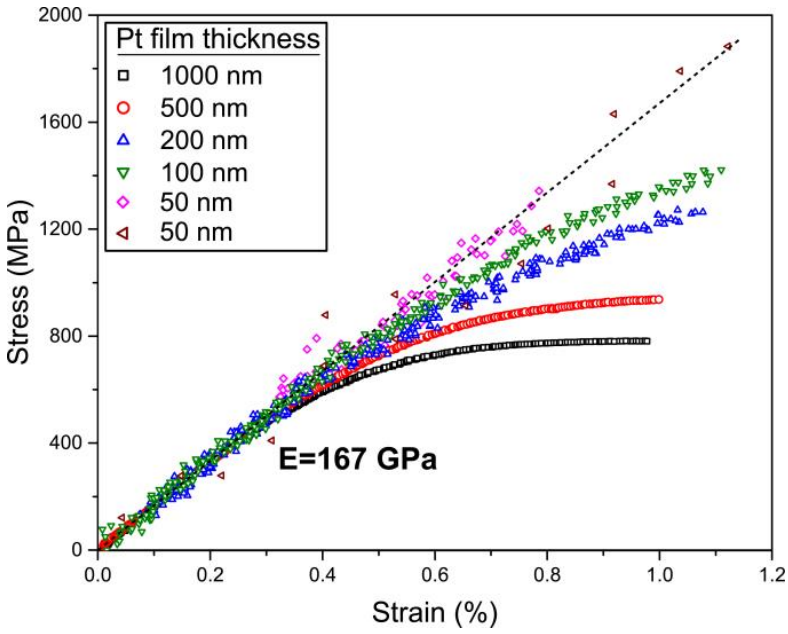

(b)

Figure 3.6 (a) Engineering stress-strain response of freestanding Pt/TiO_2 bilayers. **(b)** Engineering stress-strain response of freestanding {111}-textured Pt films vs. film thickness, as extracted from (a). Note that two experiments for 50-nm thick Pt films are included in (a,b): while one specimen failed early (diamonds), the second specimen (triangles) failed roughly at similar strain as all other Pt/TiO_2 bilayer specimens.

Table 3.2. Properties of Pt/TiO_2 bilayers.

Pt thickness (nm)	TiO_2 thickness (nm)	Elastic modulus of Pt/TiO_2 bilayer (GPa)	Failure Stress (MPa)	Failure Strain (%)
1000	35	168 ± 1	818 ± 3	1.03 ± 0.04
500	35	169 ± 2	986 ± 14	0.98 ± 0.02
200	50	172 ± 4	1401 ± 27	1.03 ± 0.04
100	50	177 ± 2	1643 ± 25	1.10 ± 0.02
50	50	180 ± 3	1736 ± 423	0.96 ± 0.23

Table 3.3. Compliance coefficients for Pt and rutile TiO_2.

Independent S_{ij} Cubic Symmetry	Values for Pt at 300 K [113] (TPa^{-1})	Independent S_{ij} Tetragonal Symmetry	Values for Rutile TiO_2 [114] (TPa^{-1})
S_{11}	9.12	S_{11}	6.82
S_{12}	-3.98	S_{12}	-4.06
S_{44}	13.78	S_{13}	-1.10
		S_{33}	3.24
		S_{44}	10.41
		S_{66}	5.28

3.3 Inelastic Response of Pt Films

The stress-strain curves for the Pt films were extracted from the stress-strain response of Pt/TiO_2 films assuming that the Pt and TiO_2 layers are under the same strain and the total applied force, P_{total}, is partitioned between the two layers as P_{Pt} and P_{TiO_2}.

The stress on the Pt layer is then obtained by subtracting the contribution of TiO_2 from the total applied force:

$$\sigma_{Pt} = \frac{1}{t_{Pt} w_{pt}} \left(P_{total} - P_{TiO_2} \right) \tag{3.4}$$

Equation (3.4) is valid as long as the TiO_2 layer remains elastic and the two layers remain perfectly bonded, even after Pt yielding. To this effect, the TiO_2 layer was inspected thoroughly and was found to be intact after specimen fracture, except very near to the region of specimen fracture. As a result, on average the TiO_2 layer deformed following the strain in the Pt layer, and remained elastic until failure of the composite film. Figure 3.6(b) shows the stress-strain response of Pt films with different thicknesses as derived via Equation (3.4). Figure 3.7(a) shows the proportional limit, and the 0.1% and 0.2% offset yield stress vs. the inverse Pt film thickness as extracted from Figure 3.6(b), following an increasing trend with decreasing Pt film thickness. The proportional limit was determined by using as metric the value of the coefficient of determination, R^2, for the fitted regression line of the initially linear segment of the stress-strain curve. Near the region where deviation from linearity occurs, the effect of the addition of individual experimental points to R^2 was monitored to determine the maximum value for R^2 as shown in the inset of Figure 3.7(b). The stress corresponding to maximum R^2 was identified as the proportional limit. The stress-strain data of the 200 nm and 100 nm thick films, which demonstrated larger scatter compared to thicker films, were first smoothed with the LOESS (locally weighted scatterplot smoothing) algorithm which utilized a local second-order polynomial regression by taking 30 points of a moving window. Subsequently, the proportional limit was determined by using the aforementioned R^2 approach, as shown in the inset in Figure 3.7(c) for a 100-nm thick Pt film. Notably, the proportional limit of many metals is the same, or slightly below the elastic limit [115]. The elastic limit of a polycrystalline aggregate is the stress at which local plastic deformation is initiated, and can be estimated by using the most favorable condition for slip following Schmid's law for plastic yielding [116], which would begin in grains where the resolved shear stress exceeds the local critical resolved shear stress.

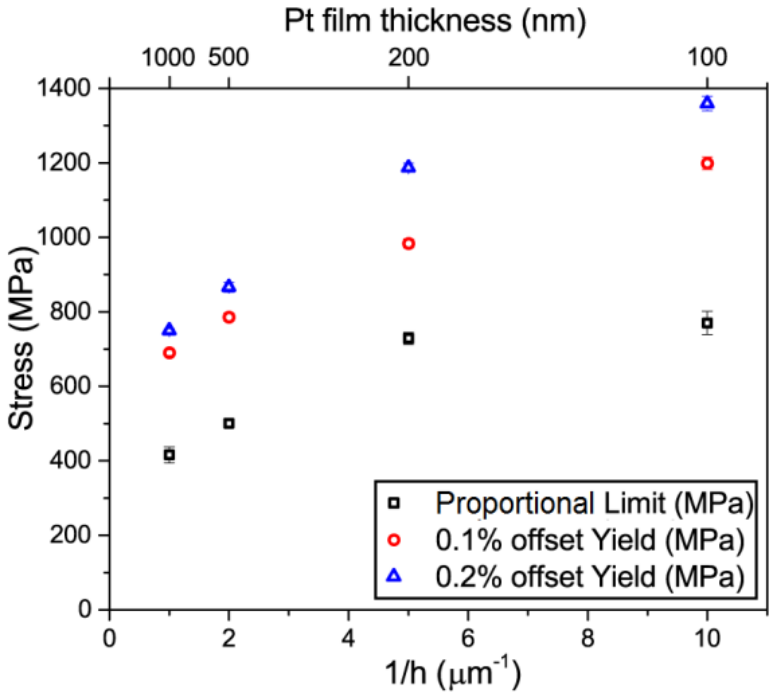

(a)

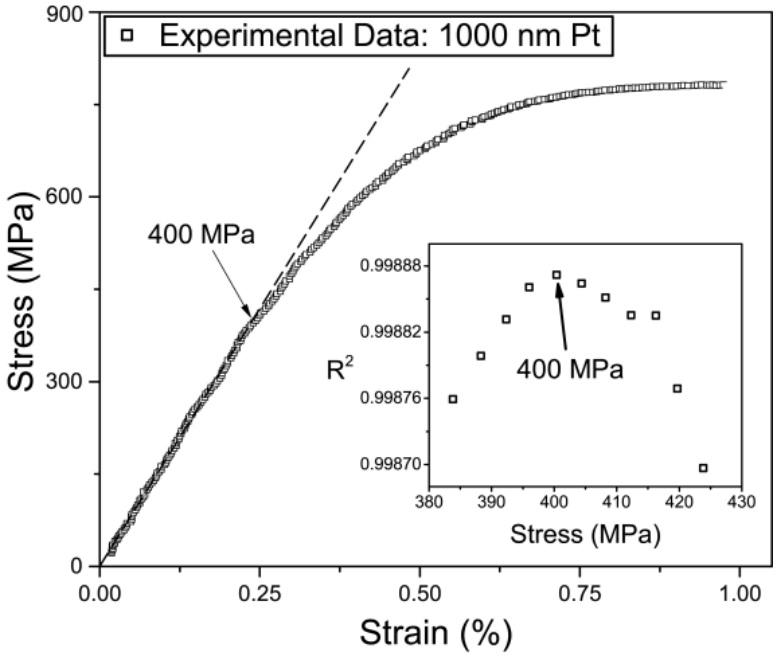

(b)

(figure continues on next page)

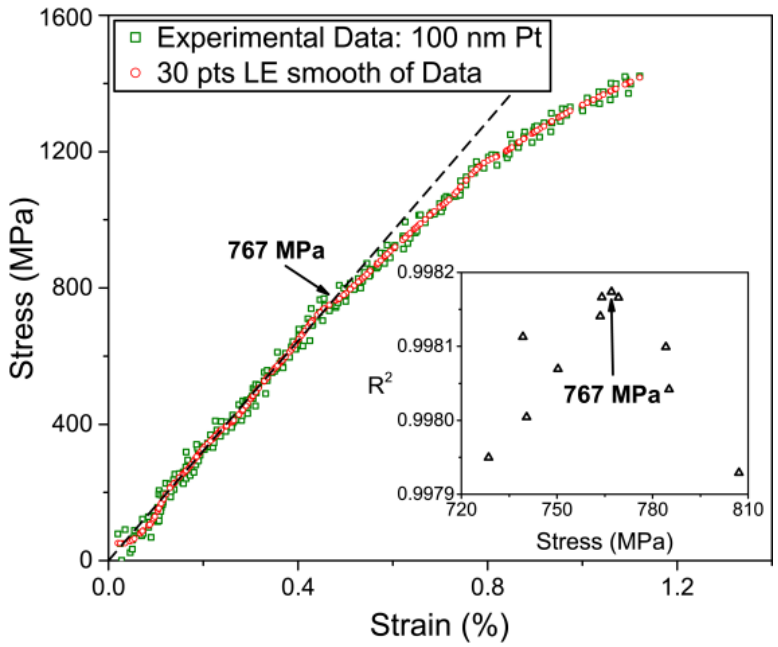

(c)

Figure 3.7. **(a)** Proportional limit, 0.1% and 0.2% offset yield stress vs. inverse Pt film thickness. Proportional limit of a **(b)** 1000 nm and **(c)** 100 nm thick film. Insets show the variation of the coefficient of determination, R^2, with stress with the maxima corresponding to proportional limit values.

3.3.1 Model for Initiation of Plastic Deformation

In polycrystalline metal films grown epitaxially on polycrystalline underlayers, the mismatch strain at the interface with the underlayer gives rise to an interfacial dislocation network. Under tensile stress, dislocation loops are emitted from the interface and glide along slip planes in the metal film, eventually depositing segments at GBs and interfaces that act as impenetrable obstacles to dislocation motion. Emission of such dislocation half-loops from film/substrate interfaces has been experimentally observed before during *in-situ* thermal cooling of epitaxial single crystal Cu films [26]: The thermal tensile stresses generated in Cu films during cooling caused the loops to expand and eventually lay down dislocation segments at twin-boundaries and interfaces. At the critical shear stress, the work done by the tensile forces should be just enough to deposit

the dislocation segments. The same idea was applied by Thompson to polycrystalline metal films bonded to rigid substrates with the exception that dislocations were considered to originate at defects at free surfaces of metal films rather than at the film/substrate interface. In particular, Thompson's model is applicable when the ratio of in-plane columnar grain diameter to height, *d/h*, is large, which applies to in-plane grain sizes that are roughly at least twice as large as the film thickness. Therefore, a modification to Thompson's model was necessary in the present study because (a) $d/h \leq 1$ for all Pt film thicknesses considered, Table 3.1, (b) the TiO_2 substrate is not rigid, and (c) dislocations generally emanate from the Pt/TiO_2 interface rather than the free surface. The premise of the modified Thompson's model is that a dislocation network already exists at grain-to-grain heteroepitaxial {111}Pt||(100)TiO_2 interfaces because of 6.34% mismatch strain [105] between Pt and TiO_2. It is assumed that the Pt/TiO_2 interface acts as a source of dislocations, the dislocation loops generated subsequently grow in the presence of tensile stress and also create additional segments at GBs and interfaces. The modification of Thompson's model for $d/h < 1$ used in this work was adopted from Carel [117] who considered truncated ellipses instead of rectangles for the intersection of glide planes with cylindrical columnar grains.

The derivation of the critical resolved shear stress according to modified Thompson's model is briefly reviewed here. An idealized right circular cylindrical grain with in-plane grain size d and height h, Figure 3.8, is subjected to tensile stress. A dislocation loop is emitted from the film/substrate interface and expands on a {111}-type glide plane which makes an angle φ with the Pt/TiO_2 interface. The work done by the stress field once the dislocation has swept through the slip plane in this grain is approximately given by [117]

$$W_{out} = (\tau S)b \tag{3.5}$$

where τ is the shear stress on the glide plane, b is the magnitude of the Burgers vector and S is the surface area of the glide plane given by [117]

$$S = AB(2\theta + \sin(2\theta)) \tag{3.6}$$

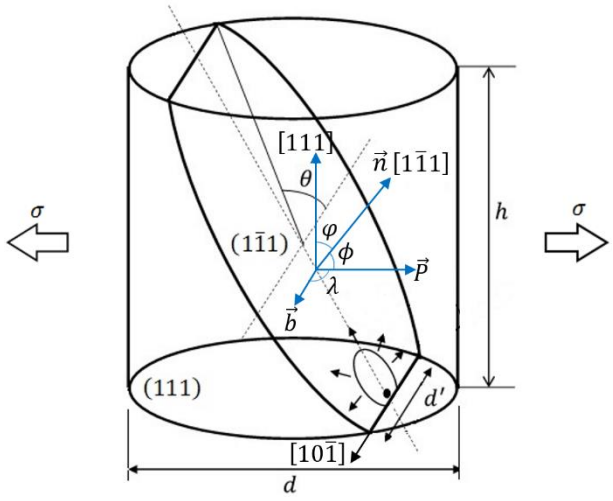

Figure 3.8 Schematic of dislocation glide taking place along a {111}-slip plane which forms a truncated ellipse when it intersects a cylindrical columnar grain. The loading direction is depicted as $\vec{P}$ and it makes angles ϕ and λ with the slip plane normal, $\vec{n}$ and the slip direction (Burgers vector), $\vec{b}$ respectively. The Burgers vector has been assumed to be parallel to $[10\bar{1}]$ direction because this leads to the maximum resolved shear stress on the $(1\bar{1}1)$ plane as discussed later.

The lengths of the semi-major and semi-minor axes A and B, respectively, are given by

$$A = d/(2\cos\varphi), \qquad B = d/2 \tag{3.7}$$

and the angle θ is defined as

$$\theta = \cos^{-1}\left(d'/\sqrt{d^2 + h^2}\right) \tag{3.8}$$

where

$$d' = \sqrt{d^2 - \frac{h^2}{\tan^2\varphi}} \tag{3.9}$$

As the dislocation loop expands, it deposits segments of interfacial dislocations on the Pt/TiO_2 interface, and eventually is blocked by GBs where additional segments are deposited. The side of the loop closer to the Pt/TiO_2 interface is deposited as interfacial segments until the other side expands freely and encounters the grain edges where additional segments are deposited. In such a case, the loop would look like a half-loop expanding in the metal film. The total energy of the dislocation in the final configuration is given by

$$W_{in} = LW_{side} + d'W_{bottom} \tag{3.10}$$

where L is the total length of the intercept of the glide plane with the cylindrical grain given by [117]

$$L = 4\int_0^{\theta} \sqrt{A^2\cos^2\gamma + B^2\sin^2\gamma}\; d\gamma \tag{3.11}$$

and W_{bottom} and W_{side} are the energies per unit length of the dislocation segments at the interface and at the edge of the grain.

For the geometry shown in Figure 3.8, the dislocation segment at the interface is a pure screw dislocation. Following the work by Nix [55] and Freund [118] the expression for the energy per unit length of the dislocation segment at the Pt/TiO_2 interface is given by

$$W_{bottom} = W_{screw,bottom}$$

$$= \frac{b_s^2}{4\pi}\frac{2\mu_f\mu_s}{\mu_f+\mu_s}\ln\left(\beta_s\frac{h\,h_s}{b_s(h+h_s)}\right) = \frac{b^2}{4\pi}\frac{2\mu_f\mu_s}{\mu_f+\mu_s}\ln\left(\frac{h\,h_s}{b(h+h_s)}\right) \tag{3.12}$$

where $b_s = b$, since the segment is a pure screw dislocation, β_s=1 is a numerical constant taken from the work of Nix [55], h_s is the thickness of the TiO_2 underlayer, μ_s and μ_f are the shear moduli of the TiO_2 underlayer and the film, respectively.

The expression for the exact energy per unit length of elliptical dislocation segments in a finite domain, as for example, the segments at the edges of the grain, is complex and difficult to compute. The energy depends not only on the self-energy of the segment which gets modified in the presence of image forces exerted by nearby free surfaces, but also on the interaction energy of the segment with other stress fields. Due to the complexity of the problem, it suffices to consider only the self-energy per unit length of elliptical segments in an infinite elastic medium. Analytic expression for the self-energy per unit length of an elliptically shaped loop in an elastic isotropic solid is given by [119]

$$W_{side} = \frac{E}{4AE(k)} = \frac{\mu_f b^2}{4\pi(1-\nu)}(1-\eta k)\ln\left(\frac{B}{r_o}\right) \approx \frac{b^2}{4\pi(1-\nu)}\mu_f \ln\left(\frac{d}{\mathrm{b}}\right) \tag{3.13}$$

where E is the self-energy, $4AE(k)$ is the circumference of the ellipse with $E(k)$ being the complete elliptic integral of the second kind, ν is the Poisson's ratio of Pt, η is an empirical parameter, k lies between 0 and 1 and depends on the orientation of the elliptical loop with respect to the Burgers vector, and r_o is the dislocation core radius. The self-energy per unit length can be approximated to the final expression by assuming η to be a small number and $r_o = b/2$. The final expression for the self-energy per unit length is identical to the one used in the Thompson model [56].

At the critical resolved shear stress, the work done by the stress field should be just enough for the dislocation half-loop to expand and deposit at GBs and the Pt/TiO_2 interface. Thus, by equating Equations (3.5) and (3.10), we have

$$\tau_{crit} = \frac{1}{Sb}(LW_{side} + d'W_{bottom}) \tag{3.14}$$

The stress generated as a result of uniaxial tension can be resolved into a shear stress on a {111}-type glide plane if the orientations of the slip plane and the slip direction with respect to the loading direction are known. Local yielding would result when the maximum resolved shear stress reaches the critical shear stress in Equation

(3.14). When uniaxial tension is applied to a {111}-textured Pt film, the maximum value of the resolved shear stress on a {111} plane is

$$\tau_{max} \approx 0.47\sigma \tag{3.15}$$

where σ is the stress due to uniaxial tension, as shown in Figure 3.8.

Equation (3.15) can be obtained as follows. Consider that the Pt film has (111)-fiber texture and is loaded in-plane along the $\left[\left(1+\sqrt{3}\right)\ \bar{2}\ \left(1-\sqrt{3}\right)\right]$ direction. Slip will occur on the $(1\bar{1}1)$ plane along the $[10\bar{1}]$ direction. The resolved shear stress is then found using the stress transformation, $\tau_{max} = \tau_{nb} = l_{ni}l_{bj}\sigma_{ij} = \sigma_{pp}l_{np}l_{bp}$ (no sum on p) $= \sigma(2/3)\left(1/\sqrt{2}\right) \approx 0.47\sigma$. The subscripts *n*, *b* and *p* are the slip plane normal, slip direction and loading direction, respectively, shown in Figure 3.8, while l_{np} and l_{bp} are the cosines of the angles between the directions denoted by the pair of subscripts. Similarly, slip will occur on the $(1\bar{1}\bar{1})$, $[0\bar{1}1]$ and $(11\bar{1})$, $[1\bar{1}0]$ systems when the loading direction coincides with the directions $\left[2\ \overline{(1+\sqrt{3})}\ \left(-1+\sqrt{3}\right)\right]$ and $\left[\left(1+\sqrt{3}\right)\ \left(1-\sqrt{3}\right)\ \bar{2}\right]$ respectively. In a (111)-textured polycrystalline Pt film with the (111) plane possessing infinite rotational symmetry because of the random in-plane orientation, there are always grains for which the loading direction aligns with $\left[\left(1+\sqrt{3}\right)\ \bar{2}\ \left(1-\sqrt{3}\right)\right]$, $\left[2\ \overline{(1+\sqrt{3})}\ \left(-1+\sqrt{3}\right)\right]$ and $\left[\left(1+\sqrt{3}\right)\ \left(1-\sqrt{3}\right)\ \bar{2}\right]$ directions and they undergo local plastic deformation. Finally, the elastic limit can be obtained by equating Equations (3.14) with (3.15):

$$\sigma_{elastic\ limit} \approx \frac{2.12}{Sb}\left(LW_{side} + d'W_{bottom}\right) \tag{3.16}$$

The underlying assumption in Equation (3.16) is that far-field uniaxial tension directly translates to the local stress around a cylindrical columnar grain. {111}-textured columnar grains exhibit in-plane isotropy. Thus, the stress is approximately uniform during elastic deformation of the present films even at the microstructural level, except of

course near the top and bottom surfaces. This assumption of stress uniformity holds until plastic deformation is initiated.

The expression for the length of the intercept of the glide plane with the cylindrical grain given by Equation (3.11) involves an elliptic integral of the second kind that is evaluated numerically. A Simpson discretization scheme as used by Carel [117] was applied for the numerical integration. The plots in Figure 3.9(a) show predictions of elastic limit, Equation (3.16), and the experimentally obtained proportional limit values (symbols) for Pt films, which are in good agreement. It can be inferred from the experimental data that the proportional limit and the elastic limit of Pt are not much different. The solid lines are computed with Equation (3.16) as a function of film thickness and constant grain size using $\mu_f = 61\,GPa,\ \mu_s = 76\,GPa,\ \nu = 0.38,\ b = 2.76\,\text{Å},$ and $\varphi = 70.5^\circ$ for {111}-textured Pt. It must be noted that Equation (3.16) can only be used for $h \leq d\tan\varphi$. For $h > d\tan\varphi$, the glide plane starting from the film/substrate interface doesn't reach the top surface of the film. Therefore, the dashed lines are simple extrapolations beyond $h = d\tan\varphi$. Figure 3.9(b) shows the contributions of the two energy terms, W_{side} and W_{bottom} to the elastic limit for films with 200 nm average grain size. As shown in Figure 3.9(b), the additive contribution of the two terms remains approximately constant beyond $h = d\tan\varphi$, because $d' \to 0$ as $h \to d\tan\varphi$, and L and S cannot increase further since the slip plane becomes confined inside the cylindrical grain as shown in inset (b) in Figure 3.9(b). Even if slip takes place along a parallel glide plane that does not start at the GB, as in shown in inset (c), the elastic limit will remain almost the same since the contribution of W_{side} will decrease but that of W_{bottom} will increase. As a result, broken horizontal lines are drawn beyond $h = d\tan\varphi$ signifying that the elastic limit would remain unchanged with further increase in film thickness. This prediction is confirmed by the experimental proportional limit values for 1000 nm and 500 nm thick films which fall on the broken lines, as shown in Figure 3.9(a), while there is good agreement with the experimental proportional limit values for 200 nm and 100 nm thick Pt films.

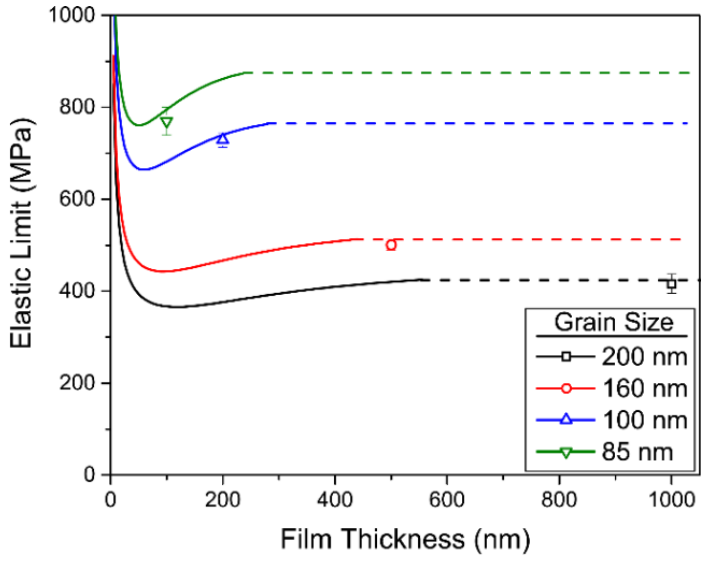

(a)

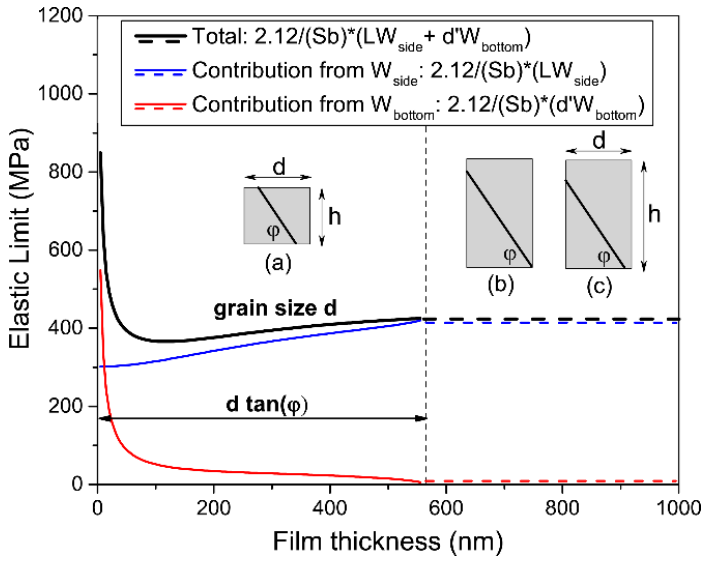

(b)

Figure 3.9 **(a)** Elastic limit of Pt films vs. film thickness. The solid lines are predictions of Equation (3.16). The dashed lines are extrapolations beyond $h = d\tan\varphi$. The experimental values (symbols) of the proportional limit agree well with the model predictions. **(b)** Elastic limit (solid black line) vs. film thickness for films with 200 nm average grain size. Insets (a), (b) and (c) depict cylindrical columnar grains with grain sizes and thicknesses d and h, respectively. {111}-type slip planes form an angle φ with the base of the cylinders. Inset (a) falls within the region covered by the theory whereas insets (b) and (c) represent cases where the slip-planes do not reach the top film surface. Blue and red lines show the contributions of the two energy terms and were extrapolated outside the region covered by theory.

3.3.2 Dislocation Nucleation at Film Surface due to Surface Roughness

In this analysis, dislocations were assumed to emanate from the Pt/TiO_2 interface due to the presence of a dislocation network at grain-to-grain heteroepitaxial {111}Pt||(100)TiO_2 interfaces. However, the top film surface roughness could also result in stress concentrations where dislocations would nucleate. This scenario is addressed by modeling the film surface roughness with a simple sinusoidal profile, $y(x) = a_o - A_0 \cos(2\pi x/\lambda)$, where A_0 and λ are the wave amplitude and wavelength, respectively, and a_o is an arbitrary constant. The maximum stress concentration factor, *SF*, corresponding to the most concave surface location, is given by $SF = 1 + 4\pi(A_0/\lambda)$ [120], decaying exponentially with depth. Setting the wave amplitude equal to the maximum valley depth recorded in AFM images and the wavelength equal to the average grain size, the stress concentration factors for films with different thickness are plotted in Figure 3.5(b). The 50 nm thick Pt films had the highest surface stress concentration factor of *SF*~2.5.

Following the analysis in [121], it can be shown that the local shear stress required for nucleation of a stable dislocation at the free film surface in the absence of thermal activation is $\tau = 2\mu_f m(2-\nu)/\left(\pi e^2(1-\nu)\right)$. Specifically, the energy of a semicircular loop of radius *R* emerging from the surface at the groove, Figure 3.10(a), is given by [121]

$$U^{semi} = \frac{\mu_f b^2 R}{8}\frac{(2-\nu)}{(1-\nu)}\ln\left(\frac{8mR}{e^2 r_o}\right) \tag{3.17}$$

The work done by the applied load is

$$W^{stress} = \frac{1}{2}\pi R^2 \tau' b \tag{3.18}$$

and the total energy is

$$E = \frac{\mu_f b^2 R}{8}\frac{(2-\nu)}{(1-\nu)}\ln\left(\frac{8mR}{e^2 r_o}\right) - \frac{1}{2}\pi R^2 \tau' b \tag{3.19}$$

Dislocation emission takes place when

$$\frac{\partial E}{\partial R} = 0;\ \frac{\partial^2 E}{\partial R^2} = 0 \tag{3.20}$$

which gives

$$\frac{\partial E}{\partial R} = \frac{\mu_f b^2}{8}\frac{(2-\nu)}{(1-\nu)}\ln\left(\frac{8mR}{er_o}\right) - \pi R\tau' b = 0\,;\ \frac{\partial^2 E}{\partial R^2} = \frac{\mu_f b^2}{8R}\frac{(2-\nu)}{(1-\nu)} - \pi\tau' b = 0 \tag{3.21}$$

Solving the last two equations simultaneously, the following result is obtained

$$\tau' = \frac{\mu_f bm}{\pi e^2 r_o}\frac{(2-\nu)}{(1-\nu)} \tag{3.22}$$

Setting $r_o = b/2$ we have:

$$\tau' = \frac{2\mu_f m}{\pi e^2}\frac{(2-\nu)}{(1-\nu)} \tag{3.23}$$

For uniaxial tension, $\sigma' = 2\tau'$. But, $\sigma' = S\sigma = S\sigma_{far\ field}$. Thus,

$$\sigma_{far\ field} = \frac{1}{S}\sigma' = \frac{4\mu_f m}{\pi S e^2}\frac{(2-\nu)}{(1-\nu)} \tag{3.23}$$

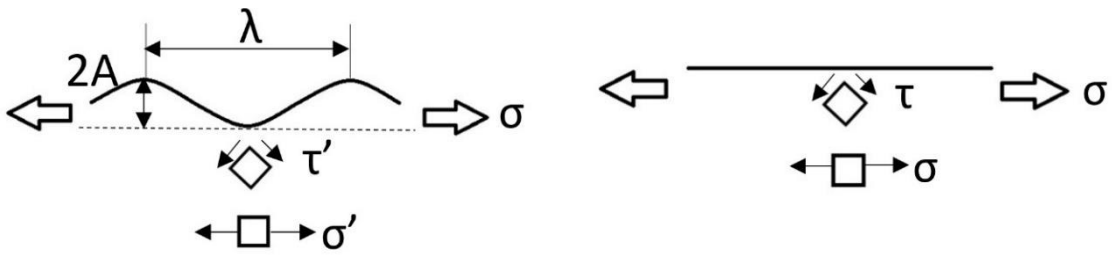

(a) **(b)**

Figure 3.10 (a) Stress concentration at the most concave location on the surface where $\sigma' = S\sigma$. Figure adapted from [120] with permission from Elsevier **(b)** There is no stress concentration on a flat surface.

Note that there is no stress concentration on a flat surface as shown in Figure 3.10(b).

For an applied uniaxial tension $\sigma_{far\ field}$, the local tangential stress at the root of a surface valley is $\sigma = SF\sigma_{far\ field}$ and the maximum resolved shear stress on a {111}-glide plane would be $\tau_{max} = 0.47\sigma$ according to in Equation (3.15). For $\tau = \tau_{max}$, $m = 0.5, e = 2.718$ and $SF = 2.5$ the minimum far field tension required for nucleation of a stable dislocation at a surface crevice is $\sigma_{far\ field} \approx 5.8\ GPa$, which is 4 times larger than the largest experimentally obtained 0.2% offset yield stress value corresponding to 100-nm thick Pt films. This result is not surprising as the surface roughness amplitude of the present films is very small compared to the roughness wavelength. Furthermore, experimental studies on FCC Pd nanowhiskers have reported uniaxial stress values for nucleation of surface dislocations in the range of 2-8 GPa [122]. Thus, only dislocations emanating from heteroepitaxial Pt/TiO_2 interfaces are considered in this study.

3.3.3 Prediction of Plastic Flow Stress

Although the modified Thompson model can describe the onset of yielding in textured Pt films with columnar grain structure, it underestimates the 0.1% and 0.2% offset yield stress values because the dislocation density evolves during deformation. For instance, there is experimental evidence for dislocation proliferation with increasing plastic deformation in Cu films [28]. The increase in dislocation density leads to interactions among dislocations causing strain hardening which, in turn, increases the flow stress. However, the modified Thompson model takes into account the motion of a *single* dislocation loop, and this underestimates the flow stress. Strain hardening as a result of interactions between gliding dislocations and arrays of stored dislocations depends on a number of factors which evolve with plastic strain, including density, type and spatial distribution of dislocations. A rough estimate of the additional strengthening due to the presence of a non-zero dislocation density as a result of plastic deformation can be obtained by Taylor's equation:

$$\Delta\sigma = \alpha M \mu_f b \sqrt{\rho_T} \tag{3.24}$$

where α is a constant with values in the range 0.3 – 0.6, M = 3.67 is the Taylor factor for {111}-fiber texture [123], and ρ_T is the average dislocation density. The latter may be represented as a combination of the density of geometrically necessary dislocations (GND) and the statistically stored dislocations (SSD). GNDs are stored at GBs during deformation to relax incompatibility stresses in adjacent grains. Following the work by Ashby [124], the density of GNDs as a function of plastic strain is given by

$$\rho_{GND} = \frac{N\varepsilon_{plastic}}{bd} \tag{3.25}$$

where $\varepsilon_{plastic}$ is the plastic strain and N = 2 for a two-dimensional columnar grain structure or N = 4 for three-dimensional grain structure. The density of SSDs is difficult to be analytically derived. There are several dislocation sources in a material, which may act independently or in a coordinated manner during deformation to increase the density of SSDs, e.g. *Frank-Read* sources or GB ledges may act as dislocation sources [125] to create a network of dislocations during plastic deformation, thus increasing the density of SSDs in each grain. For simplicity, it is assumed that at small length scales the two dislocation densities are comparable, $\rho_{GND} \sim \rho_{SSD}$ [126]. Therefore, the total average dislocation density is given by

$$\rho_T = \rho_{GND} + \rho_{SSD} = \frac{2N\varepsilon_{plastic}}{bd} \tag{3.26}$$

A similar approach was adopted by Hommel and Kraft [28] who inferred from an X-ray FWHM analysis the total dislocation density as a function of grain size and plastic strain in 1 μm thick Cu films deposited on a polyimide substrate. It may be noted that Equation (3.26) does not have any material parameters except for the Burgers vector which does not vary much for FCC metals. A good agreement has been confirmed between the dislocation densities predicted by Equation (3.26) and those measured in Cu by Hommel and Kraft [28], and as a result, the same equation is used here to predict the average dislocation density in Pt films vs. plastic strain and grain size.

Adding the stress increment due to the Taylor strain hardening mechanism given by Equation (3.24) to the stress required to initiate plasticity provided by the modified Thompson model in Equation (3.16), the total flow stress becomes:

$$\sigma_{flow} = \sigma_{elastic\ limit} + \alpha M \mu_f b \sqrt{\rho_T} \approx \sigma_{elastic\ limit} + \alpha M \mu_f \sqrt{\frac{2Nb\varepsilon_{plastic}}{d}} \tag{3.27a}$$

$$\begin{aligned} \sigma_{flow} &\approx \sigma_{elastic\ limit} + \frac{k(\varepsilon_{plastic})}{\sqrt{d}}; where\ k(\varepsilon_{plastic}) \\ &= \alpha M \mu_f \sqrt{2Nb\varepsilon_{plastic}} \end{aligned} \tag{3.27b}$$

The evolution of flow stress with plastic strain as predicted by Equation (3.27a) can be verified by fitting it to the experimental stress-plastic strain data. Figure 3.11 shows a moderately good quantitative agreement for different film thicknesses for $\alpha = 0.47$. It may be noted that, for the thicker films, Equation (3.27) overestimates the flow stress beyond 0.2 % plastic strain. This may be due to the lack of an inbuilt recovery process in the model such as dislocation annihilation.

Equation (3.27a) can be rewritten as Equation (3.27b) to emphasize that the strain hardening model reduces to the Hall-Petch grain-size strengthening model with the Hall-Petch coefficient becoming a function of plastic strain. This approach of obtaining the Hall-Petch slope by removing the grain size dependent term from the dislocation density function is also found in a study by Hansen [127]. The value used for the single fitting parameter $\alpha = 0.47$ in Equation (3.27a) is justified if the Hall-Petch coefficient calculated by Equation (3.27b) for 0.2% plastic strain agrees well with the literature data: Specifically, the Hall-Petch coefficient $k(\varepsilon_{plastic})$ computed for 0.2% plastic strain of Pt films is 0.16 $MPa\sqrt{m}$ which compares well with the value of 0.18 $MPa\sqrt{m}$ reported in literature [71].

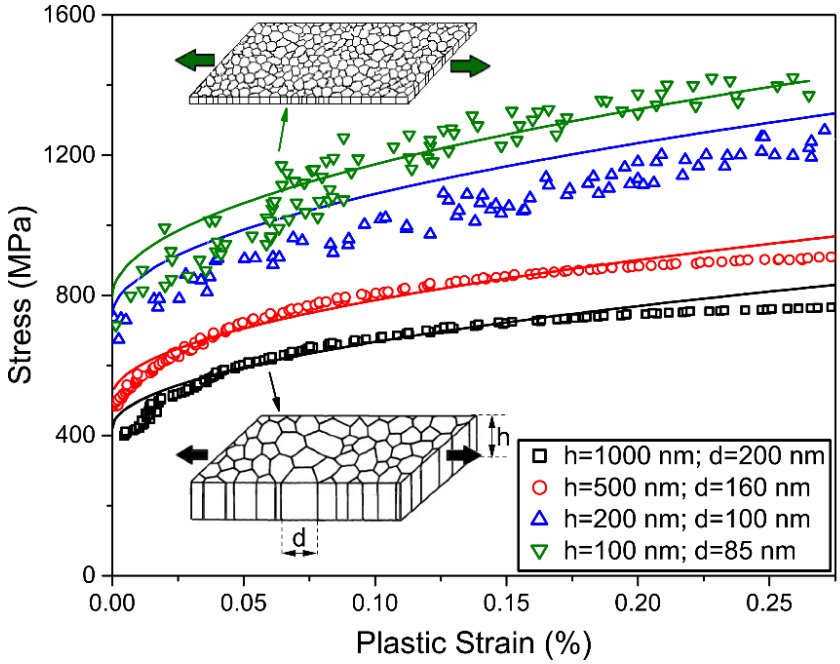

Figure 3.11 Experimental flow stress vs. plastic strain for Pt films. The prediction by Equation (3.27) is represented by the solid lines with good agreement with experiments (symbols). The lowermost curve corresponds to the thickest film with the largest grain size whereas the uppermost curve corresponds to the thinnest film with the smallest grain size.

3.4 Strain Rate Sensitivity of Pt/TiO_2 Films

Notably, the strain at failure was consistent (~1%) for Pt/TiO_2 films of different thickness but the plastic strain at failure of Pt decreased with decreasing Pt film thickness: Computed from the data in Figure 3.6(b), the plastic strain accumulated in 1000 nm, 500 nm, 200 nm, 100 nm and 50 nm thick Pt films, was 0.5%, 0.4%, 0.3%, 0.25% and ~0%, respectively. Figure 3.12(a-c) shows the fracture profiles of 1000 nm, 500 nm and 100 nm thick Pt films. Figure 3.12(d) shows strain localization in a 1000 nm thick film, whereas 500 nm thick films demonstrated intergranular cleavage, as shown in Figure 3.12(e). Figure 3.12(f) shows that cracks in the TiO_2 layer formed only near the bilayer fracture zone while the rest of the TiO_2 layer remained crack-free until specimen

failure. This result supports the use of isostrain and elastic behavior for the TiO_2 layer in computing the strain in Pt by Equation (3.4).

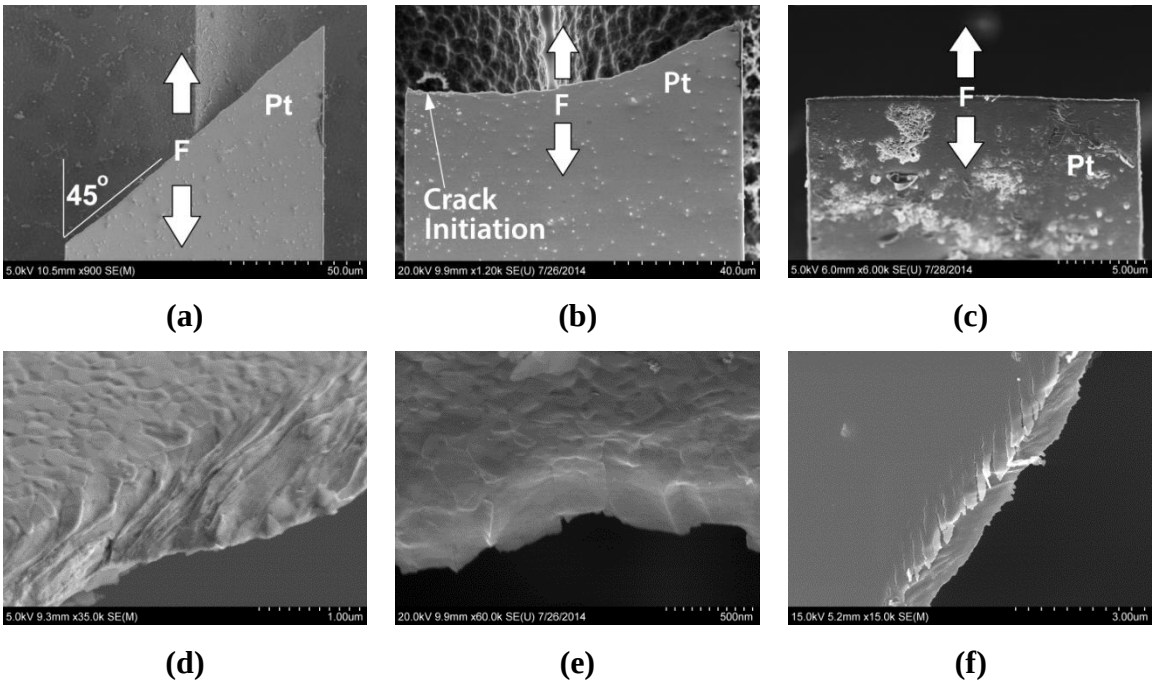

(a) **(b)** **(c)**

(d) **(e)** **(f)**

Figure 3.12 Fracture profiles for Pt specimens with **(a)** 1000 nm, **(b)** 500 nm, and **(c)** 100 nm thickness. The loading direction is denoted by the arrows. **(d)** Strain localization in a 1000 nm thick specimen. **(e)** Intergranular cleavage of a 500 nm thick specimen. **(f)** Cracks in the TiO_2 layer very near to the fracture surface of the Pt/ TiO_2 bilayer, while the rest of the TiO_2 layer was damage-free.

The failure of 1000 nm and 500 nm thick films was controlled by the Pt layer. The failure mechanism in the thicker films can be understood by considering the grain size distribution of Pt. For broad grain size distributions, small grains have higher yield strength compared to larger grains, resulting in non-uniform local deformation. Compared to thinner films, the 1000 nm thick Pt films had much broader grain size distribution and larger mean grain size. Under tension, strain localized in the larger grains which allowed for the development of plastic deformation in regions of maximum shear. Evidence for this process is shown in Figure 3.12(d). Such a mechanism for strain localization is strain rate dependent. Figure 3.13(a,b) show engineering stress vs. strain

curves for 1000 nm and 500 nm thick Pt films subjected to tensile strain rates between 2×10^{-6} s^{-1} and 6 s^{-1}. Notably, in this range of strain rates, the failure strain increased with increasing strain rate by as much as 30%, which is not typical for metals. Such an anomalous behavior may occur due to more uniform plastic flow with increased strain rate as a result of suppression of strain localization and increased small scale yielding taking place at high strain rates. This was argued before by Rupert [128] based on molecular-dynamics simulations of nanocrystalline Ni. Post-mortem fracture surface imaging supports this argument as shown in Figure 3.14(a,b) where increased strain localization at slower strain rates lead to smaller engineering strain. However, the yield stress increased only slightly with strain rate. The strain rate sensitivity of 1000 nm thick Pt films was low, ~0.01. Such small values would promote strain localization as observed experimentally. The 500 nm thick Pt films showed further reduced sensitivity to strain rate with the yield stress practically remaining unchanged.

A reduction in Pt film thickness resulted in narrower grain size distribution and decreased mean grain size, which, in turn, impacted plastic deformation: 50 nm thick Pt films demonstrated brittle fracture, which may be due to a change in deformation mechanism from full to partial dislocations as reported before for Al [129], Au [130] and Ta/Cu [131] films with thicknesses in the range of 40-100 nm. The stress required to nucleate partial dislocations accompanying a stacking fault are smaller than those required to full dislocations when the grain size or film thickness falls below a critical size. The resulting partial dislocations are harder to cross-slip and provide an additional constraint to dislocation motion.

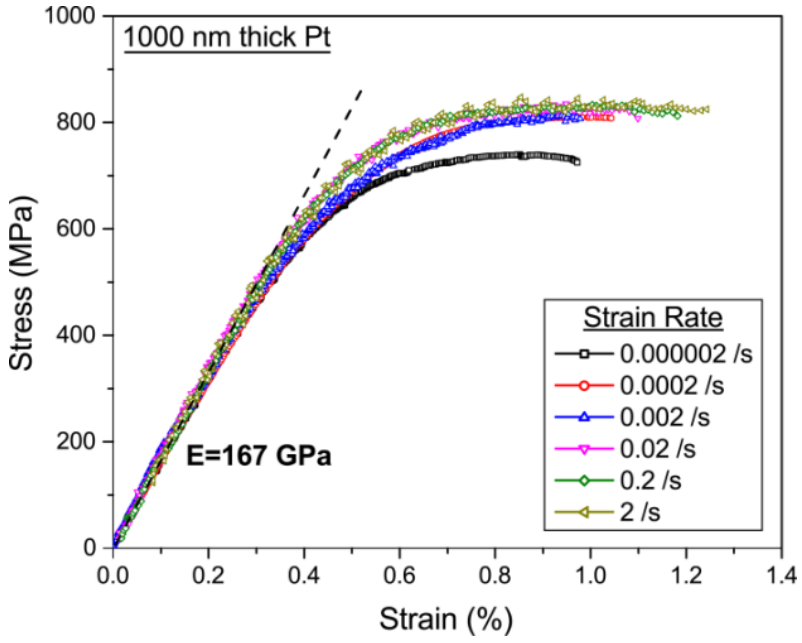

(a)

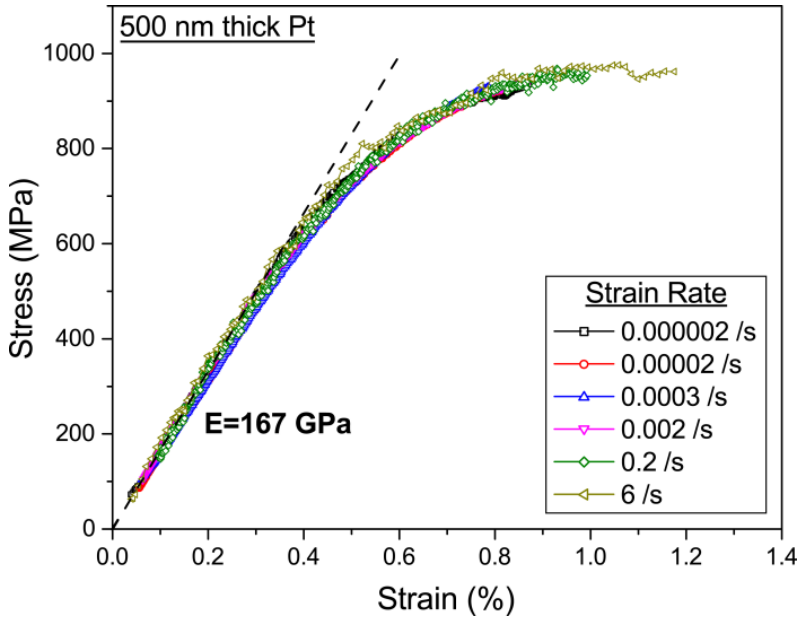

(b)

Figure 3.13 Engineering stress vs. strain curves for **(a)** 1000 nm and **(b)** 500 nm thick Pt films subjected to various strain rates.

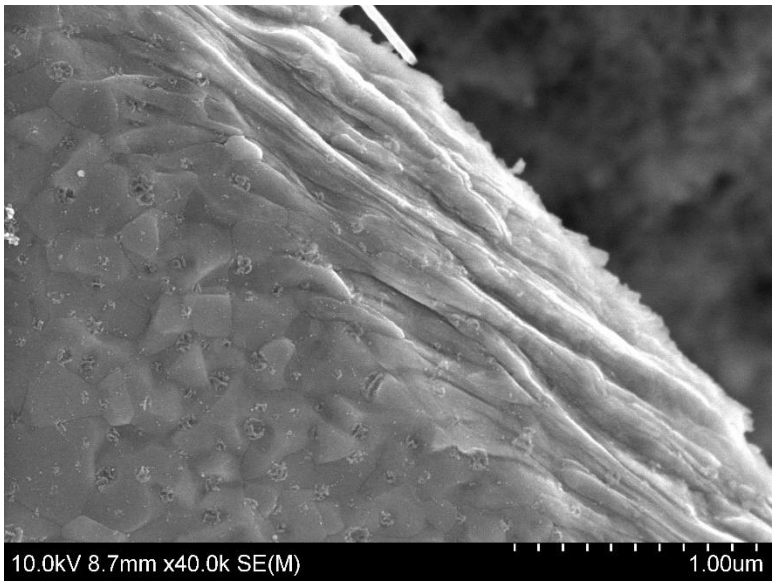

(a)

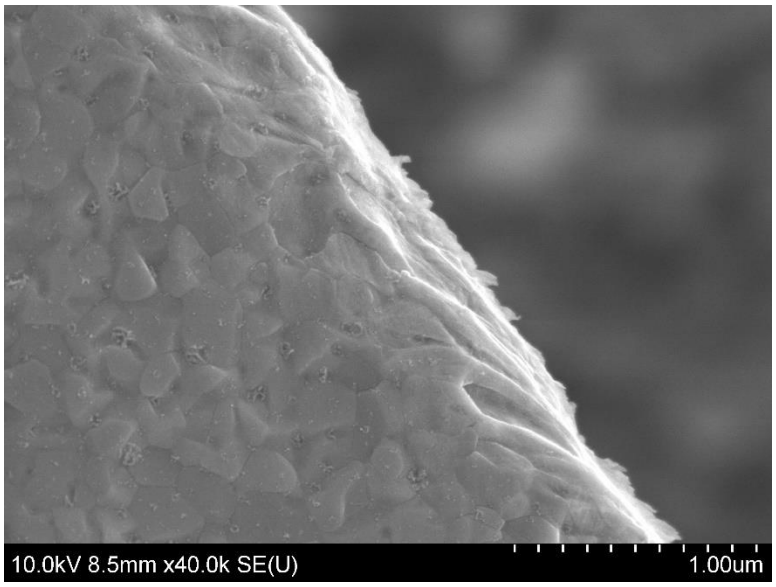

(b)

Figure 3.14 Strain localization in 1000 nm thick Pt films, tested at the **(a)** strain rate of 10^{-6} s^{-1}, and **(b)** 10^{-2} s^{-1}.

3.5 Conclusions

The effect of film thickness and grain size on the mechanical response of freestanding nanocrystalline {111}-textured Pt films epitaxially grown on rutile TiO_2 seed substrates with columnar grain structure was experimentally and analytically investigated for Pt/TiO_2 bilayer films with thicknesses in the range of 100 to 1000 nm. The measured elastic modulus of Pt (E_{Pt}=167 ± 2 GPa) agreed well with theoretical estimates for the in-plane modulus of {111}-textured polycrystalline Pt, while the modulus of TiO_2 (E_{TiO_2}=195 ± 5 GPa) was 15% lower than the theoretical estimate for (100)-textured polycrystalline TiO_2. The flow stress of Pt/TiO_2 films increased with reduced thickness. The experimentally determined proportional limit of Pt was consistent with predictions by a modified Thompson model for plastic deformation of polycrystalline columnar metal thin films. However, the yield stress was underestimated by the same model, and a Taylor strain hardening model was superimposed to the modified Thompson model to account for additional hardening occurring as a result of dislocation interactions during plastic deformation. The combined model, which is also a Hall-Petch grain strengthening model, predicted well the evolution of flow stress with plastic strain.

CHAPTER 4

Mechanical Response of Textured PZT Films

Piezoelectric lead zirconate titanate (PZT) films find use in several types of MEMS [1-6]. Perovskite ferroelectric materials are strongly anisotropic, therefore, control of their grain orientation is critical for improved electromechanical properties [29] and enhanced low voltage actuation. Several studies [29,30] have reported improved piezoelectric coefficients, $e_{31,f}$ and $d_{33,f}$ of {100} oriented polycrystalline PZT films at the morphotropic phase boundary (MPB), demonstrating that the intrinsic response of PZT associated with ionic deformation of unit cells depends on texture. There has been a recent focus on orientation control of polycrystalline PZT films and thus, their piezoelectric and dielectric properties [33,44-46,51]. However, few studies [8-11] have probed the dependence of mechanical properties on film texture with good control of the latter. To date, only a handful of publications [8-10] have reported, mostly using nanoindentation, the directional dependence of Young's modulus of PZT thin films on {001}, {110} and {111} preferred orientation, as shown in Figure 4.1 and Table 4.1. The indentation test results in Figure 4.1, taken from [84] show strong scatter in values, which may be due to the roughness of the sample surface. Bulk PZT has Young's modulus of 68 GPa [14]; comparatively speaking the results in Figure 4.1 and Table 4.1 for PZT thin films measured through nanoindentation are quite high, and the following directional relationship of elastic modulus has been observed [84]: $E_{<100>} = E_{<110>} < E_{<111>} < E_{<001>}$.

For PZT films incorporated as a stack multimorph with several layers of dielectric, piezoelectric, elastic and conductors on a substrate, the piezoelectric coefficient of interest, $d_{31,f}$ depends on the elastic properties of PZT and the other

materials forming the stack [21,22]. Inaccuracies in the determination of the elastic modulus subsequently precipitate in d_{31} calculations. It has been noted [20] that disparities among the published d_{31} values could be the result of different elastic moduli used in calculations.

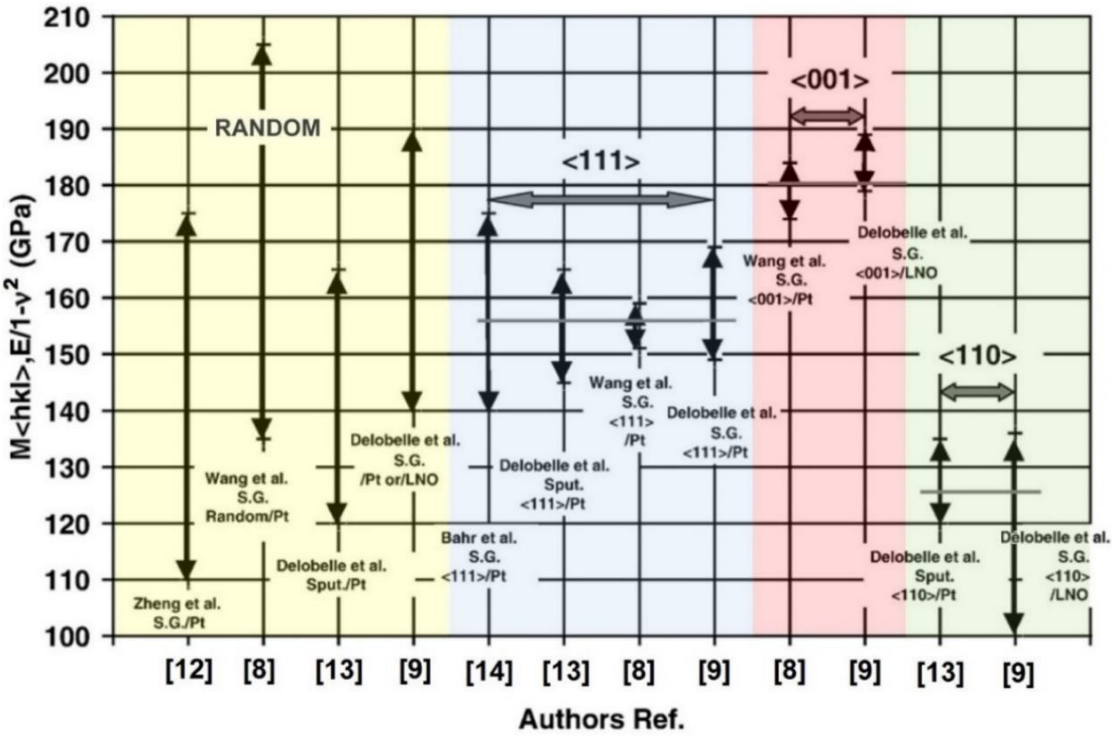

Figure 4.1. Indentation moduli obtained by various studies showing a general trend of $E_{<110>} < E_{<111>} < E_{<001>}$. There is pronounced scatter in results with the random texture demonstrating the largest scatter. Figure adapted from [84] with permission from Elsevier.

More importantly, there are no prior studies on the effect of texture on ferroelasticity[††] of PZT films and the associated non-linearity in the mechanical behavior. The work in this Chapter addresses the lack of quantitative information about the open circuit elastic and ferroelastic behavior of polycrystalline PZT films as a function of

[††] Ferroelasticity is an extrinsic property exhibited by ferroelectrics where non-180° domain switching is induced by mechanical stresses.

texture, with measurements conducted on freestanding PZT thin film stacks. PZT films at the MPB (52/48) with 0-10% excess Pb were deposited on $PbTiO_3$ seed layers with 0-30% excess Pb which in conjunction with the texture of the underlying Pt film controlled the PZT texture.

Table 4.1. Directional dependence of PZT modulus. Table adapted from Ref. [132]

Thin film structure	Elastic or Indentation Modulus	Test Method
Si(100)/SiO_2/Ti/Pt(111)/PZT 1 µm thick sol-gel deposited PZT films with (001), (111) and random orientations obtained under different thermal treatments and using different solvents.	$E_{<001>}$ = 165 GPa $E_{<111>}$ = 145 GPa E_{random} = 125-190 GPa	Nanoindentation [8]
Si/SiO_2/TiO_x/Pt/PZT Si/SiO_2/$LaNiO_3$(001)/PZT 0.5 µm - 3.8 µm thick sol-gel deposited PZT films with (001), (110) and (111) preferred orientations obtained by varying the bottom electrode, film thickness, and precursor solution.	$M_{<001>}$ = 180 ± 5 GPa $M_{<110>}$ = 125 ± 10 GPa $M_{<111>}$ = 156 ± 8 GPa	Nanoindentation [9,84]
Si(100)/SiO_2/Ti/Pt(111)/PZT 0.2 µm thick sol-gel deposited PZT films with (100), (111) and random orientations obtained under different thermal treatments.	$M_{<100>}$ = 146.5 GPa $M_{<111>}$ = 161.2 GPa $M_{<random>}$ = 155.3 GPa	Nanoindentation [10]
MgO(100)/(100)Pt/PZT/Pt 3.6 µm thick RF magnetron sputtered PZT films with (001) epitaxial PZT.	$s_{11}^E = 10.8\times10^{-12}$ m^2/N $E_{(001)}$ = 92 GPa [47]	Resonance [11]

Although (111) and (001) textured PZT films have been fabricated in the past [34,39], it has not been possible to control their texture without modifying the seeding layer [33,47]. Furthermore, in prior studies, the PZT films were bonded to thick Si substrates, which prevented the direct measurement of their mechanical behavior and required precise knowledge of the mismatch stresses [35,37]. The present PZT films were implemented as composite stacks forming d_{31} type actuators. The stacks had an elastic SiO_2 layer, TiO_2 serving as an adhesion layer, Pt as the metallization layer, a $PbTiO_3$ (PTO) seed layer, the PZT (52/48) layer, another Pt metallization layer, and finally an ALD layer consisting of Al_2O_3 and HfO_2. The thin PTO seed layer could not be distinguished from the PZT layer in cross-section micrographs such as the one shown in Figure 4.2, and therefore, the PTO-PZT layer is henceforth referred to as the PZT layer. The measured thicknesses of the SiO_2, TiO_2, bottom Pt, top Pt, and ALD layers were 300 nm, 35 nm, 100 nm, 50 nm and 75 nm, respectively. The entire stacks were of the sequence SiO_2-TiO_2-Pt-PZT-Pt-ALD. Several layer combinations, such as TiO_2-Pt, SiO_2-TiO_2-Pt, SiO_2-TiO_2-Pt-PZT, and SiO_2-TiO_2-Pt-PZT-Pt-ALD, were tested in uniaxial tension to deduce the properties of each individual layer and, in turn, compute the Young's modulus of PZT films with different textures in open circuit conditions.

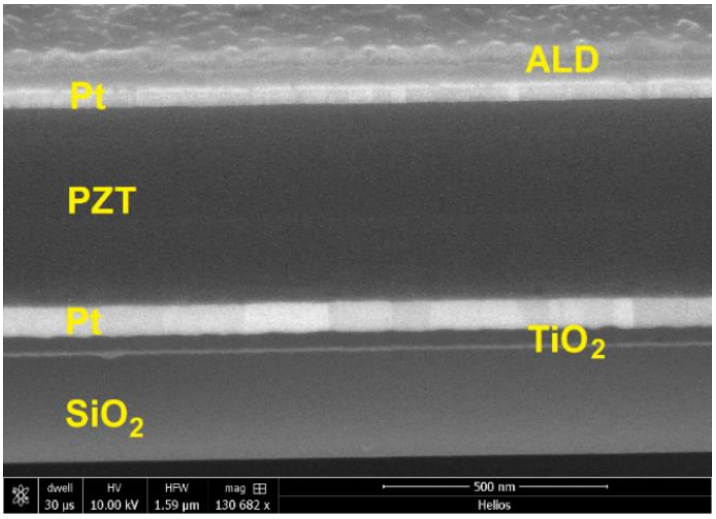

Figure 4.2. Cross-section of Sample #6019 with 100% (001) texture showing the layers of a SiO_2-TiO_2-Pt-PZT-Pt-ALD stack.

4.1 Experimental Methods

The test specimens were fabricated at the US Army Research Laboratory (ARL) using chemical solution deposition as detailed in [133]. A highly {111} textured 100 nm Pt layer was deposited using magnetron sputtering onto 35 nm highly {100} textured TiO_2 film that was grown on 300 nm thick SiO_2. Then, 20 nm $PbTiO_3$ seed layers containing 0-30% excess Pb were prepared using the 2-Methoxyethanol (2-MOE) synthesis route. PZT(52/48) solutions with 0-10% excess Pb were then spun-cast and pyrolyzed on the $PbTiO_3$ seed layers according to the 2-MOE synthesis route, similarly to Ref. [134]. The total thickness of the pyrolyzed PZT was ~500 nm. Ar ion milling followed by wet etching were used to pattern the PZT layer, and reactive ion etching via fluorine plasma was performed on the elastic layer to enable access to the Si substrate for the final release. Finally, isotropic XeF_2 etching released the freestanding 1000 μm long, 100 μm wide and ~1 μm thick dog-bone specimens for mechanical testing. Focused ion beam (FIB), scanning electron microscopy (SEM), and X-ray diffraction (XRD) studies were conducted to determine the thickness, average grain size, and texture of the PZT films, respectively as reported in Table 4.2.

Figure 4.3(a) shows X-ray 2theta-omega scans for samples #6006, #6109 and #6020. Sample #6006 shows only (111) PZT peaks, whereas #6020 shows only (001) PZT peaks. Sample #6109 on the other hand, shows (001), (110) and (111) peaks. In addition to 2theta-omega scans, rocking curve measurements revealed preferred (001), (110) and (111) textures. The FWHM values for (001), (110) and (111) peaks were $\leq 5^{\circ}$, $\leq 3^{\circ}$ and $\leq 8^{\circ}$, respectively, indicating moderately good alignment of these planes relative to the film surface. Pole figure plots for (001), (110) and (111) peaks show concentrated intensity distributions at the center and an encircled ring around the (110) peak indicating fiber texture.

Various methods have been applied before to quantify the degree of preferred orientation using XRD [135-138]. The XRD method employed in this study compared the intensities of the thin-film $\theta/2\theta$ diffraction pattern with those of a powder sample exhibiting random orientation. The integrated intensities of a powder sample may be obtained from standard PDFs from the International Centre for Diffraction Data (ICDD).

The standard PDF#01-070-4060 was used to quantify the relative degrees of preferred orientations in the films.

Table 4.2. Thickness of PZT layers in SiO_2-TiO_2-Pt-PZT stacks and percentage of texture factors.

Sample#	%Pb-excess $PbTiO_3$	%Pb-excess PZT	PZT Thickness (nm)	PZT grain size (nm) [133]	% T_{001}	% T_{110}	% T_{111}
6117	0	0	500	-	21	20	59
6109	0	3	520	74 ± 2	44	17	39
6101	0	5	540	125 ± 3	15	15	70
6103	0	10	500	-	9	23	68
6006	10	3	520	79 ± 2	0	0	100
6015	10	5	550	79 ± 2	19	0	81
6017	20	3	520	73 ± 4	0	0	100
6155	20	5	520	111 ± 2	25	18	57
6001	20	8	550	121 ± 1	78	22	0
6113	30	3	525	-	73	0	27
6019	30	5	525	103 ± 2	100	0	0
6020	30	8	505	93 ± 2	100	0	0
6122	30	10	525	84 ± 3	59	0	41

The texture factor [136] was evaluated as a measure of the degree of enhancement or reduction in the *hkl* reflection due to preferred orientation when compared to a powder sample, given by

$$T_h = \frac{I_h^F / A_{\theta 2\theta}(\theta_h)}{I_h^{ICDD}} \frac{\sum_{h'} I_{h'}^{ICDD}}{\sum_{h'} \left(I_{h'}^F / A_{\theta 2\theta}(\theta_{h'}) \right)} \tag{4.1}$$

where I_h^F is the integrated intensity for diffraction from a *hkl* plane in a thin film, I_h^{ICDD} is the integrated intensity for diffraction from the same *hkl* plane in a standard random

powder, $A_{\theta 2\theta}(\theta_h)$ is the absorption factor at the Bragg angle θ_h and $\sum_h I_h$ is to the sum of the integrated intensities from all reflections. Since three preferred orientations were present, the (001) percentage texture factor, for example, was computed as:

$$\%\, T_{001} = \frac{\frac{I^F_{001}/A_{\theta 2\theta}(\theta_{001})}{I^{ICDD}_{001}}}{\left(\frac{I^F_{001}/A_{\theta 2\theta}(\theta_{001})}{I^{ICDD}_{001}} + \frac{I^F_{110}/A_{\theta 2\theta}(\theta_{110})}{I^{ICDD}_{110}} + \frac{I^F_{111}/A_{\theta 2\theta}(\theta_{111})}{I^{ICDD}_{111}}\right)} \tag{4.2}$$

In Equation (4.2) the absorption factor $A_{\theta 2\theta}$ is defined as [136]:

$$A_{\theta 2\theta}(\theta_h) = \left(1 - e^{-\frac{2\mu t}{\sin\theta_h}}\right) \tag{4.3}$$

where μ is the linear absorption coefficient, and t is the film thickness. The linear absorption coefficient can be calculated from the mass absorption coefficients, μ/ρ [139] at photon energies of 8.23 keV for Cu K_α radiation, and weight fractions, w, of the elements contained in the crystallized thin film according to [137]:

$$\begin{aligned}\frac{\mu_{PZT}}{\rho_{PZT}} = 0.52&\left(w_{Pb}\left(\frac{\mu_{Pb}}{\rho_{Pb}}\right) + w_{Zr}\left(\frac{\mu_{Zr}}{\rho_{Zr}}\right) + w_O\left(\frac{\mu_O}{\rho_O}\right)\right)_{PbZrO_3} \\ &+ 0.48\left(w_{Pb}\left(\frac{\mu_{Pb}}{\rho_{Pb}}\right) + w_{Zr}\left(\frac{\mu_{Ti}}{\rho_{Ti}}\right) + w_O\left(\frac{\mu_O}{\rho_O}\right)\right)_{PbTiO_3}\end{aligned} \tag{4.4}$$

For ρ_{PZT} = 7.83 g/cc, it is found that μ_{PZT} = 1325 cm^{-1}. For this value of μ_{PZT} and the integrated intensities of the diffraction peaks from the sample and the powder standard along with the Bragg angles and film thicknesses, the percentage texture factors were calculated, Table 4.2. Figure 4.3(b) shows the percentage (001) texture factors for the excess lead concentrations in the $PbTiO_3$ and PZT layers: in general, increasing excess-Pb in the $PbTiO_3$ seed layer increases the (001) texture, as also reported elsewhere [46] and discussed in Section 1.2.

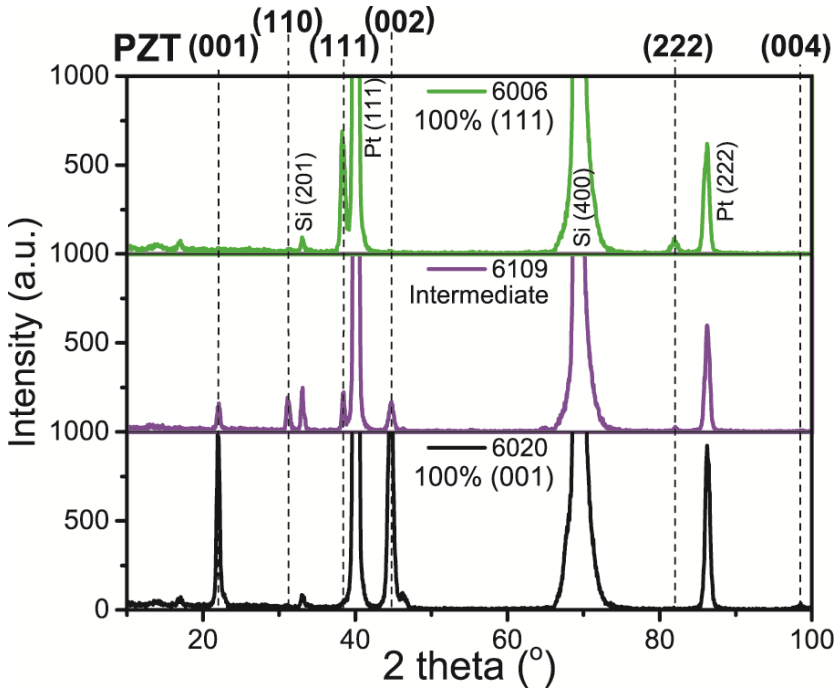

(a)

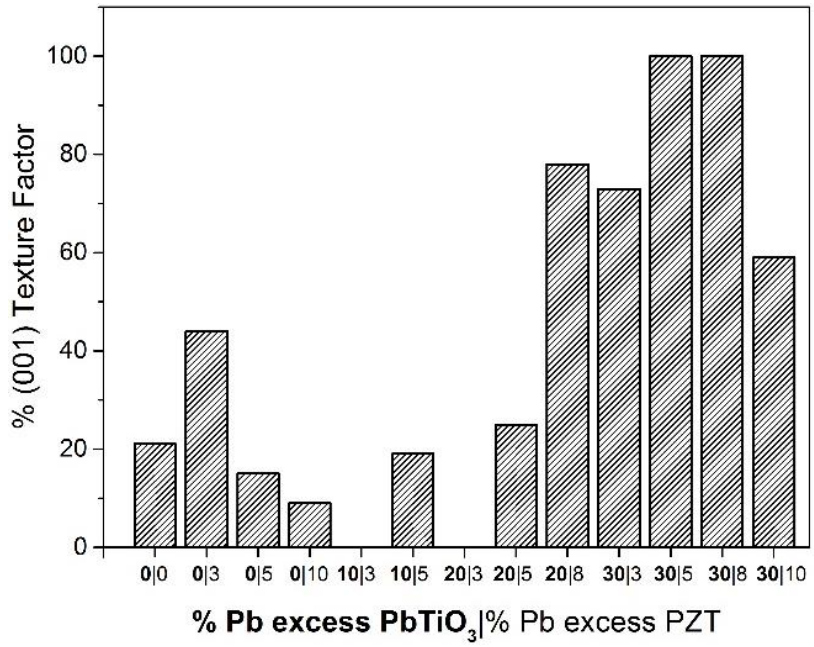

(b)

Figure 4.3. **(a)** XRD showing (001), (110) and (111) PZT textures. **(b)** (001) texture factor vs. content of excess Pb. The excess Pb percentages in the $PbTiO_3$ and PZT layer in the x-axis are separated by a vertical bar.

4.2 Stress-strain Response of Textured PZT Films

A custom-built apparatus for microscale uniaxial tension experiments with freestanding thin films, as described in detail in Section 2.2, was used to test the microscale thin film specimens under an optical microscope at 10^{-4} s^{-1} strain rate.

Uniaxial tension experiments were performed to extract the elastic modulus of the individual layers in the textured PZT stacks. The elastic moduli of the TiO_2 and Pt layers were 195±5 GPa and 167±2 GPa, respectively [65]. The mechanical response of the SiO_2-TiO_2-Pt composite stack was perfectly linear until failure at 0.85% strain, Figure 4.4(a), whereas, as shown in Figure 3.6(b) [65], the stress-strain response of a 100 nm Pt film was non-linear after 0.5% strain. The SiO_2-TiO_2-Pt-PZT composite films with 100% (111) PZT had the highest in-plane modulus of 112±2 GPa, whereas those stacks with 100% (001) PZT had the lowest in-plane modulus of 95±1 GPa. Five highly reproducible tests of specimens from each type were performed. The stress-strain response of all SiO_2-TiO_2-Pt-PZT composite films was non-linear, Figure 4.4(b), with the degree of non-linearity increasing with increased (001) texture. The non-linearity was not due to plastic deformation of the Pt layer since experiments on SiO_2-TiO_2-Pt multilayers showed perfect linearity. It was rather due to the mechanical behavior of textured PZT layers.

The elastic moduli of the textured PZT (52/48) layers were extracted from the initial segment of the loading curves of the SiO_2-TiO_2-Pt-PZT composite films in the linear regime and under a stress of 200 MPa. It was assumed that the total load was partitioned among the four layers under isostrain conditions leading to the following equation for the stress in the PZT layer, Figure 4.4(c), and hence the elastic modulus for textured PZT:

$$\sigma_{PZT} = \frac{1}{t_{PZT}}\left(\sigma_{stack}t_{stack} - \varepsilon_{stack}\left(E_{SiO_2}t_{SiO_2} + E_{TiO_2}t_{TiO_2} + E_{Pt}t_{Pt}\right)\right) \tag{4.5a}$$

$$E_{PZT} = \frac{1}{t_{PZT}}\left(E_{stack}t_{stack} - E_{SiO_2}t_{SiO_2} - E_{TiO_2}t_{TiO_2} - E_{Pt}t_{Pt}\right) \tag{4.5b}$$

where σ, ε, E and t are the stress, strain, Young's modulus and the thickness of the layers denoted by the subscripts, respectively.

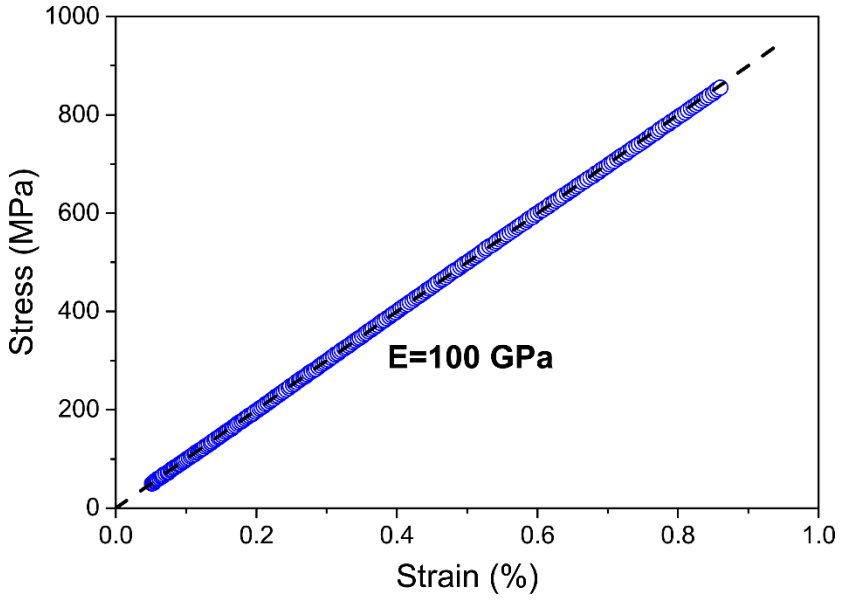

(a)

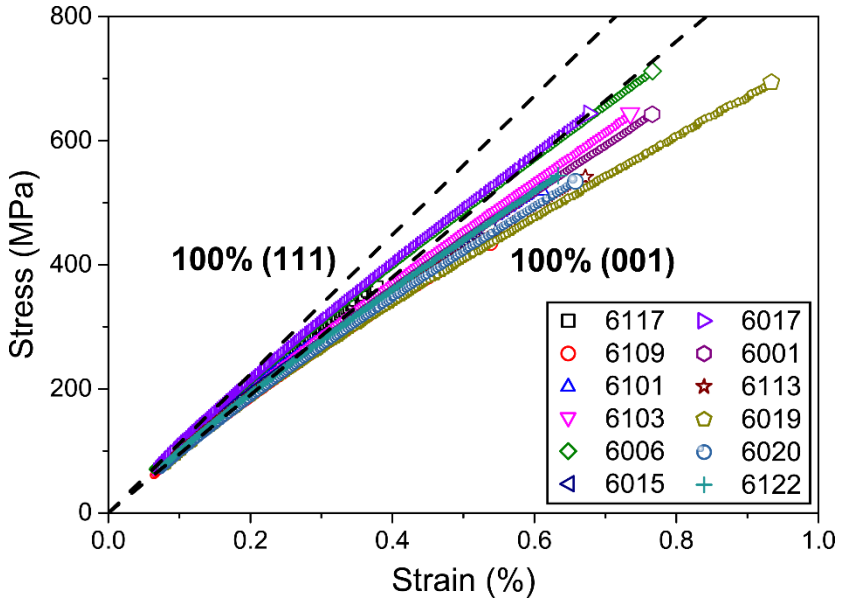

(b)

(figures continues on next page)

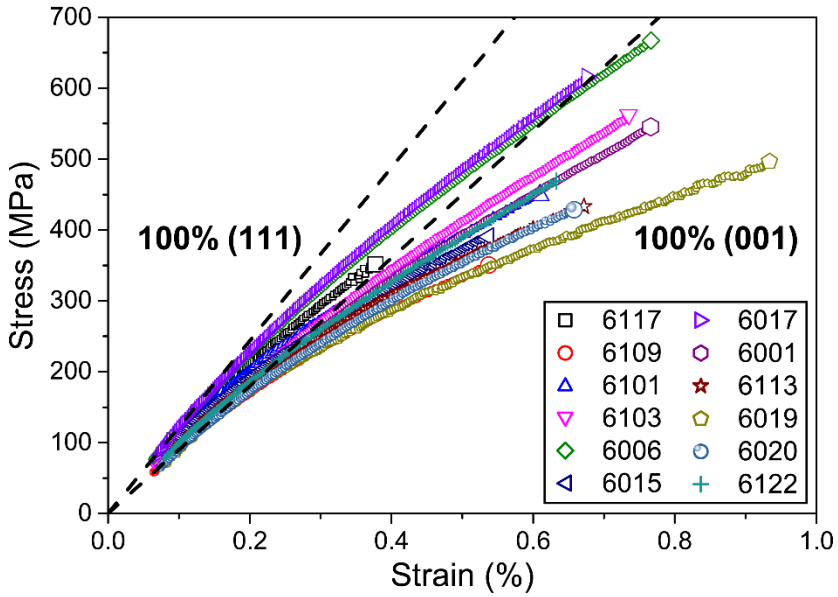

(c)

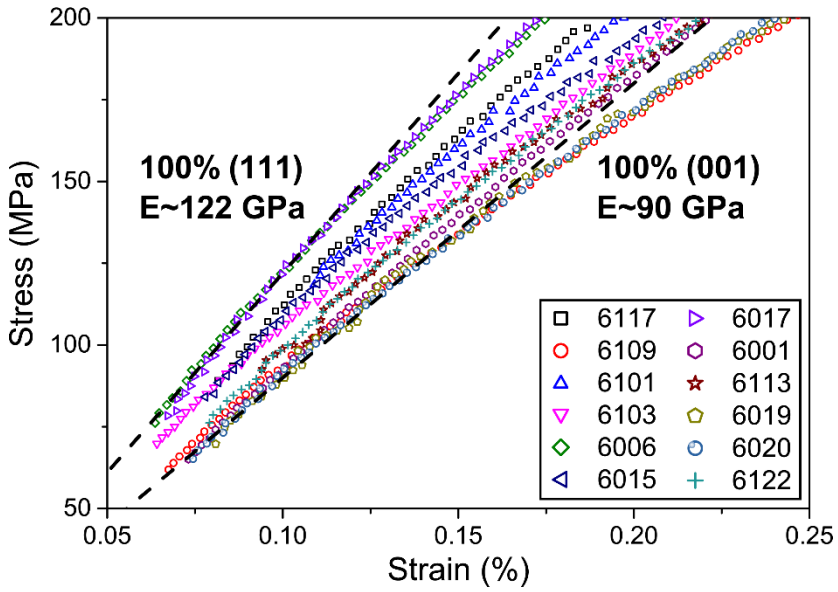

(d)

Figure 4.4. Stress-strain response of **(a)** SiO_2-TiO_2-Pt stack, **(b)** SiO_2-TiO_2-Pt-PZT stacks for various textures, **(c)** PZT, **(d)** PZT showing a magnified region of the plot (c). Table 4.2 provides the percentage texture for each run. The compositional and microstructural details of each Sample # are given in Table 4.2.

The isostrain assumption is valid as long as the different layers remain perfectly bonded throughout the entire loading process, even if one or more layers behave non-linearly [140,141]. Figure 4.4(d) shows a magnified portion of the PZT stress-strain curves illustrating the effect of texture on the elastic modulus of PZT. Open circuit tensile tests performed on SiO_2-TiO_2-Pt-PZT-Pt-ALD stacks reproduced the same effect of texture on modulus. By subtracting the contribution of the SiO_2-TiO_2-Pt-PZT stack from the stiffness of the entire SiO_2-TiO_2-Pt-PZT-Pt-ALD stack, the effective modulus of Pt-ALD layers was found to be 162 ± 21 GPa which resulted in 159 GPa for the elastic modulus of ALD, which is close to the value of 150-155 GPa reported for ALD deposited Al_2O_3 [142]. The open circuit modulus of PZT is plotted in Figure 4.5 as a function of the relative texture factors, demonstrating a linear relationship between the modulus and the relative percentage (001) and (111) texture factors: a pure (001) texture resulted in the minimum modulus value of 90±2 GPa, which increased linearly with (111) texture reaching the maximum value of 122±3 GPa for pure (111) texture.

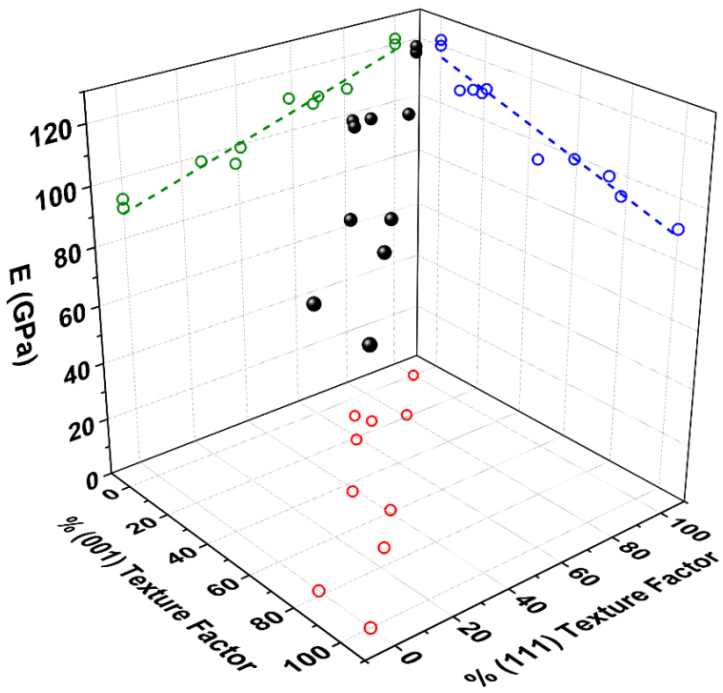

Figure 4.5. Elastic modulus of PZT as a function of %(001) and %(111) texture factors. The scatter in the data can be attributed to the presence of (110) texture which cannot be taken into account in the plot.

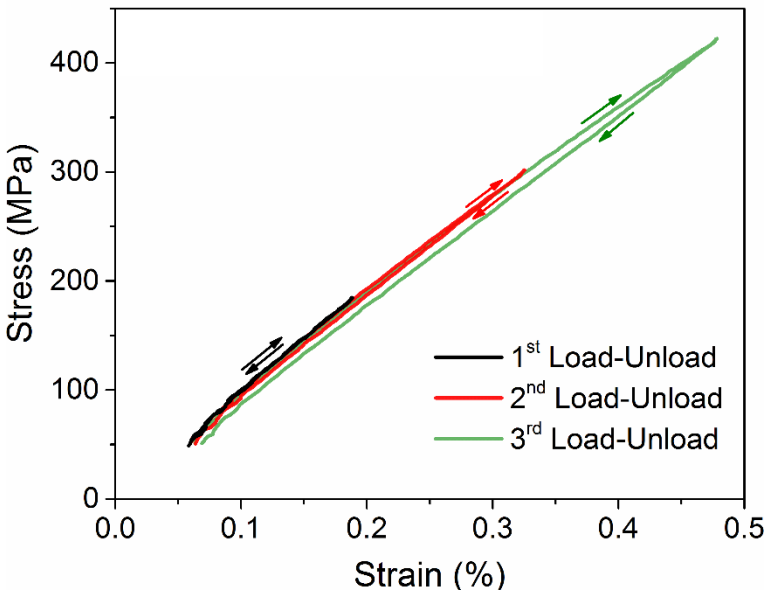

(a)

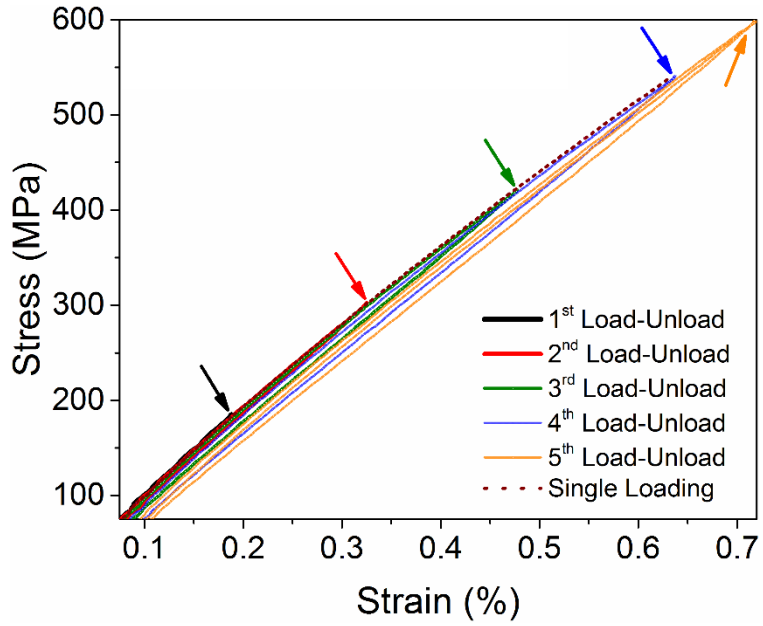

(b)

Figure 4.6. **(a)** Stress-strain loading-unloading curves of a specimen from (#6122) showing no hysteresis below 180 MPa and perfect overlap between loading and unloading curves. **(b)** Cyclic loading-unloading and single loading response demonstrating excellent matching between loading cycles. The arrows point to the maximum stress in each of five subsequent loading-unloading cycles.

Cyclic loading-unloading of the SiO_2-TiO_2-Pt-PZT stack films showed hysteresis in the stress-strain response. However, below 200 MPa, the loading and unloading curves showed no hysteresis, for example, Figure 4.6(a) for wafer #6122. Hence, all initial elastic moduli calculations were made on the SiO_2-TiO_2-Pt-PZT stacks below 200 MPa, since the stress-strain response of SiO_2-TiO_2-Pt-PZT stacks were much more linear and then the PZT modulus was extracted assuming isostrain deformation. Furthermore, the loading path remained identical in both cyclic loading-unloading and single loading curves, as shown, in Figure 4.6(b).

4.3 Micromechanics Model for Nonlinear Stress vs. Strain Response

Experimental stress-strain response, Figure 4.4(c), shows that (001) textured PZT exhibits the most non-linearity, compared to (111) textured PZT, which exhibits the least amount of non-linearity. Such nonlinearities are due to ferroelasticity, and a polycrystalline ferroelectric material at the morphotropic phase boundary (MPB) of any texture shows considerable nonlinear macroscopic strain due to non-180˚ domain switching [143]. The non-linearity in the tensile stress-strain response of thin film PZT [15] and bulk PZT [144,145] at the MPB has been attributed by other studies to ferroelastic 90˚ domain switching in the tetragonal phase due to stress. Ferroelastic domain switching in PZT ceramics at the MPB is complicated by concurrent in-phase domain switching (90˚ inside the tetragonal and 71˚ inside the rhombohedral phases) and interphase domain switching (tetragonal to rhombohedral phase transformation and vice-versa). To simplify the analysis of the observed non-linear response of the two extreme textures, only tetragonal symmetry was assumed, which is consistent with other studies [146,147]. Several studies have reported phenomenological [147,148] and micromechanical [149-152] models for domain switching in bulk ferroelectric materials. A simple micromechanics model based on Eshelby's inclusion problem [152,153] was adapted to compute the strain due to domain switching by accounting for tetragonal symmetry.

For (001) texture, tetragonal elongations parallel to (100), (010) and (001) in crystal coordinates lead to a_1, a_2, and c domains, respectively, and for (111) texture lead to d_1, d_2, and d_3 domains, respectively. In the case of pure (001) texture, the out-of-plane c domains can undergo either c-a_1 or c-a_2 switching depending on the crystal orientation with respect to the loading axis that lies in the plane of the film. The strain associated with $(c\text{-}a_1)$ or $(c\text{-}a_2)$ domain switching in local crystal coordinates is given by [151]:

$$\varepsilon^{(c-a_1)/(d_3^- - d_1^+)} = S_o \begin{bmatrix} 1 & 0 & 0 \\ 0 & 0 & 0 \\ 0 & 0 & -1 \end{bmatrix}, \quad \varepsilon^{(c-a_2)} = S_o \begin{bmatrix} 0 & 0 & 0 \\ 0 & 1 & 0 \\ 0 & 0 & -1 \end{bmatrix} \tag{4.6}$$

where $S_o = (c/a - 1)$ is the single crystal deformation. The films have fiber texture with in-plane isotropy and thus, the individual crystallites can take all possible in-plane orientations with respect to the loading axis. Consider n and m number of grains in which the crystal axes (100) and (010), respectively, are aligned along the loading axis and undergo $(c\text{-}a_1)$ and $(c\text{-}a_2)$ domain switching. These two particular orientations are equivalent and are chosen since domain switching along these orientations leads to the maximum strain in the direction of the applied stress and thus provide the maximum energy released to decrease the total energy of the system, thus making these domain switches thermodynamically favorable, as shown in inset (i) in Figure 4.7. Considering a spherical region as an isotropic Eshelby inclusion [152,153] which provides a good description for the boundary conditions of the PZT film in a PZT stack, the total change in system's free energy per unit volume due to domain switching is:

$$\Delta U = \Delta U_{Elastic} - \Delta U_M^{\infty} + f_{90} W_{90} \tag{4.7}$$

where $\Delta U_{Elastic}$, ΔU_M^{∞}, f_{90} and W_{90} denote the elastic mismatch energy, the work done by the far field applied stress, the fraction of 90˚ domain switched and the energy barrier for 90˚ domain switching. The elastic mismatch energy can be estimated via Eshelby's inclusion model, and Equation (4.7) can then be written as:

$$\Delta U = \frac{E_{(001)}(7-5\nu)}{15(1-\nu^2)}\left(\sum_{n=1}^{n} f_{3-1}^{n} + \sum_{m=1}^{m} f_{3-2}^{m}\right)^2 S_o^2 - \left(\sigma\left(\sum_{n=1}^{n} f_{3-1}^{n} + \sum_{m=1}^{m} f_{3-2}^{m}\right)S_o\right) + \left(\sum_{n=1}^{n} f_{3-1}^{n} + \sum_{m=1}^{m} f_{3-2}^{m}\right)W_{90_{(001)}} \quad (4.8)$$

where $E_{(001)}$, ν, f_{3-1}^{n}, f_{3-2}^{m}, and σ are the elastic modulus for (001) texture, the Poisson's ratio, the fraction of *(c-a₁)* domains that has switched in n^{th} grain, the fraction of *(c-a₂)* domain that has switched in m^{th} grain, and the applied in-plane stress, respectively.

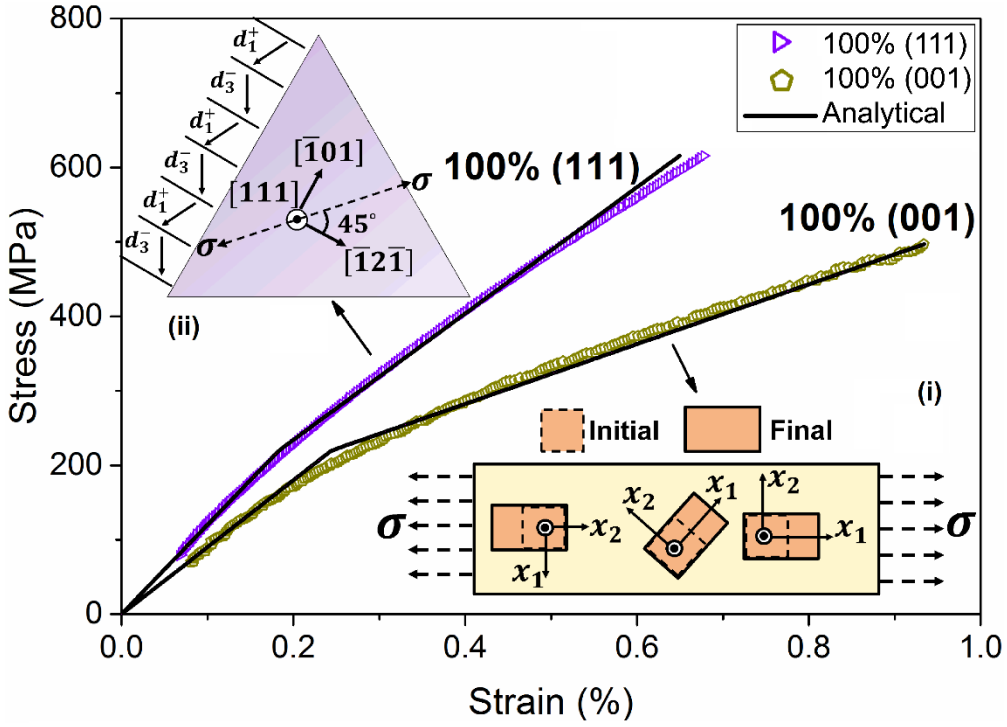

Figure 4.7. Comparison between analytical model and experimental results: **Inset (i)** shows the top view of a 100% (001) textured PZT film (#6019). The crystallites oriented along the stress direction undergo preferential domain switching (*c-a₁*) and (*c-a₂*) and give rise to non-linear stress-strain response; **Inset (ii)** shows the (111) plane of a 100% (111) textured film (#6017) and a uniaxial stress applied in [-(1+√3) 2 (-1+√3)] direction when d_3^- domains switch to d_1^+ domains and result in non-linearity.

The total strain in (001) texture due to domain switching is computed by minimization of energy of Equation (4.8):

$$\varepsilon_{DS_{(001)}} = \left(\sum_{n=1}^{n} f_{3-1}^{n} + \sum_{m=1}^{m} f_{3-2}^{m}\right) S_o = \frac{15(1-\nu^2)}{2E_{(001)}(7-5\nu)}\left(\sigma - \frac{W_{90_{(001)}}}{S_o}\right) \tag{4.9}$$

Notably, if the orientation of maximum strain due to domain switch coincides with the direction of applied stress, the total fraction of domain switching remains the same even if we consider the inclusion as a single grain undergoing only one type of switching.

In the case of pure (111) texture in the tetragonal phase, a combination of d_1, d_2 and d_3 domains taken two at a time, form normal twin domain boundaries. In order to maintain charge neutrality of the interface, the polarization of adjacent domains must alternate. For example, twin domain patterns, such as d_3^-/d_1^+, d_3^+/d_2^- and d_2^+/d_1^-, have been theoretically predicted as well as experimentally observed in tetragonal PZT [154,155]. When an in-plane stress is applied, 90˚ domain switching may occur when one of *d* domain switches to the other across a twin boundary. Such 90˚ domain switching in the tetragonal phase in (111) textured PZT films has been experimentally observed with applied electric field [155,156]. Considering (100), (010) and (001) as the coordinate axes, a 90˚ domain switch from a d_3^- to a d_1^+ domain generates the strain given by Equation (4.6). This strain must be resolved on the (111) plane and the maximum in-plane (ε'_{11}) component can be found by transformation of strain. For example, this strain tensor in the [-(1+√3) 2 (-1+√3)], [(1-√3) -2 (1+√3)], [111] coordinate system is:

$$\varepsilon'^{(d_3^- - d_1^+)} = S_o \begin{bmatrix} 0.5774 & 0 & -0.5774 \\ 0 & -0.5774 & -0.5774 \\ -0.5774 & -0.5774 & 0 \end{bmatrix} \tag{4.10}$$

As noted before, the analysis of 90˚ domain switching in a single grain with d_3^-/d_1^+ domains will provide the total volume fraction of domains subjected to 90˚

domain switching in the (111) texture. A uniaxial stress σ is applied along the [-(1+√3) 2 (-1+√3)] direction as shown in inset (ii) of Figure 4.7. Considering a spherical grain as an isotropic Eshelby inclusion, the total change in the system's free energy per unit volume due to $(d_3^- - d_1^+)$ domain switching in a single grain is given by:

$$\Delta U = \frac{E_{(111)}(7-5\nu)}{15(1-\nu^2)}\left(f_{90_{(111)}}S_o\right)^2 - 0.5774\left(\sigma f_{90_{(111)}}S_o\right) + f_{90_{(111)}}W_{90_{(111)}} \quad (4.11)$$

where $E_{(111)}$ is the elastic modulus for (111) texture.

The total strain due to domain switching for (111) texture can be calculated by minimization of energy of Equation (4.11):

$$\varepsilon_{DS_{(111)}} = \frac{15(1-\nu^2)}{2E_{(111)}(7-5\nu)}(0.5774^2)\left(\sigma - \frac{W_{90_{(111)}}}{0.5774S_o}\right) \quad (4.12)$$

Under uniaxial tension, the total strain at a particular stress is given by the sum of the elastic strain and the strain due to 90˚ domain switching as:

$$\varepsilon_{total_{(001)}} = \frac{\sigma}{E_{(001)}} + \frac{15(1-\nu^2)}{2E_{(001)}(7-5\nu)}\left(\sigma - \sigma_{th_{(001)}}\right) \quad (4.13a)$$

$$\varepsilon_{total_{(111)}} = \frac{\sigma}{E_{(111)}} + \frac{15(1-\nu^2)}{2E_{(111)}(7-5\nu)}(0.5774^2)\left(\sigma - \sigma_{th_{(111)}}\right) \quad (4.13b)$$

where $\sigma_{th_{(001)}} = W_{90_{(001)}}/S_o$ and $\sigma_{th_{(111)}} = W_{90_{(111)}}/(0.5774S_o)$ are fitting parameters. There is no strain due to domain switching below σ_{th}, which is the threshold stress for 90˚ domain switching. Figure 4.7 shows that Equations 4.13(a) and 4.13(b) can predict reasonably well the experimental stress-strain response with the same values for the fitting parameter $\sigma_{th_{(001)}} = \sigma_{th_{(111)}} = 220$ MPa and $\nu = 0.3$. The model shows that the fraction of 90˚ domain switched varies linearly with applied stress which agrees with the linear prediction for bulk PZT for switched fraction less than around 50% [148].

Finally, the model provides the total fraction of 90˚ domain switching as 10% and 17% for (111) and (001) textures, at their respective failure stresses, and suggests that the extrinsic property of ferroelastic domain switching depends on texture. Domain switching in the present PZT thin films is greatly suppressed potentially due to substrate clamping and pinning at interfaces, point defects and surfaces [157-159]. In contrast, bulk PZT ceramics have been modeled to reach ~100% 90˚ domain switching at the relatively low prestress value ~100 MPa [148].

4.4 Elastic Modulus as a Function of Texture

As was shown in Section 4.2, the open circuit modulus of PZT plotted in Figure 4.5, demonstrated a linear relationship with %(001) and %(111) texture factors: pure (001) texture resulted in the minimum modulus value of 90±2 GPa, which increased linearly with (111) texture reaching the maximum value of 122±3 GPa for pure (111) texture. The experimental moduli values are compared to theoretical predictions considering tetragonal symmetry and columnar grains. The elastic modulus of single crystal tetragonal (*P4mm*) systems along a <*hkl*> direction is given by

$$E_{\langle hkl\rangle\ tetragonal} = \frac{1}{(\alpha^4+\beta^4)s_{11}+\gamma^4 s_{33}+\alpha^2\beta^2(2s_{12}+s_{66})+\gamma^2(1-\gamma^2)(2s_{13}+s_{44})} \quad (4.14)$$

where α, β and γ are direction cosines and s_{ij} are the compliance coefficients. The compliance coefficients, s_{ij}^D for soft (s_{11}^D=15.08 TPa^{-1}, s_{12}^D=-9.25 TPa^{-1}, s_{13}^D=-3.03 TPa^{-1}, s_{33}^D=9.65 TPa^{-1}, s_{44}^D=26.46 TPa^{-1}, s_{66}^D=48.78 TPa^{-1}) and hard (s_{11}^D=9.52 TPa^{-1}, s_{12}^D=-4.48 TPa^{-1}, s_{13}^D=-1.99 TPa^{-1}, s_{33}^D=7.63 TPa^{-1}, s_{44}^D=16.05 TPa^{-1}, s_{66}^D=28.01 TPa^{-1}) bulk PZT ceramics under open circuit conditions were obtained from Ref. [9]. By invoking transverse isotropy, Equation (4.14) was averaged for an aggregate of columnar grains to obtain the effective in-plane modulus of (001) and (111) fiber textured PZT:

$$\overline{E}_{PZT(001)} = \frac{1}{2\pi}\int_{-\pi}^{\pi} \frac{d\theta}{\left(\left(\sin^4(\theta)+\cos^4(\theta)\right)s_{11}+\sin^2(\theta)\cos^2(\theta)\left(2s_{12}+s_{66}\right)\right)} \tag{4.15a}$$

$$\overline{E}_{PZT(111)} = \frac{1}{2\pi}\int_{-\pi}^{\pi} \frac{d\theta}{\left(\left(\alpha^4+\beta^4\right)s_{11}+\gamma^4 s_{33}+\alpha^2\beta^2\left(2s_{12}+s_{66}\right)+\gamma^2\left(1-\gamma^2\right)\left(2s_{13}+s_{44}\right)\right)} \tag{4.15b}$$

where $\alpha \approx (0.71\cos\theta - 0.41\sin\theta)$, $\beta \approx (-0.71\cos\theta - 0.41\sin\theta)$, and $\gamma \approx 0.81\sin\theta$ for a tetragonal unit cell with *c/a*=1.023 [160] at the morphotropic composition. Numerical evaluation of the integrals in Equations (4.15a) and (4.15b) yields in-plane elastic moduli of $\overline{E}_{PZT(001)}$ = 66 GPa and $\overline{E}_{PZT(111)}$ = 81 GPa for soft PZT, and $\overline{E}_{PZT(001)}$ = 105 GPa and $\overline{E}_{PZT(111)}$ = 126 GPa for hard PZT.

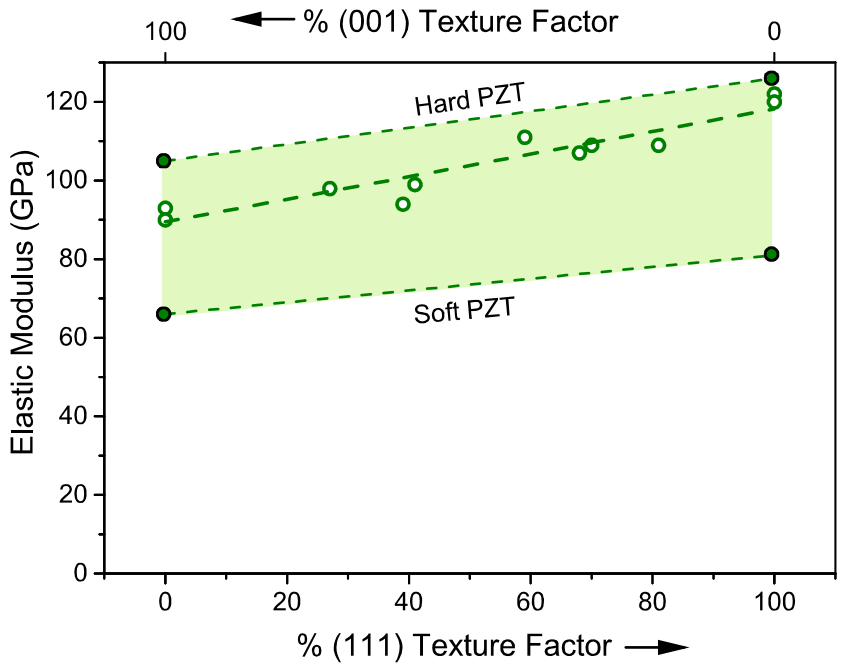

Figure 4.8. Elastic modulus as a function of %(111) texture factor: the experimental data lie within the upper and lower bounds calculated for transversely isotropic textured films by using the compliance coefficients for soft and bulk PZT and assuming the rule of mixtures. The dashed lines correspond to the theoretically calculated moduli based on the rule of mixtures and the computed $\overline{E}_{PZT(001)}$ and $\overline{E}_{PZT(111)}$.

Figure 4.8 shows the experimental Young's modulus of PZT as a function of percent (111) texture factor and the theoretical values for transversely isotropic textured films using the compliance coefficients for soft and hard bulk PZT. If the PZT is comprised of only (001) and (111) textures, then the rule of mixtures yields the lower and upper limits shown with dotted lines in Figure 4.8. The experimental data fit within these two bounds and lie close to the upper limit obtained for hard bulk PZT.

4.5 Conclusions

The effect of texture on the open-circuit mechanical response of 500-nm thick freestanding PZT films was investigated through uniaxial tension tests on SiO_2-TiO_2-Pt-PZT and SiO_2-TiO_2-Pt stacks. The stress-stress response of textured PZT films was extracted from the response of the SiO_2-TiO_2-Pt-PZT stacks by subtracting the contribution of the SiO_2-TiO_2-Pt stacks assuming isostrain deformation between all layers. The open circuit modulus computed from the initially linear segment of the stress-strain curves varied linearly with the %(001) and %(111) texture factors, specifically, between 90±2 GPa for pure (001) texture and 122±3 GPa for pure (111) texture. The stress-strain response was non-linear, with the 100% (001) textured films showing the most pronounced non-linearity, and the 100% (111) textured films having the least non-linear mechanical behavior. The strong non-linearity of (001) texture indicated easier 90˚ domain switching; a micromechanics model based on Eshelby's inclusion problem was developed to provide physical interpretation to the experimental results. This model fit well the experimental, non-linear, stress-strain curves for both the 100% (001) and 100% (111) textured PZT films, and at the point of failure predicted 17% and 10% of switched 90˚ domains in (001) and (111) textured PZT films, respectively, indicating that ferroelasticity, an extrinsic property of ferroelectrics, can be controlled via film texture.

CHAPTER 5

Control of Ferroelectric Response of PZT Films through Texture

Piezoelectric lead zirconate titanate (PZT) thin films have been used in several MEMS including inkjet printer heads [4], radio frequency (RF) MEMS switches [2], biosensors [5] and millimeter scale robotics [6]. Their performance can be improved by increasing the piezoelectric response of the PZT films at low applied voltages thus enabling large force, large displacement actuators and more sensitive sensors. It has been recognized that controlling the grain orientation in PZT films is critical in achieving desirable electromechanical properties [29] since perovskite ferroelectric materials are strongly anisotropic. Several studies [29-31,47,161] have reported on improved effective piezoelectric coefficients, $e_{31,f}$ and $d_{33,f}$ of {001} oriented polycrystalline PZT films at the MPB. As a result, there has been a recent impetus on orientation control, and thus piezoelectric and dielectric properties, of polycrystalline PZT films through modified fabrication techniques [33,44-46,51]. However, several other studies have reported an improved response for {111} [32], (110) [33] or even randomly oriented [34] PZT films near the MPB, which prevent the derivation of definite conclusions. These inconclusive results are further shrouded by the fact that the majority of prior studies have examined PZT films that were bonded to thick Si substrates without always accounting for residual stresses and their gradients, which could lead to a reduction in both linear and nonlinear ferroelectric behavior [35,36]. These reports provided the longitudinal piezoelectric strain coefficient, d_{33}, rather than the transverse coefficient, d_{31}, of PZT films. However, from a viewpoint of device design, d_{31} is more important than d_{33}, since large deflections can be induced in cantilever-type structures, compared to dimensional changes in the direction

of applied field. Computation of d_{31} requires the elastic modulus of the PZT film, which is quite difficult to obtain from thin films. Thus, studies have reported the effective piezoelectric stress coefficient, $e_{31,f,}$ which eliminates the need for the elastic modulus value.

This Chapter reports on studies on the transverse piezoelectric strain coefficient, $d_{31,f}$, of polycrystalline PZT films as a function of film texture, through out-of-plane deflection measurements in textured PZT microcantilever stacks in response to electrical bias. The elastic modulus values required in the calculation of d_{31} were obtained from uniaxial tension tests on freestanding textured PZT stacks from the same wafers [66]. PZT (52/48) films with 0-10% excess Pb were deposited on $PbTiO_3$ seed layers with 0-30% excess Pb. The excess Pb in the $PbTiO_3$ seed layer along with the texture of the underlying Pt film controlled the PZT texture. Although (111) and (100) PZT films were fabricated in the past to study their piezoelectric and ferroelectric properties [39,162], it has not been possible to control the texture and the relative fraction of grains with (111) and (100) orientation without major modification of the seeding layer [33,47]. Furthermore, in most prior studies, the PZT films were mechanically clamped to thick Si substrates, which made it difficult to measure out-of-plane deflections of cantilevers with dimensions comparable to typical MEMS devices.

5.1 Experimental Methods

5.1.1 Specimen Preparation and Materials Characterization

PZT films were fabricated using the chemical solution deposition or sol-gel method at the US Army Research Laboratory (ARL) as detailed in [133]. A highly {111} textured 100 nm Pt layer was deposited using magnetron sputtering onto 35 nm highly {100} textured TiO_2 grown on 300 nm SiO_2. Then, 20 nm $PbTiO_3$ seed layers containing 0-30% Pb-excess were prepared using the 2-Methoxyethanol (2-MOE) synthesis route. PZT (52/48) solutions with 10% Pb-excess were then spun cast and pyrolyzed on the $PbTiO_3$ seed layers according to the 2-MOE synthesis route, similar to the solution preparation method used by Budd *et al*. [134]. The total thickness of the pyrolyzed PZT

solutions was ~500 nm. Following PZT deposition, top electrodes of Pt were sputtered with a thickness of 50 nm, and patterned using Ar ion milling followed by a second Ar ion-milling process to pattern the PZT layer. Next, a combination of Ar ion milling followed by a wet etch was used to pattern the PZT layer and open access to the bottom Pt electrode. An evaporation of Ti/Pt/Au (20 nm / 20 nm / 730 nm) was added to the wafer as contact pads to the bottom and top Pt layers and patterned via metal lift-off. After the patterning processes, a reactive ion etch (RIE) using a fluorine plasma was performed on the elastic layer which enabled access to the Si substrate for the final release step. The entire wafer was placed into a XeF_2 etching chamber to etch the exposed Si isotropically, thus creating the freestanding multi-layered cantilever specimens. The cantilever specimens had a thickness of ~1 μm with varying lengths. The die with the specimens was diced out of the 150 mm wafer using a Mahoh dicing technique by Accretech America. Figure 5.1 shows the freestanding cantilever arrays with an initial curvature due to residual stress gradients.

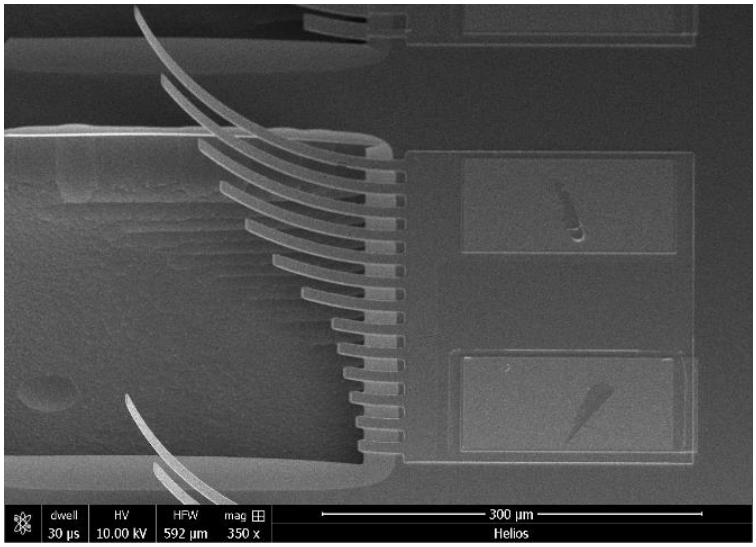

Figure 5.1. Side view of SiO_2-TiO_2-Pt-PZT-Pt cantilevers showing an initial curvature due to residual stress gradients.

5.1.2 Measurement of out-of-plane Displacement and Piezoelectric Properties

Oscillation of the piezoelectric cantilever arrays was induced by a triangular voltage wave applied to the top electrodes and by grounding the bottom electrodes, while the cantilever shape was measured in non-contact mode with a Polytec MSV laser Doppler vibrometer (LDV). The frequency of the triangular wave signal was 2 Hz, which was much lower than the mechanical resonance frequency of the cantilevers (>100 kHz). The out-of-plane displacement and velocity were obtained with a Michelson interferometer integrated into the LDV. The frequency difference and the phase difference provided the instantaneous velocity and displacement, respectively. The displacements along the length of the cantilevers were then used to calculate the transverse piezoelectric properties of the freestanding textured PZT films. Finally, *P-E* hysteresis loops were measured at 100 Hz as described in Section 2.3.1.

5.2 Results and Discussion

5.2.1 Unipolar Piezoelectric Actuation

The thickness, grain size, and texture of the PZT films were determined via SEM and XRD studies and are reported in Table 4.2. Figure 5.2(a) and Figure 5.2(b) show the tip displacements vs. time of 75 µm long cantilevers for 2 Hz periodic triangular voltage inputs of 0 - 10 V and 0 - (-10) V, after poling the films at +10 V and -10 V, respectively. The displacements are in-phase and out-of-phase with respect to the input signals when positive and negative voltages, respectively, are applied to the top electrode. Figure 5.2(c) shows asymmetric hysteresis of displacement vs. electric field during positive and negative unipolar sweeps. As shown in insets (i) and (ii) in Figure 5.2(c), the application of electric field along the polar (thickness) direction of the PZT caused a contraction of the PZT films along the in-plane dimensions due to transverse piezoelectric effect which resulted in a stress/strain gradient through the film thickness and upward cantilever deflection. Films with pure (001) texture showed the highest displacement contrary to pure (111) texture that resulted in the least cantilever tip displacement. In all samples, displacements larger than 1 µm were recorded in the 75 µm long cantilevers.

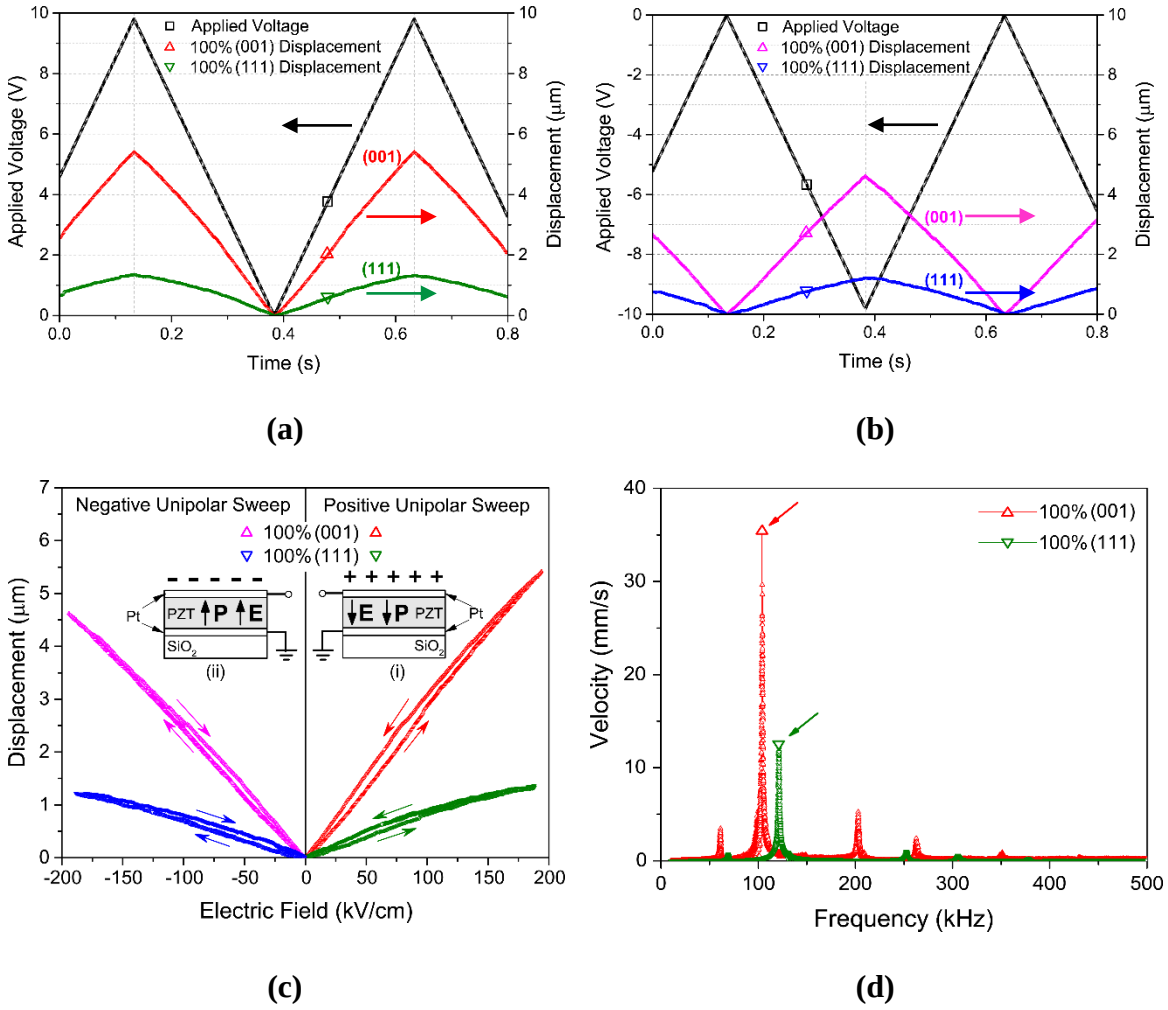

Figure 5.2. **(a)** Tip displacement of 75-μm long cantilevers as a function of time for two extreme textures when positive unipolar electric fields are applied. **(b)** Same as in (a) but for negative unipolar fields. **(c)** Displacements in (a) and (b) plotted as a function of applied unipolar electric field. Insets (i) and (ii) show that the electric field and polarization directions coincided during both positive and negative unipolar cycling leading to an expansion in the thickness direction and hence a contraction in the in-plane dimensions which resulted in the out-of-plane deflection of the cantilevers. **(d)** Velocity of cantilever tips as a function of frequency showing fundamental resonance frequencies in the 100 kHz range. Pure (111) texture had a higher resonant frequency than pure (001) texture due to higher modulus and slightly smaller cantilever length. Pure (001) texture is represented by Sample #6020 and pure (111) texture by Sample #6017.

5.2.2 High Field Effective Transverse Piezoelectric Coefficients

The two most common methods for the evaluation of the transverse piezoelectric coefficients of PZT thin films are based on the (a) measurement of the out-of-plane displacement of unimorph microscale PZT cantilevers in response to an applied electric field [33,47], and (b) measurement of the electric charge generated by deforming PZT films deposited on a Si wafer [29,90]. Unlike bulk PZT ceramics, thin PZT films are used in the form of multilayer stacks where the supporting layers and the electrodes impose significant constraints on the PZT film. Furthermore, because the thickness of the PZT layers is in the micrometer or sub-micrometer range, the electric field per unit thickness is quite high, which may place the film beyond the limits of linear piezoelectric behavior. Hence, most often the *effective piezoelectric coefficients* of a PZT film are computed instead of the *true piezoelectric coefficients*.

In this work, unipolar triangular voltage signals with a peak voltage of ±10 V were applied to the top electrode at a frequency of 2 Hz and the out-of-plane displacements measured with the LDV setup during unloading were used to determine the effective transverse piezoelectric coefficients. Static experiments are not very practical because charge leakage results in current losses due to finite resistance which would cause decay in cantilever deflection under static field conditions. On the other hand, the resonant frequencies of the cantilevers used to compute the piezoelectric coefficients were in the 100 kHz range as shown in Figure 5.2(d). Thus, the experiments can be considered as quasi-static, and the results approximate the static response. Thus, analytical static deflection models were used to describe the cantilever response. The out-of-plane deflection was modeled using the static deflection model by Weinberg [22] and the results were modified for a curved multilayer composite beam with an initial radius of curvature R_o, (which is allowed to be a function of position along the length of the cantilevers), which is much larger than the dimensions of the beam cross-section. The initial curvature was due to residual stresses at different interfaces in the stacks arising from deposition conditions. The relation between the radius of curvature, R (at the same location along a cantilever where R_o was measured) and the applied electric field, $\boldsymbol{E_{PZT}}$, is given by:

$$\frac{1}{R} = \frac{1}{R_o} - \frac{d_{31,f}(Z_{PZT}Y_{PZT}A_{PZT}\boldsymbol{E}_{PZT})}{\sum_i Y_i(I_i + A_i Z_i^2)} \tag{5.1}$$

where Z_i, Y_i, I_i, and A_i are the distance from the neutral axis, the Young's modulus, the moment of inertia, and the cross-sectional area of layer *i*, respectively.

The cantilever beams comprised of the SiO_2-TiO_2-Pt-PZT-Pt composite stack had a small segment near the fixed end resembling "webbed feet", Figure 5.3(a). A thin layer (~300 nm) of SiO_2 connected the individual cantilever beams in the array, requiring a more detailed analysis. To this effect, each beam was considered as the combination of two segments, as explained by the inset in Figure 5.3(a). It was assumed that a single initial radius of curvature, R_o, describes the entire beam profile and the curvature is the same in both segments 1 and 2. To justify this assumption, an example profile of the entire beam, as measured with a confocal microscope, is shown in Figure 5.3 (b), demonstrating that the curved beam perfectly conforms to a cylinder with constant radius R_o while the curve fits well the profile, $w \approx (\theta)x + (1/(2R_o))x^2$ [163] with θ being the initial take-off angle. Note that the parabolic profile has approximately the same constant radius of curvature, R_o since the initial take-off angle is very small.

The widths and thicknesses of the two segments of the cantilevers in Figure 5.3(a), as measured from SEM micrographs, and the elastic moduli of the various layers measured via uniaxial tension tests of freestanding film stacks from the same wafers [65,66] are provided in Table 5.1. The open circuit modulus of PZT was used instead of the short circuit modulus to calculate the transverse piezoelectric coefficient $d_{31,f}$. The open circuit modulus does not differ significantly from the short circuit modulus in PZT due to the small piezoelectric coupling coefficient (k^2~0.12 [22]), and it can be shown that $d_{31,f}$ increases by only 4% when the elastic modulus decreases by 20%. Note that the open circuit modulus of PZT decreases with %(001) texture factor, which is also predicted by a theoretical analysis assuming columnar grains and tetragonal symmetry [66].

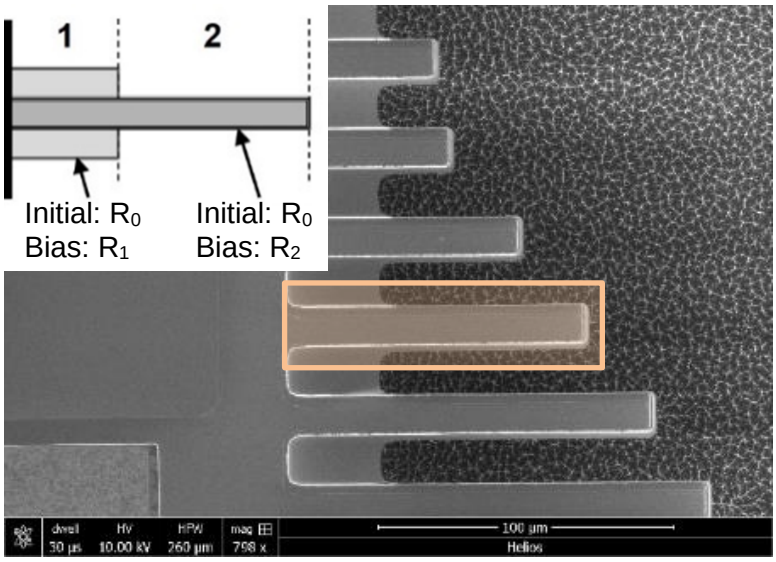

(a)

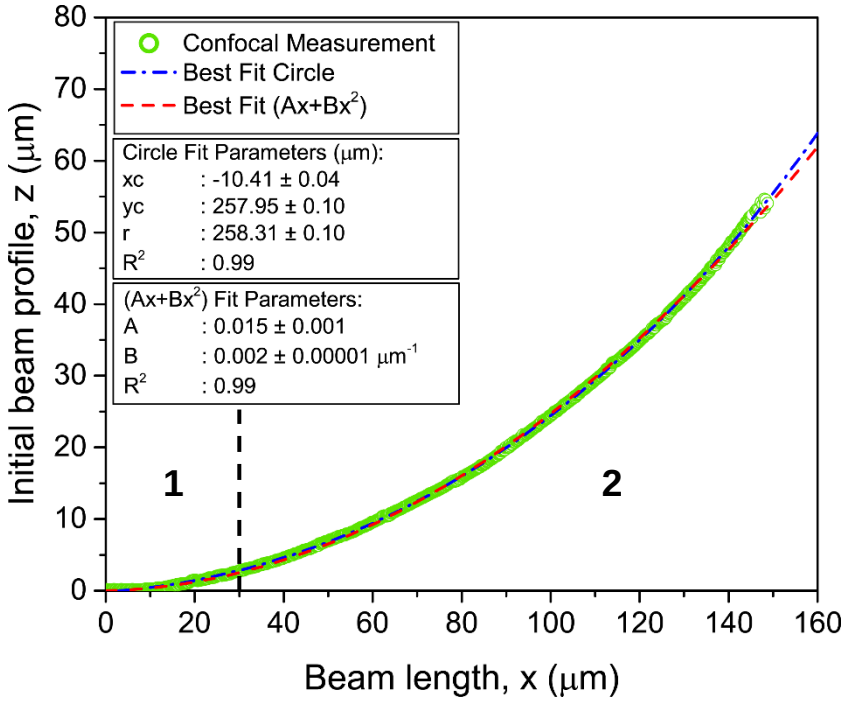

(b)

(figure continues on next page)

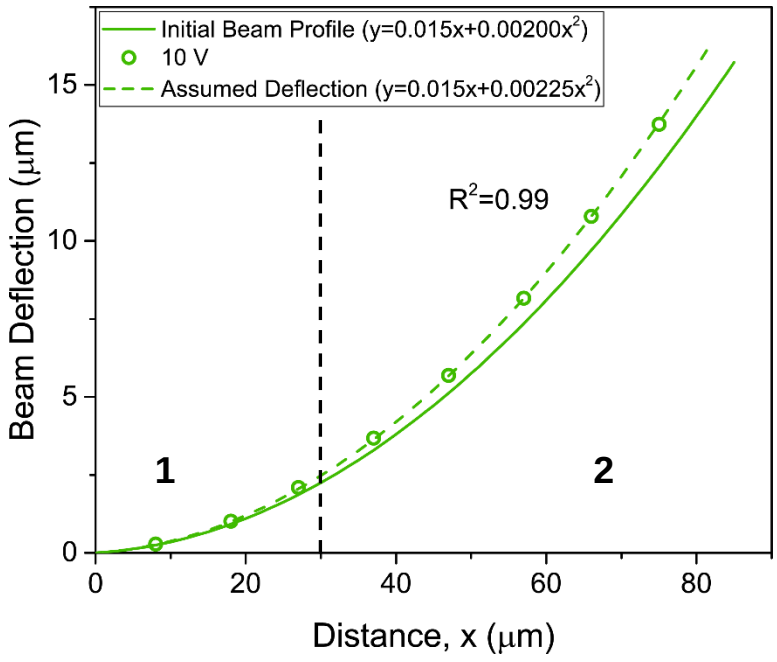

(c)

Figure 5.3 (a) Scanning electron micrograph of a PZT composite cantilever beam array. The box outlines the segment of each cantilever beam that was analyzed according to the schematic in the inset, comprised of two segments, with segment 1 having an additional SiO_2 layer. **(b)** Beam profile measured with a confocal microscope, showing a constant curvature in segments 1 and 2. The blue line is the best fit circle whereas green line is the best fit parabola. **(c)** Beam profile at 10V bias. The open circles are the experimentally determined displacements along the beam length using the LDV setup.

Table 5.1. Properties and dimensions of layers in the SiO_2-TiO_2-Pt-PZT-Pt stacks.

	SiO_2	**TiO_2**	**Bottom Pt**	**PZT**	**Top Pt**
E (GPa)	68	195	167	Chapter 4	167
Width (μm), segment 1	31.5	13.5	13.5	13.5	10
Width (μm), segment 2	15	13.5	13.5	13.5	10
Thickness (nm)	300	35	100	Table 4.2	50

Equation (5.1) was used to relate the radius of curvature of segment 1, R_1 and segment 2, R_2 with the applied electric field assuming that a single curvature described both segments. When an electric field was applied to any of the films listed in Table 4.2, it was established that:

$$0.98 \leq \frac{\left(\frac{1}{R_2} - \frac{1}{R_0}\right)}{\left(\frac{1}{R_1} - \frac{1}{R_0}\right)} \leq 0.99 \tag{5.2}$$

The relationship in Equation (5.2) shows that the radius of curvature induced by the applied electric field was roughly the same in each of the two beam segments. Therefore, it was assumed that the entire beam profile is described well by a single radius of curvature as shown in Figure 5.3(c). To convert the radius of curvature to out-of-plane displacements, which are measured via the LDV, two additional assumptions are made for the fixed boundary:

$$w(0, \boldsymbol{E}) \approx 0 \tag{5.3}$$

$$\left.\frac{\mathrm{d}w}{\mathrm{d}x}\right|_{(0,\mathbf{E})} = \left.\frac{\mathrm{d}w}{\mathrm{d}x}\right|_{(0,0)} \tag{5.4}$$

namely, there is no out-of-plane deflection at the fixed end, and the initial take-off angles of the cantilevers at the fixed end do not change with the application of the electric field. The validity of these assumptions is verified in Figure 5.3(c) where the deflected beam profile, represented by the dotted curve, satisfies Equations (5.3) and (5.4). Utilizing these two assumptions, the electric field-induced out-of-plane displacement $(\delta\text{-}\delta_o)$ at a location x from the cantilever fixed end (considering either a circular or a parabolic profile), can be related to the applied electric field $\boldsymbol{E}$ as:

$$(\delta - \delta_o) \approx \frac{x^2}{2}\left(-\frac{d_{31,\mathrm{f}}(z_{PZT}Y_{PZT}A_{PZT}\boldsymbol{E}_{PZT})}{\sum_i Y_i(I_i + A_i z_i^2)}\right) \tag{5.5}$$

Using Equation (5.5), the slope of the displacement vs. electric field and the effective transverse piezoelectric coefficients can be given by the following:

$$\frac{\partial(\delta-\delta_o)}{\partial \boldsymbol{E}_{PZT}} = \frac{x^2}{2}\left(-\frac{d_{31,\mathrm{f}}(z_{PZT}Y_{PZT}A_{PZT})}{\sum_i Y_i(I_i + A_i z_i^2)}\right) \tag{5.6a}$$

$$d_{31,f} = -\frac{2}{x^2}\left(\frac{\partial(\delta-\delta_o)}{\partial \boldsymbol{E}_{PZT}}\right)\left(\frac{\sum_i Y_i(I_i + A_i z_i^2)}{z_{PZT}Y_{PZT}A_{PZT}}\right) \tag{5.6b}$$

Equation (5.5) shows that the out-of-plane displacement is proportional to the applied electric field $\boldsymbol{E}$ and the square of the distance from the fixed end. To apply the model to the textured PZT films, the unloading slope of the linear part of the displacement versus electric field was computed, Figure 5.4(a), along each cantilever, similar to the slope calculation of strain vs. electric field in [164]. As shown in Figure 5.4(b), the experimental slope demonstrated a parabolic dependence on the distance from the fixed end which is in agreement with Equation (5.6a). Using Equation (5.6b), $d_{31,f}$ was computed at 5 points along each cantilever, and the results for different textures are given in Table 5.2. Figure 5.5(a,b) show $d_{31,f}$ as a function of %(001) and %(111) texture factors. The transverse piezoelectric coefficient, $d_{31,f}$, exhibits its largest value of 96 ± 3 pm/V for pure (001) texture, and decreases linearly with (111) texture reaching its smallest value of 40 ± 5 pm/V for pure (111) texture. Kanno *et al*. also reported a value of 100 pm/V for c-axis oriented (001) PZT [11]. The advantageous piezoelectric and ferroelectric properties of pure (001) vs. pure (111) texture have been reported by previous experimental and theoretical studies too [29,30]. The advantage of the results presented in Table 5.2, is that the calculation of $d_{31,f}$ is based on direct measurements of the elastic properties of the same PZT films, instead of assuming bulk values, therefore not only the trends but also the exact values are of high accuracy.

Most prior studies have reported the effective piezoelectric stress coefficient, $e_{31,f}$ instead of the piezoelectric strain coefficient, $d_{31,f}$. For comparison, the strain coefficients were converted to the stress coefficients, assuming that the $d_{31,f}$ values are very close to

the material coefficients, d_{31}. This assumption is justified since all measurements were made on freestanding stacks. When the textured PZT layers with transverse coefficients, d_{31} are clamped to thick substrates preventing in-plane extensions or contractions of the PZT layers, only the out-of-plane strains and the in-plane stresses need to be accounted for. The following equation relates d_{31} to $e_{31,f}$:

$$e_{31,f} = \frac{d_{31}}{s_{11}^E + s_{12}^E} \approx \frac{d_{31,\mathrm{f}}}{s_{11}^E + s_{12}^E} \tag{5.7}$$

where s_{ij}^E are the compliance coefficients at constant electric field, i.e. under short circuit conditions. The short circuit compliance coefficients are again assumed not to differ much from the open circuit values. Transverse isotropy provides: $s_{11}^E = 1/Y_{PZT}$ and $s_{12}^E = -\nu_{PZT}/Y_{PZT}$, where Y_{PZT} and ν_{PZT} are the Young's modulus and the Poisson's ratio (assumed 0.3 without orientation dependence) of textured PZT under open circuit conditions.

With the aid of Equation (5.7), the values of $e_{31,f}$ were calculated from the strain coefficients, $d_{31,f}$, and are plotted in Figure 5.5(c). In general, $e_{31,f}$ increased with %(001) texture factor, while no particular trend can be established in the way $e_{31,f}$ varied with %(110) texture factor, as shown in Figure 5.5(d). This independence of $e_{31,f}$ from %(110) texture factor is important as some (110) texture is always present except for 100% (001) or (111) texture. The $e_{31,f}$ values reported in this study follow closely those reported by Ledermann *et al*. [29] and other studies [33,161,165] for the two extreme textures. Notably, the $e_{31,f}$ values obtained for the high maximum electric field, E_{max} ~200 kV/cm, agreed well with those computed by Ambika *et al*. [33] also for 200 kV/cm. It should be emphasized that this dissertation research provide intermediate $e_{31,f}$ values for various percentages of (001) texture as opposed to previous literature that quantified only the extreme cases of 100% (111) and 100% (001) texture.

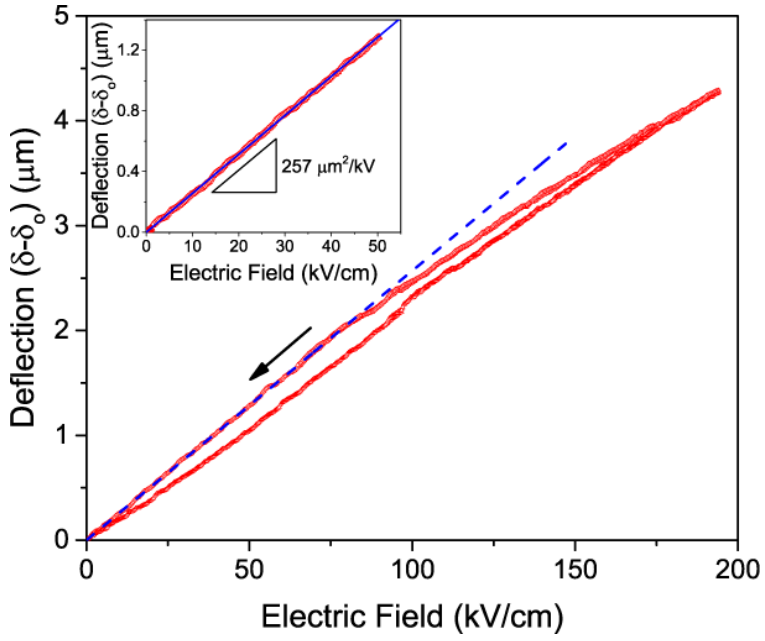

(a)

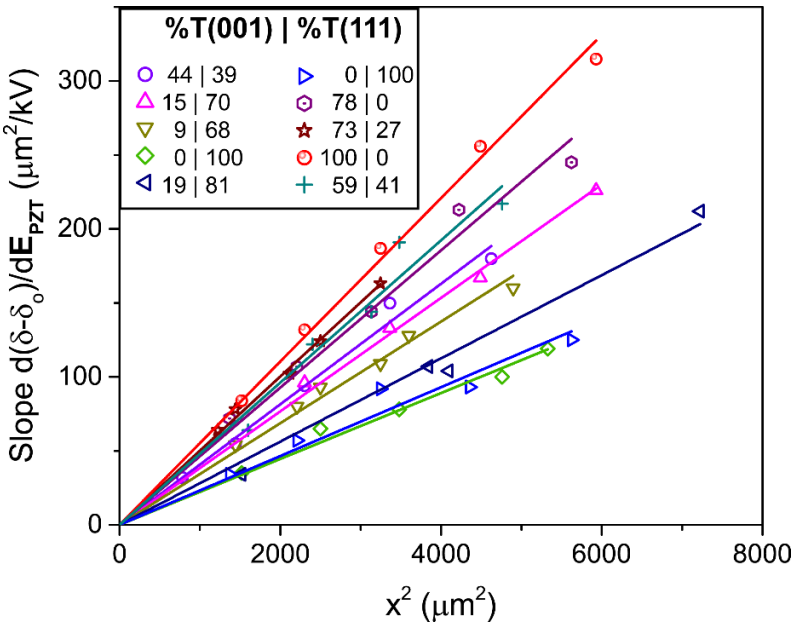

(b)

Figure 5.4 (a) Out-of-plane displacement as a function of electric field for a point on Sample #6020 with 100% (001) texture, which was 67 μm away from the fixed end. **(b)** Slope as a function of the square of the distance from the fixed end for different percentages of (001) and (111) texture factors. All curves are bracketed between 0|100 and 100|0 ratio of %T(001) | %T(111).

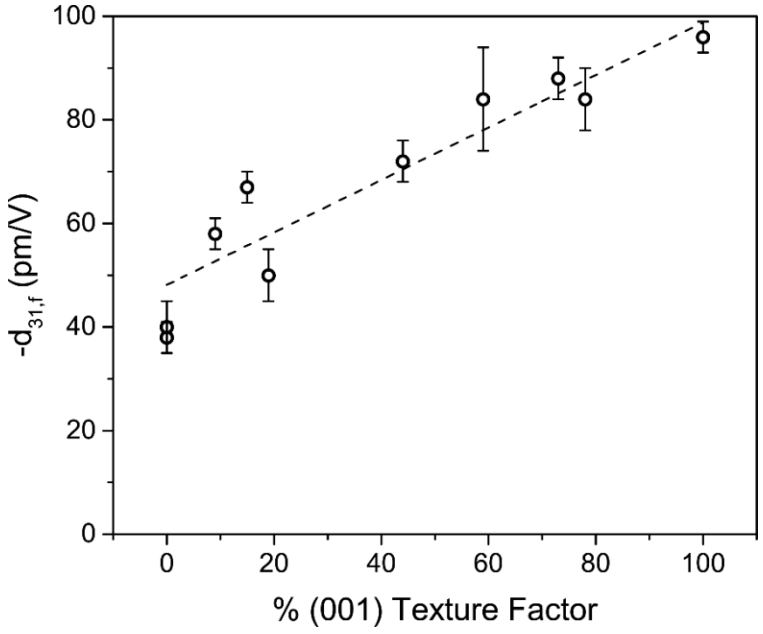

(a)

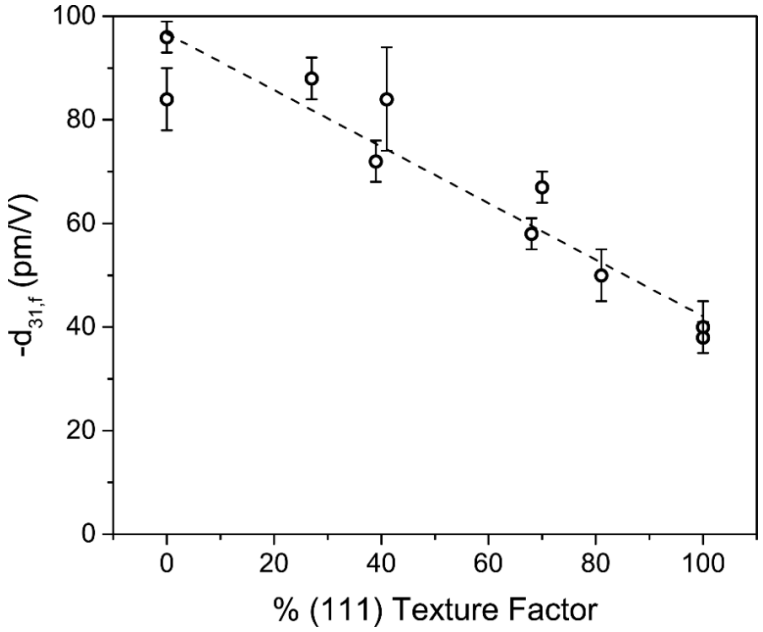

(b)

(figure continues on next page)

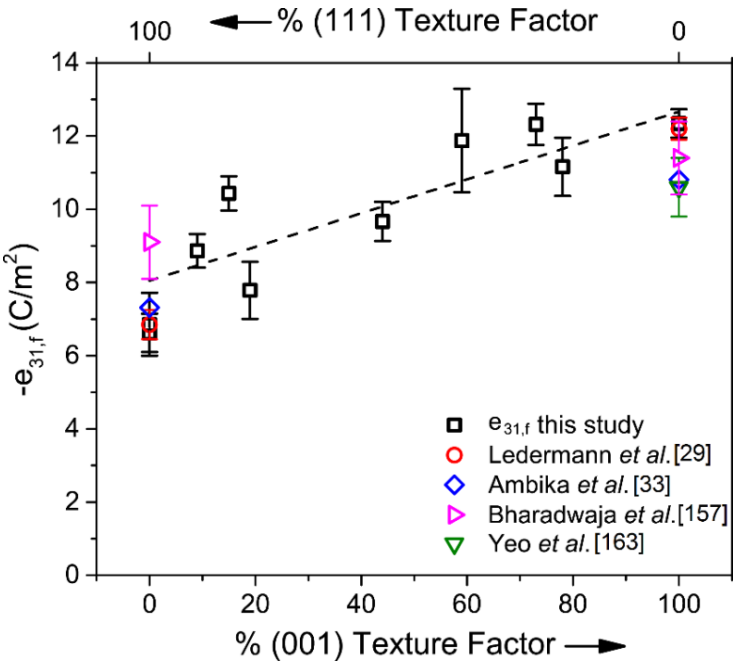

(c)

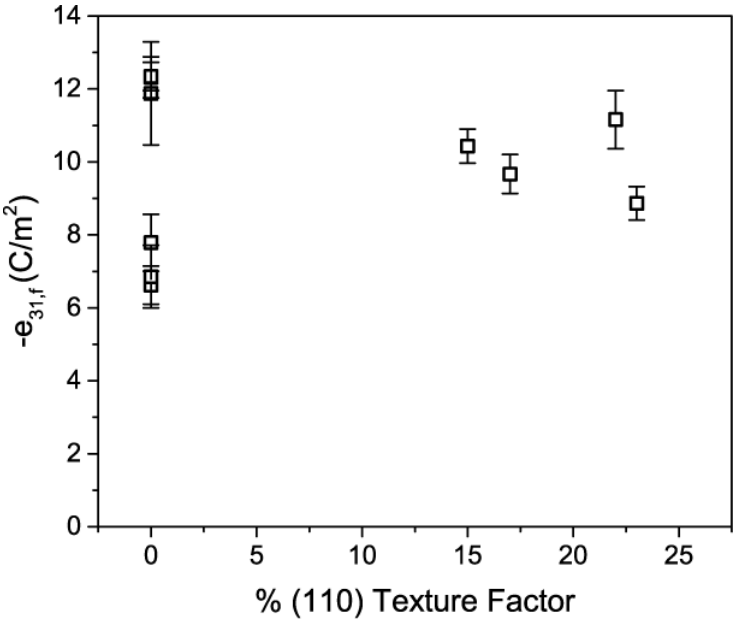

(d)

Figure 5.5 (a) Transverse strain coefficient, $d_{31,f}$, as a function of %(001) and **(b)** %(111) texture factors. Effective piezoelectric stress coefficients, $e_{31,f}$, calculated from strain coefficients, $d_{31,f}$, as a function of %(001) texture factor. **(c)** Effective piezoelectric stress coefficients, $e_{31,f}$, as a function of %(110) texture factor.

Table 5.2. Effective piezoelectric coefficients, $d_{31,f}$ and $e_{31,f}$ of textured PZT layers.

Sample #	% T_{001}	% T_{110}	% T_{111}	$d_{31,f}$ (pm/V)	$e_{31,f}$ (C/m^2)
6109	44	17	39	72 ± 4	9.7 ± 0.5
6101	15	15	70	67 ± 3	10.4 ± 0.5
6103	9	23	68	58 ± 3	8.9 ± 0.5
6006	0	0	100	38 ± 3	6.6 ± 0.5
6015	19	0	81	50 ± 5	7.8 ± 0.8
6017	0	0	100	40 ± 5	6.9 ± 0.9
6001	78	22	0	84 ± 6	11.2 ± 0.8
6113	73	0	27	88 ± 4	12.3 ± 0.6
6020	100	0	0	96 ± 3	12.3 ± 0.4
6122	59	0	41	84 ± 10	11.9 ± 1.4

The results presented in the previous paragraphs were based on experimental measurements at high electric field (~200 kV/cm) which is beyond the linear piezoelectric effect. Beyond the coercive electric field, $\boldsymbol{E_c}$, there are nonlinear contributions, such as domain switching, domain wall vibration and translation, etc. However, these nonlinear contributions die out as the saturation electric field is approached [166]. In bulk PZT, the longitudinal piezoelectric coefficient, d_{33}, has been shown to increase linearly with remanent polarization until saturation polarization is reached, beyond which the longitudinal piezoelectric coefficient remains constant [166]. A similar variation in e_{31} (derived from d_{31}) with electric field has been reported for PZT thin films [33]. All films tested in this work reached their saturation polarization at 10 V (~200 kV/cm), as shown for example in Figure 5.6 in which a plot of the positive remanent polarization, P^R against the applied electric field for Sample #6103, with 9% and 68% of (001) and (111) texture, respectively, shows saturation beyond maximum

electric field of 180 kV/cm. As a result, the effective transverse piezoelectric coefficient, $d_{31,f}$ reported in Table 5.2 provide the highest value of the coefficient for the ferroelectric material.

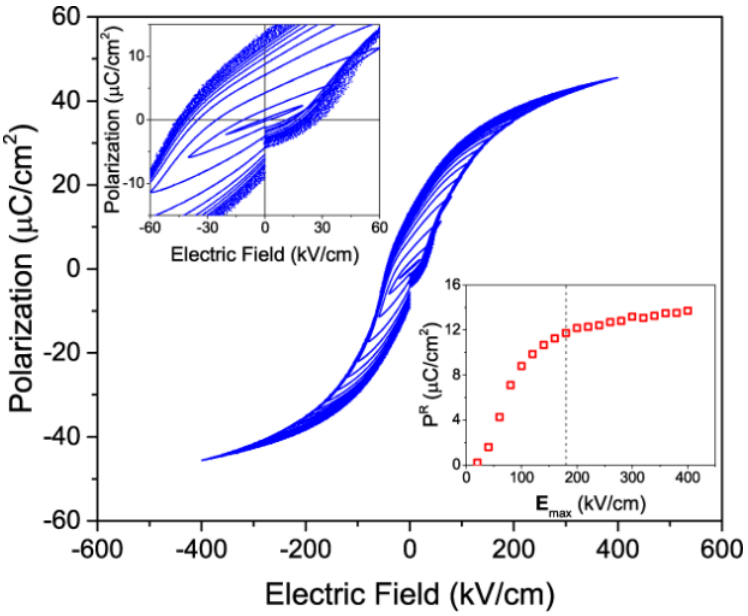

Figure 5.6 *P-E* hysteresis loops for Sample #6103 with 9% (001) and 68% (111) texture, cycled in the range 1 - 20V at 100 Hz. The inset shows saturation in remnant polarization at ~180 kV/cm.

5.2.3 Low Field Effective Transverse Piezoelectric Coefficients

The dependence of the effective piezoelectric coefficients on the applied electric field and the saturation in the transverse coefficients, were investigated via unipolar bias experiments in which the electric field was cycled at 2 Hz from zero to a progressively higher maximum value. Figure 5.7(a) shows the displacement vs. electric field loops for the tip of a cantilever, which is 115 μm away from the fixed end, from Sample #6020 with 100% (001) texture, as the maximum electric field is progressively increased from 20 to 198 kV/cm. The magnified region and the inset in Figure 5.7(b) shows that the

unloading slopes of the linear segment of the hysteresis curves reach a saturation beyond ~150 kV/cm. Using Equation (5.6b), it can be shown that, for all samples except #6113 (comprised of 73% (001) and 27% (111) texture), the transverse piezoelectric strain coefficient, $d_{31,f}$ also reaches saturation beyond ~150 kV/cm. Figure 5.7(c) shows the variation of $d_{31,f}$ with the maximum applied electric field. The two extreme textures: 100% (001) and 100% (111) bracketed the $d_{31,f}$ values of all but one other texture, all demonstrating high-field saturation in piezoelectric coefficients. On the other hand, Sample #6113 with 73% (001) and 27% (111) texture had stably high $d_{31,f}$ at all values of electric fields, including well-below the coercive field, where the intrinsic contribution from ionic deformation of the unit cell is dominant. Thus, for Sample #6113, there was, potentially, very limited contribution of non-linear processes, such as domain switching, domain wall vibration, and translation, etc. to the piezoelectric response since these non-linear processes become active only at high electric fields beyond the coercive field. A similar stability of piezoelectric properties with electric field has been shown by Kanno *et. al*. [47], albeit for films with 100% (001) texture, deposited on a particular substrate.

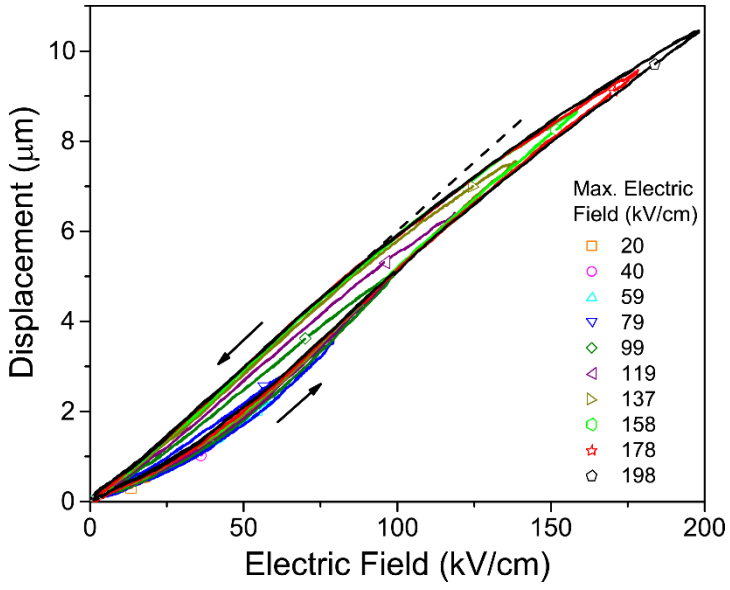

(a)

(figure continues on next page)

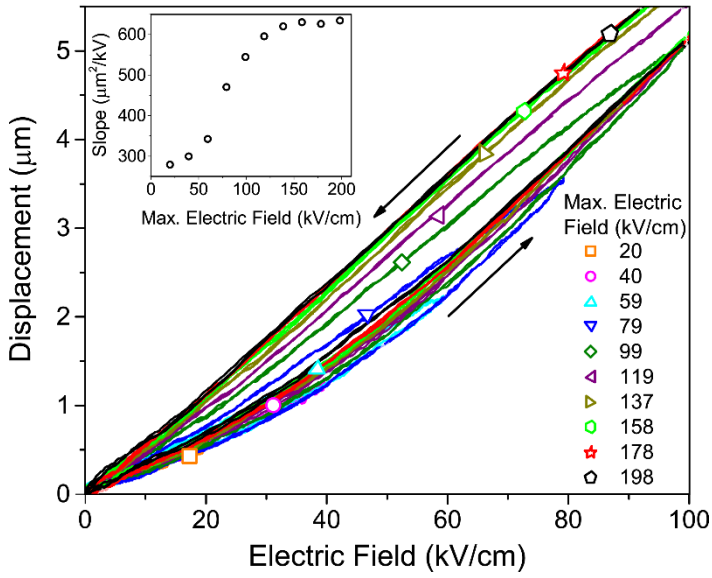

(b)

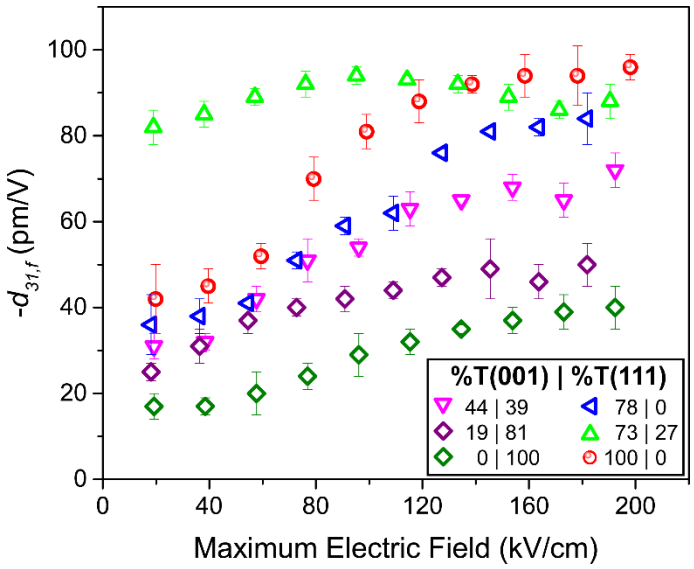

(c)

Figure 5.7 (a) Tip displacement vs. electric field loops for Sample #6020 with 100% (001) texture, as the maximum electric field is cycled to a progressively higher value. **(b)** Magnified view of (a) for the lower end of electric field values. **(c)** $d_{31,f}$ vs. maximum applied electric field showing saturation at ~150 kV/cm for samples with textures: 100% (001) (#6020), 78% (001) and 0% (111) (#6001), 44% (001) and 39% (111) (#6109), 19% (001) and 81% (111) (#6015), and 100% (111) (#6017). Only Sample #6113 with 73% (001) and 27% (111) texture demonstrated relatively stable $d_{31,f}$.

In Figure 5.5 was shown that the effective piezoelectric coefficients at saturation vary linearly with % (001) and (111) texture factors. It remains to show whether a similar linearity would hold for the linear piezoelectric effect, except for Sample #6113 (with 73% (001) and 27% (111) texture) which was shown in Figure 5.7(c) to have a stable piezoelectric response. The linear piezoelectric effect is valid when the applied electric field is well below the coercive electric field. Figure 5.8 shows the linear piezoelectric behavior for the two extreme textures: 100% (001) and 100% (111). The out-of-plane displacement of a cantilever tip that is 140 µm away from its fixed end varies linearly with the electric field when the maximum bipolar electric field is limited to ~20 kV/cm which is below the coercive electric field for all samples. The figure also shows that the displacements at such low electric fields depend on film texture: the (001) texture resulted in the largest displacement and slope, while (111) texture resulted in the smallest values.

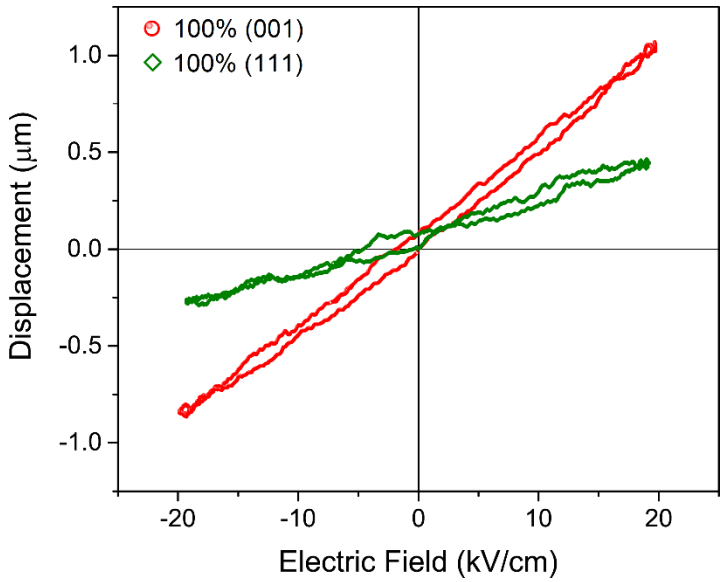

Figure 5.8 Out-of-plane tip displacement at 140 µm away from the fixed end showing linear variation with electric field at low fields. 100% (001) texture is represented by Sample #6020 and 100% (111) texture by Sample #6017.

Using Equation (5.6b), the constant slope of unipolar displacement vs. electric field is, again, converted to the effective linear piezoelectric coefficient. Finally, Figure 5.9 shows the linear and saturated effective piezoelectric strain coefficients, $d_{31,f}$ vs. (001) and (111) texture factors, which increased linearly with (001) texture content. The linear transverse piezoelectric properties increased from -17±3 pm/V for pure (111) texture to -42±8 pm/V for the pure (111) texture.

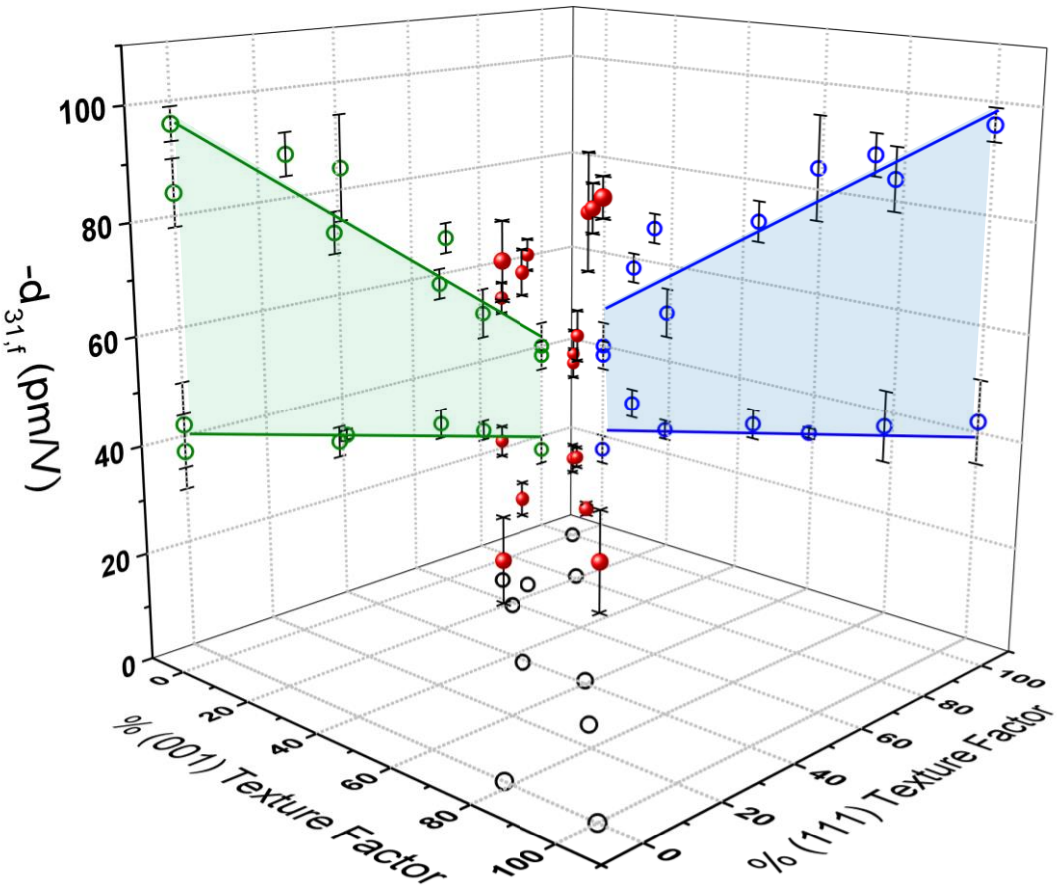

Figure 5.9 Linear and saturated effective transverse strain coefficient, $d_{31,f}$, vs. %(001) and %(111) texture factors. The points in green and blue are the projection of the points in red onto the vertical panels of the plot.

5.2.4 P-E Hysteresis Loops and Bipolar Piezoelectric Actuation

The *P-E* hysteresis loops, Figure 5.10(a), exhibited tilting, shifting, and pinching in varying degrees. Tilt in hysteresis loops demonstrates the presence of a low-dielectric constant layer between the PZT layer and the electrodes. This results in separation of bound charges due to PZT polarization from the compensating charges on the Pt electrodes and a depolarizing field across the PZT layer [167]. Similarly, pinching and shifting may occur due to electronic defect dipoles between oxygen or lead vacancies and substitute impurity ions with a lower or a higher valence than the host atom [167]. Positive or negative shift of hysteresis loops along the field axis indicates an internal bias or field originating from the preferential orientation of electric defect dipoles along the polarization direction. Pinched loops can form due to several reasons. For instance, constricted or pinched loops are observed when both positive and negative internal bias with respect to the applied field is present in different domains of a ferroelectric material. Also, pinched loops can form due to diffusion of defects into domain walls giving rise to domain pinning and internal fields [167]. In this work, the hysteresis loops for predominantly (001) textures and higher Pb-excess in the $PbTiO_3$ solutions were pinched and tilted. Furthermore, the values of maximum polarization, saturation polarization, and remnant polarization decreased with increasing excess Pb in the $PbTiO_3$ layer.

Figure 5.10(a) shows that the *P-E* hysteresis loop of Sample #6006 with 100% (001) texture showed tilting, pinching and shifting. Tilting and pinching could be the reason for the lower values of saturation and remnant polarization for (001) texture as compared to (111) texture. Previous studies have reported higher saturation and remnant polarization for the (001) texture [47,162] and Ref. [47] showed square hysteresis loop for the (001) texture which is expected since c-axis oriented domains should exhibit abrupt polarization reversals. The *P-E* hysteresis loops have a direct bearing on the displacement butterfly curves shown in Figure 5.10(b) which were also measured by applying triangular wave signals with a bipolar voltage amplitude of ±10 V at 2 Hz. All samples showed clear polarization reversals at their respective coercive electric fields, E_c. Sample #6020 with pure (001) texture demonstrated the largest peak displacement, and

Sample #6006 with pure (111) texture demonstrated the smallest peak displacement at high fields.

It may be noted that Sample #6020 with pure (001) texture hardly showed any negative displacement compared to all other samples. This is due to its pinched P-E hysteresis loop where the gap between the coercive fields, $-\boldsymbol{E_c}$ to $+\boldsymbol{E_c}$ is so small that polarization reversals take place almost instantly when the polarity of the driving electric field is changed and hardly any negative displacement is recorded. Similarly to *P-E* hysteresis loops, the displacement butterfly loops also show shifting along the field axis.

Finally, the capacitance vs. voltage (CV) sweeps, Figure 5.11(a) showed hysteresis with the capacitance at 0 V increasing with increased (001) texture content. Knowing the capacitance, *C*, the thickness of the PZT layer, *t*, the area of the capacitors, *A* and the permittivity of free space, ε_0, the dielectric constants were calculated using the equation for a parallel plate capacitor:

$$K_{33} = \frac{Ct}{\varepsilon_0 A} \tag{5.7}$$

Figure 5.11(b) shows that the dielectric constant at 0 V increased linearly with %(001) texture factor. Pure (001) texture showed 20% increase in dielectric constant compared to pure (111) texture. A commonly used figure of merit for piezoelectric sensors, in which voltage is generated in deflected piezoelectric laminates, is $e_{31,f}/(\varepsilon_o K_{33})$. Pure (001) texture, even though has a higher dielectric constant than pure (111) texture, also results in 50% higher figure of merit than pure (111) texture due to the high piezoelectric stress coefficient of the (001) texture. Thus, pure (001) texture is advantageous in low-power MEMS for large displacements and better sensing.

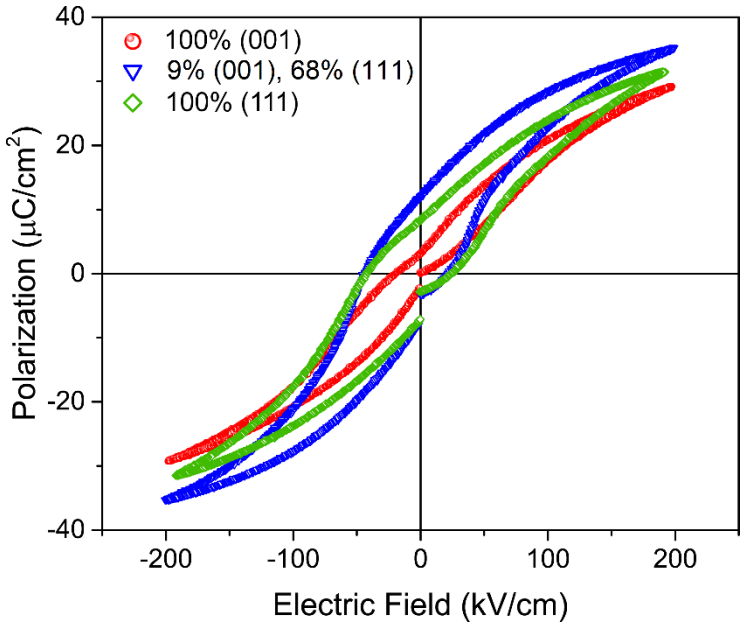

(a)

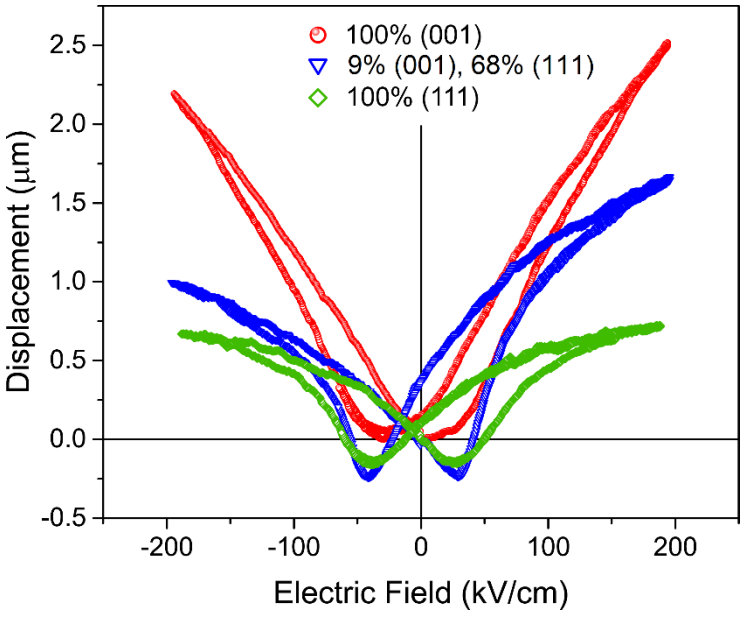

(b)

Figure 5.10 (a) *P-E* hysteresis loops for three samples with textures 100% (001) (#6020), 9% (001) and 68% (111) (#6103), and 100% (111) (#6006) showing tilting, shifting and pinching in the loops. **(b)** Cantilever tip deflection vs. applied electric field during bipolar biasing showing regular butterfly loops for the PZT film textures in (a). Note that the film with (001) texture shows much larger deflection than that with (111) texture.

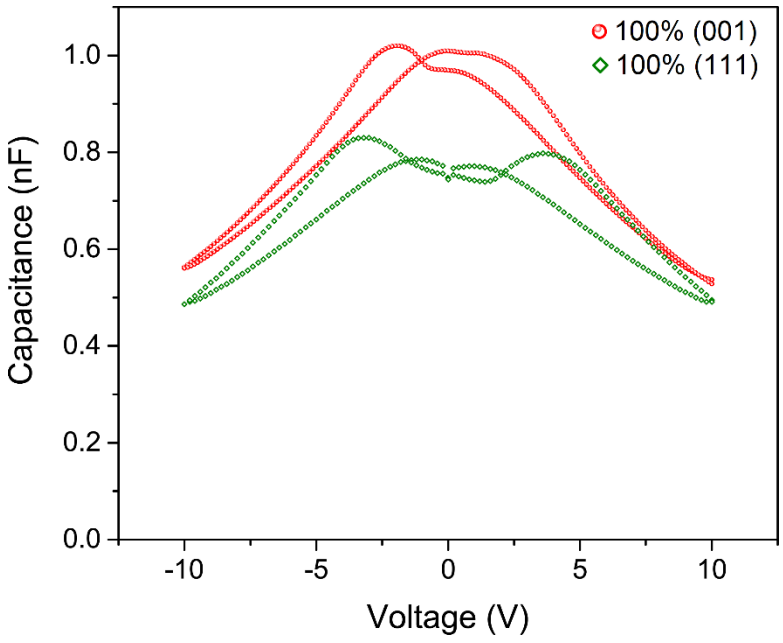

(a)

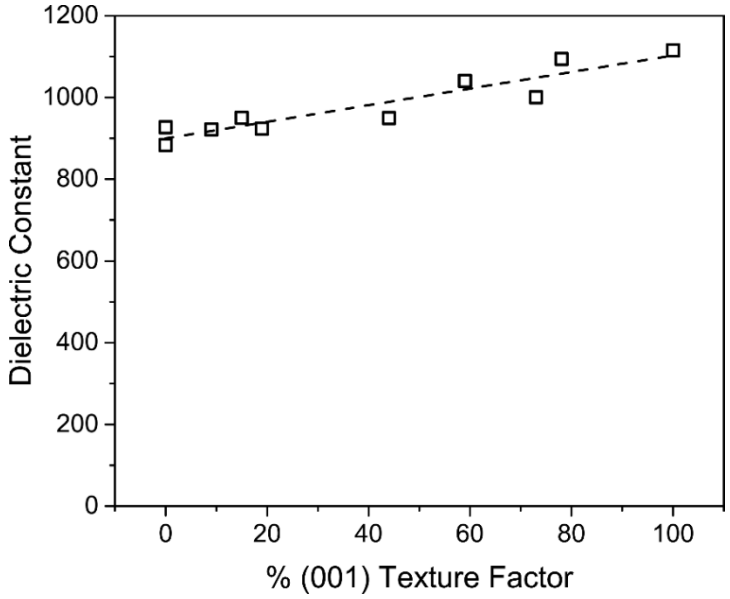

(b)

Figure 5.11 (a) CV sweeps showing hysteresis and increase in capacitance with increase in (001) texture. The sample with 100% (001) texture corresponds to Sample #6020, and the sample with 100% (111) texture corresponds to Sample #6006. **(b)** Dielectric constant, K_{33}, as a function of % (001) texture factor.

5.3 Conclusions

The effect of texture on the ferroelectric and linear piezoelectric response of 500-nm thick PZT films in freestanding SiO_2-TiO_2-Pt-PZT-Pt cantilevers subjected to electrical bias was investigated by measuring the cantilever out-of-plane deflection using a laser Doppler vibrometer. Several PZT film stacks were studied with the textures varying from 100% (001) to 100% (111) texture and several intermediate textures. It was shown that the ferroelectric properties depend strongly on PZT film texture and the effective transverse strain and stress coefficients vary linearly with %(001) and %(111) texture factors: $d_{31,f}$ and $e_{31,f}$ ranged between -40±5 pm/V and -6.9±0.9 C/m^2, respectively, for pure (111) texture and -96±3 pm/V and -12.3±0.4 C/m^2, respectively, for pure (001) texture. With the exception of a sample with 73% (001) and 27% (111) texture, the linear piezoelectric properties and the dielectric constant also increased linearly with (001) texture content. The linear piezoelectric coefficient, $d_{31,f}$ ranged between -17 ± 3 pm/V for pure (111) texture and -42 ± 8 pm/V for pure (001) texture. The dielectric constant of pure (001) texture was found to be 20% higher than that of pure (111) texture. In contrast to all other samples, the sample with 73% (001) and 27% (111) texture showed stable transverse piezoelectric coefficients with electric field which is of major technological importance. In general, PZT films with (001) preferred orientation showed significantly larger piezoelectric response than films with (111) preferred orientation for the same bias level and the same film thickness. Furthermore, pure (001) texture has 50% higher figure of merit in sensing than pure (111) texture and, thus, is more advantageous in low-power MEMS devices.

CHAPTER 6

Conclusions

The objective of this Ph.D. dissertation research was to quantify the effect of film texture on the electromechanical behavior of freestanding PZT stacks. This Chapter summarizes the research outcomes and provides an assessment of the extent to which the dissertation objectives were met.

6.1 Assessment of Dissertation Outcomes

Before this research, correlations between the microstructure and the mechanical property of textured PZT and {111}-textured Pt were sparse and not in general agreement. The major obstacles were posed by existing fabrication methods for textured PZT films, which required major modification of the seed layer, and hence the residual stresses. The available literature has probed the directional dependence of the elastic modulus of PZT films via nanoindentation experiments with several limitations as described in Section 2.1. However, accurate determination of the in-plane modulus of PZT and other films comprising the PZT stacks has further and direct implications on the calculation of the piezoelectric strain coefficient, $d_{31,f}$.

In terms of the mechanical behavior of Pt electrodes that are a major component of a PZT stack due to the high stiffness of Pt, this dissertation research provided combined analytical and experimental data that support the hypothesis for plasticity initiated in epitaxially grown polycrystalline Pt films by an interfacial dislocation network resulting from the mismatch strain between the Pt film and the underlying polycrystalline oxide layer serving as a seed layer. This mechanism of plasticity resulted

in limited ductility due to strain localization and strain rate sensitivity. These results have direct implications on the mechanical reliability of PZT MEMS devices since the metal electrodes constitute an essential part of the structure.

In terms of the PZT layer itself, the results of this research provided experimental evidence of the effect of texture on the ferroelastic property of PZT films and the associated non-linearity in the mechanical response of freestanding PZT stacks. Importantly, although (111) texture is not associated with enhanced ferroelectric and piezoelectric coefficients, it exhibits more linearity and the least amount of domain switching in response to mechanical stress.

Finally, the present experiments allowed us to capture in a clear and unequivocal manner the effect of texture on the ferroelectric and linear piezoelectric response of PZT by taking out the effect of residual stress which is by far the most important factor influencing ferroelectric and ferroelastic properties. The fabricated PZT films had an average film thickness and grain size of 525 ± 15 nm and 95 ± 20 nm without much variation across samples which helped eliminate the influence of these secondary factors. Furthermore, the chemical composition was held constant across the various samples. Specifically, it was shown that pure (001) texture results in the highest piezoelectric strain and stress coefficients which are respectively, 140% and 80% higher than those of pure (111) texture. Thus, the former should be advantageous in low-power MEMS for large displacements and better sensing. The next sub-sections discuss the research outcomes in detail.

6.1.1 Mechanical Response of Epitaxially Grown {111} Pt Thin Films

The experimentally measured elastic modulus of freestanding polycrystalline {111}-textured Pt films with thicknesses 50-1000 nm and different combinations of grain size and film thickness (E_{Pt}=167±2 GPa) agreed well with theoretical estimates for the in-plane modulus of {111}-textured polycrystalline Pt, while the modulus of the underlying 35-50 nm thick polycrystalline (100)-TiO_2 (rutile) seed layer (E_{TiO_2}=195±5 GPa) was 15% lower than the theoretical estimate for (100)-textured polycrystalline

TiO_2. However, its small thickness compared to the epitaxially grown Pt layer increases the uncertainty in the determination of its mechanical stiffness. Importantly, the elastic properties of Pt films were consistent in the entire range of applied uniaxial tension strain rates 10^{-6} - 10 s^{-1}.

The mismatch strain between {111}-Pt films and the underlying (100)-TiO_2 seed layer gave rise to an interfacial dislocation network, which, in turn, determined the initiation of plastic deformation in Pt. Experiments showed that the flow stress increased, while the plastic strain accumulation at failure decreased with decreasing Pt film thickness. A modified Thompson model developed for polycrystalline columnar metal films that accounted for the combined effect of film thickness and grain size provided good predictions for the experimentally determined proportional limit of Pt films. The modification to Thompson's model was necessary for the present study because the grain diameter to height aspect ratio $d/h \leq 1$, the TiO_2 substrate was not rigid given its thickness and elastic modulus relative to Pt, and dislocations were shown to be more likely to emanate at the Pt/TiO_2 interface rather than the free Pt film surface, as discussed in detail in Sections 3.3.1 and 3.3.2.

However, the yield stress was underestimated by the same model. To address this issue, a Taylor strain hardening model was superimposed to the modified Thompson model to account for additional hardening as a result of dislocation interactions during plastic deformation, which provided good predictions for the evolution of flow stress with plastic strain. The combined model, which is also a Hall-Petch grain strengthening model, predicted well the evolution of flow stress with plastic strain.

6.1.2 Effect of Texture on Mechanical Response of PZT Thin Films

The effect of texture on the open-circuit mechanical response of PZT film stacks was experimentally investigated. The measured open circuit modulus varied linearly with %(001) and %(111) texture factors values ranging between 90 ± 2 GPa for pure (001) texture and 122 ± 3 GPa for pure (111) texture, and a linear increase with increasing (111) texture content. Pure (001) texture resulted in most nonlinear stress-strain response

and (111) texture in the least nonlinearity, indicating easier 90˚ domain switching in pure (001)-textured films. Such non-linearities were due to ferroelasticity; a polycrystalline ferroelectric material at the morphotropic phase boundary (MPB) of any texture shows considerable nonlinear macroscopic strain due to non-180˚ domain switching. To explain the texture dependence of ferroelasticity, a simple micromechanics model based on the isotropic Eshelby's inclusion problem was developed. The model captured the change in ferroelastic domain switching with texture: (001) texture showed the most non-linearity with the model predicting that up to ~17% of 90˚ domains switched at the maximum tensile stress applied to the (001) texture. On the other hand, PZT films with (111) texture demonstrated switching of only ~10% of 90˚ domains, as also evidenced by the considerably more linear behavior of PZT films with (111) texture.

6.1.3 Effect of Texture on the Ferroelectric Response of PZT Thin Films

The ferroelectric behavior of ~500 nm thick freestanding, sol-gel deposited, $PbZr_{0.52}Ti_{0.48}O_3$ (PZT) film stacks, with PZT texture varying from 100% (001) to 100% (111) was investigated. The ferroelectric properties were computed from the out-of-plane deflection of PZT unimorphs, obtained via a laser Doppler vibrometer. The ferroelectric coefficients depended strongly on PZT film texture, while the effective transverse strain and stress coefficients varied linearly with %(001) and %(111) texture factors: $d_{31,f}$ and $e_{31,f}$ were -40 ± 5 pm/V and -6.9 ± 0.9 C/m^2, respectively, for pure (111) texture and -96 ± 3 pm/V and -12.3 ± 0.4 C/m^2, respectively, for pure (001) texture. The effective stress coefficients obtained in this study matched those reported in the literature for the two extreme textures: 100% (001) and 100% (111). The transverse piezoelectric coefficients varied linearly with %(001) and %(111) texture factors: $d_{31,f}$ increased from -17 ± 3 pm/V for pure (111) texture to -42 ± 8 pm/V for pure (001) texture, namely, the linear piezoelectric strain coefficient of (001) was ~150% higher than (111) texture. Furthermore, the dielectric constant increased with (001) texture content and (001) texture showed 20% higher dielectric constant than (111) texture. In general, PZT films with (001) preferred orientation showed larger piezoelectric response than films with (111) preferred orientation for the same bias level and the same film thickness. Finally,

one of the samples with 73% (001) and 27% (111) texture showed stable transverse piezoelectric coefficients with electric field which might be exploited in low-power MEMS devices.

6.2 Future Directions

In all the experiments performed in this dissertation research, the exact magnitudes of the residual stresses in each layer in the PZT stack were unknown. To obtain a better understanding of the PZT texture development during fabrication, the residual stresses in each layer could be monitored during fabrication. The net residual thermal stress on the PZT layer at the freestanding configuration of the PZT stack could be accounted for in the mechanical measurements reported in this study.

Along the same lines, measurement of the ferroelectric response as a function of applied tensile pre-stress (e.g. [15]) would complement the ferroelectric studies in this dissertation; tensile pre-stresses have been known to cause in-plane mechanical clamping of domains leading to decrease in ferroelectric coefficients. When combined with the data in Chapters 4 and 5, it would provide a more complete picture of the combined effect of electric field and stresses on domain switching. Such experiments proved challenging because of electrical connectivity issues in our SiO_2-TiO_2-Pt-PZT-Pt-ALD specimens where the top non-conducting ALD layer prevented access to the bottom Pt layer.

Finally, there are several micromechanical models for polycrystalline ferroelectric materials [149-152] with each grain consisting of either single or multi-domains. Domain switching in the presence of electrical and/or mechanical stimuli is determined by an energy-based criterion, with either intergranular interactions neglected or considered through the Eshelby inclusion model or with the aid of finite element calculations. Small modifications to the above models, could be made to account for grain orientation and stress dependence of the ferroelectric and/or ferroelastic response of thin films, and compared to the experimental results in Chapters 4 and 5. This could lead to better

understanding of the physical processes occurring under electrical and/or mechanical bias in textured thin PZT films.

References

[1] K. Hyeoungwoo, S. Priya, H. Stephanou, and K. Uchino. "Consideration of impedance matching techniques for efficient piezoelectric energy harvesting." IEEE transactions on ultrasonics, ferroelectrics, and frequency control, vol. 54, pp. 1851-1859, 2007.

[2] G. L. Smith, J. S. Pulskamp, L. M. Sanchez, D. M. Potrepka, R. M. Proie, T. G. Ivanov, R. Q. Rudy, W. D. Nothwang, S. S. Bedair, C. D. Meyer, and R. G. Polcawich, "PZT-based piezoelectric MEMS technology," J. Am. Ceram. Soc., vol. 95, pp. 1777–1792, 2012.

[3] J. S. Pulskamp, R. G. Polcawich, R. Q. Rudy, S. S. Bedair, R. M. Proie, T. Ivanov, and G. L. Smith. "Piezoelectric PZT MEMS technologies for small-scale robotics and RF applications." MRS bulletin, vol. 37, pp. 1062-1070, 2012.

[4] M. Murata, T. Kondoh, T. Yagi, N. Funatsu, K. Tanaka, H. Tsukuni, K. Ohno, H. Usami, R. Nayve, N. Inoue, S. Seto, and N. Morita, "High-resolution piezo inkjet printhead fabricated by three dimensional electrical connection method using through glass VIA," Proceedings of the IEEE International Conference on Micro Electro Mechanical Systems (MEMS), pp. 507–510, 2009.

[5] P. Muralt, "Piezoelectric Films for Innovations in the Field of MEMS and Biosensors," Piezoelectricity. Springer Berlin Heidelberg, pp. 351-376, 2008.

[6] J. R. Bronson, J. S. Pulskamp, R. G. Polcawich, C. M. Kroninger, and E. D. Wetzel, "PZT mems actuated flapping wings for insect-inspired robotics," Proc. IEEE Int. Conf. Micro Electro Mech. Syst., pp. 1047–1050, 2009.

[7] H. Nazeer, M. D. Nguyen, Ö. S. Sukas, G. Rijnders, L. Abelmann, and M. C. Elwenspoek, "Compositional dependence of the Young's modulus and piezoelectric coefficient of (110)-oriented pulsed laser deposited pzt thin films," Journal of Microelectromechanical Systems, vol. 24, pp. 166–173, 2015.

[8] Q. Wang, Y. Ding, Q. Chen, M. Zhao, and J. Cheng, "Crystalline orientation dependence of nanomechanical properties of Pb(Zr0.52Ti0.48)O3 thin films," Appl. Phys. Lett., vol. 86, p. 2903, 2005.

[9] P. Delobelle, G. S. Wang, E. Fribourg-Blanc, and D. Remiens, "Indentation modulus and hardness of $Pb(Zr,Ti)O_3$ sol-gel films deposited on Pt and $LaNiO_3$ electrodes. An estimation of the C_{ij}^D compliances," J. Eur. Ceram. Soc., vol. 27, pp. 223–230, 2007.

[10] H. Wu, L. Wu, Q. Sun, W. Fei, and S. Du, "Mechanical properties of sol-gel derived lead zirconate titanate thin films by nanoindentation," Appl. Surf. Sci., vol. 254, pp. 5492–5496, 2008.

[11] I. Kanno, S. Fujii, T. Kamada, and R. Takayama, "Piezoelectric properties of c-axis oriented $Pb(Zr,Ti)O_3$ thin films," Appl. Phys. Lett., vol. 70, p. 1378, 1997.

[12] X. J. Zheng, Y. C. Zhou, and J. Y. Li. "Nano-indentation fracture test of $Pb(Zr_{0.52}Ti_{0.48})O_3$ ferroelectric thin films." Acta Materialia, vol. 51, pp. 3985-3997, 2003.

[13] P. Delobelle, E. Fribourg-Blanc, and D. Remiens. "Mechanical properties determined by nanoindentation tests of $[Pb(Zr,Ti)O_3]$ and $[Pb(Mg_{1/3}Nb_{2/3})_{1-x}Ti_xO_3]$ sputtered thin films." Thin Solid Films, vol. 515, pp. 1385-1393, 2006.

[14] D. F. Bahr, J. S. Robach, J. S. Wright, L. F. Francis, and W. W. Gerberich, "Mechanical deformation of PZT thin films for MEMS applications", Materials Science and Engineering: A, vol. 259, pp. 126-131, 1999.

[15] S. Yagnamurthy, I. Chasiotis, J. Lambros, R. G. Polcawich, J. S. Pulskamp, and M. Dubey, "Mechanical and ferroelectric behavior of PZT-based thin films," J. Microelectromechanical Syst., vol. 20, pp. 1250–1258, 2011.

[16] S. Wakabayashi, "Study on mechanical characteristics of PZT thin film for sensors and actuators," Proc. SPIE, vol. 2639, pp. 304–314, 1995.

[17] S. G. Hong, M. Kim, S. B. Lee, and C. S. Lee, "Characterization of deformation behaviors and elastic moduli of multilayered films in piezoelectric inkjet head," J. Microelectromechanical Syst., vol. 17, pp. 1155–1163, 2008.

[18] S. Watanabe, T. Fujiu, and T. Fujii, "Effect of poling on piezoelectric properties of lead zirconate titanate thin films formed by sputtering," Appl. Phys. Lett., vol. 66, p. 1481, 1995.

[19] D. L. Polla and L. F. Francis, "Ferroelectric thin films in micro-electromechanical systems applications," MRS Bull., vol. 21, pp. 59–65, 1996.

[20] J. F. Shepard, P. J. Moses, and S. Trolier-McKinstry, "The wafer flexure technique for the determination of the transverse piezoelectric coefficient (d_{31}) of PZT thin films," Sensors and Actuators A: Physical, vol. 71, pp. 133–138, 1998.

[21] D. L. DeVoe and A. P. Pisano, "Modeling and optimal design of piezoelectric cantilever microactuators," J. Microelectromechanical Syst., vol. 6, pp. 266–270, 1997.

[22] M.S. Weinberg, "Working equations for piezoelectric actuators and sensors," J. Microelectromechanical Syst., vol. 8, pp. 529–533, 1999.

[23] C. Ayela, L. Nicu, C. Soyer, E. Cattan, and C. Bergaud, "Determination of the d_{31} piezoelectric coefficient of $PbZr_xTi_{1-x}O_3$ thin films using multilayer buckled micromembranes," J. Appl. Phys., vol. 100, p. 054908, 2006.

[24] J. Akedo and M. Lebedev, "Piezoelectric properties and poling effect of $Pb(Zr,Ti)O_3$ thick films prepared for microactuators by aerosol deposition," Appl. Phys. Lett., vol. 77, pp. 1710–1712, 2000.

[25] G. R. Fox, R. G. Polcawich, D. M. Potrepka, and L. M. Sanchez, "Stylo-epitaxial piezoelectric and ferroelectric devices and method of manufacturing," US Patent No. 20130093290, 2013.

[26] G. Dehm, T. J. Balk, H. Edongue, and E. Arzt, "Small-scale plasticity in thin Cu and Al films," Microelectronic Engineering, vol. 70, pp. 412–424, 2003.

[27] R. Venkatraman and J. Bravman, "Separation of film thickness and grain boundary strengthening effects in Al thin films on Si," J. Mater. Res., vol. 7, pp. 2040–2048, 1992.

[28] M. Hommel and O. Kraft, "Deformation behavior of thin copper films on deformable substrates," Acta Mater., vol. 49, pp. 3935–3947, 2001.

[29] N. Ledermann, P. Muralt, J. Baborowski, S. Gentil, K. Mukati, M. Cantoni, A. Seifert, and N. Setter, "{100}-Textured, piezoelectric $Pb(Zr_x,Ti_{1-x})O_3$ thin films for MEMS:

integration, deposition and properties," Sensors Actuators A Phys., Vol. 105, pp. 162–170, 2003.

[30] X. X.-H. Du, J. Zheng, U. Belegundu, and K. Uchino, "Crystal orientation dependence of piezoelectric properties of lead zirconate titanate near the morphotropic phase boundary," Appl. Phys. Lett., vol. 72, pp. 2421-2423, 1998.

[31] S. Trolier-McKinstry and P. Muralt, "Thin film piezoelectrics for MEMS," J. Electroceramics, vol. 12, pp. 7–17, 2004.

[32] F. Xu, R.A. Wolf, T. Yoshimura, and S. Trolier-McKinstry, "Piezoelectric films for MEMS applications," Proceedings. 11th Int. Symp. Electrets, IEEE, pp. 386–396, 2002.

[33] D. Ambika, V. Kumar, K. Tomioka, and I. Kanno, "Deposition of PZT thin films with {001}, {110}, and {111} crystallographic orientations and their transverse piezoelectric characteristics," Adv. Mater. Lett., vol. 3, pp. 102–106, 2012.

[34] K. Kakimoto, H. Kakemoto, S. Fujita, and Y. Masuda, "Control of crystal orientation and piezoelectric response of lead zirconate titanate thin films near the morphotropic phase boundary," J. Am. Ceram. Soc. Vol. 85, pp. 1019–1021, 2004.

[35] T. A. Berfield, R. J. Ong, D. A. Payne, and N. R. Sottos, "Residual stress effects on piezoelectric response of sol-gel derived lead zirconate titanate thin films," J. Appl. Phys. Vol. 101 p. 24102, 2007.

[36] R. J. Ong, T. Berfield, N. R. Sottos, and D. Payne, "Sol-Gel derived $Pb(Zr,Ti)O_3$ thin films: Residual stress and electrical properties," J. Eur. Ceram. Soc. Vol. 25, pp. 2247–2251, 2005.

[37] L. Lian, and N. R. Sottos. "Stress effects in sol-gel derived ferroelectric thin films." J. Appl. Phys, Vol. 95, pp. 629-634, 2004.

[38] B. A. Tuttle, J. A. Voigt, T. J. Garino, D. C. Goodnow, R. W. Schwartz, D. L. Lamppa, T. J. Headley, and M. O. Eatough. "Chemically prepared $Pb(Zr,Ti)O_3$ thin films: the effects of orientation and stress," ISAF '92 Proc. Eighth IEEE Int. Symp. Appl. Ferroelectr.; p. 344, 1992.

[39] L. Lian, and N. R. Sottos, "Effects of thickness on the piezoelectric and dielectric properties of lead zirconate titanate thin films", J. Appl. Phys., vol. 87, pp. 3941-3949, 2000.

[40] F. Griggio, and S. Trolier-McKinstry, Grain size dependence of properties in lead nickel niobate-lead zirconate titanate films, J. Appl. Phys., vol. 107, 2010.

[41] B. Jaffe, W. R. Cook, and H. Jaffe, "Piezoelectric Ceramics". Academic, New York, 1971.

[42] K. C. Chen and J. D. Mackenzie, "Crystallization kinetics of metallo-organics derived PZT thin film," MRS Proc., vol. 180. pp. 663–668, 1990.

[43] S. Chen and I. Chen, "Temperature-time texture transition of $Pb(Zr_{1-x}Ti_x)O_3$ thin films: II, heat treatment and compositional effects," J. Am. Chem. Soc., vol. 77, no. 9, pp. 2337–2344, 1994.

[44] L. M. Sanchez, D. M. Potrepka, G. R. Fox, I. Takeuchi, K. Wang, L. A. Bendersky, and R. G. Polcawich, "Optimization of $PbTiO_3$ seed layers and Pt metallization for PZT-based piezoMEMS actuators," J. Mater. Res., vol. 28, no. 14, pp. 1920–1931, 2013.

[45] P. Muralt, T. Maeder, L. Sagalowicz, S. Hiboux, S. Scalese, D. Naumovic, R. G. Agostino, N. Xanthopoulos, H. J. Mathieu, L. Patthey, and E. L. Bullock, "Texture control of $PbTiO_3$ and $Pb(Zr,Ti)O_3$ thin films with TiO_2 seeding," J. Appl. Phys., vol. 83, pp. 3835-3841, 1998.

[46] S. Hiboux and P. Muralt, "Mixed titania-lead oxide seed layers for PZT growth on Pt(111): A study on nucleation, texture and properties," J. Eur. Ceram. Soc., vol. 24, pp. 1593–1596, 2004.

[47] I. Kanno, H. Kotera, and K. Wasa, "Measurement of transverse piezoelectric properties of PZT thin films," Sensors Actuators, A Phys., vol. 107, pp. 68–74, 2003.

[48] S. Chen and I. Chen, "Temperature-time texture transition of $Pb(Zr_{1-x}Ti_x)O_3$ thin films: I, role of Pb-rich intermediate phases," J. Am. Ceram. Soc., vol. 77, pp. 2332–2336, 1994.

[49] K. Aoki, Y. Fukuda, K. Numata, and A. Nishimura, "Effects of titanium buffer layer on lead-zirconate-titanate crystallization processes in sol-gel deposition technique," Jpn. J. Appl. Phys., vol. 34, pp. 192–195, 1995.

[50] K. G. Brooks, I. M. Reaney, R. Klissurska, Y. Huang, L. Bursill, and N. Setter, "Orientation of rapid thermally annealed lead zirconate titanate thin films on (111) Pt substrates," J. Mater. Res., vol. 9, pp. 2540–2553, 1994.

[51] S. Mhin, K. Nittala, C. Cozzan, K. Kim, D. S. Robinson, L. M. Sanchez, R. G. Polcawich, and J. L. Jones, "Role of the $PbTiO_3$ seed layer on the crystallization behavior of PZT thin films," J. Am. Ceram. Soc., vol. 98, pp. 1407–1412, 2015.

[52] Y. Shindo, and F. Narita, "Piezomechanics in PZT Stack Actuators for Cryogenic Fuel Injectors," in Smart Actuation and Sensing Systems - Recent Advances and Future Challenges, G. Berselli (Ed.), INTECH Open Access Publisher, 2012.

[53] R. J. Ong, D. A. Payne, and N. R. Sottos, "Processing effects for integrated PZT: Residual stress, thickness, and dielectric properties," J. Am. Ceram. Soc., vol. 88, pp. 2839–2847, 2005.

[54] L. B. Freund, "The stability of a dislocation threading a strained layer on a substrate," J. Appl. Mech., vol. 54, p. 553, 1987.

[55] W. D. Nix, "Mechanical properties of thin films," Metall. Trans. A, vol. 20, pp. 2217–2245, 1989.

[56] C. V. Thompson, "The yield stress of polycrystalline thin films," J. Mater. Res., vol. 8, pp. 237–238, 1993.

[57] B. von Blanckenhagen, P. Gumbsch, and E. Arzt, "Dislocation sources and the flow stress of polycrystalline thin metal films," Philos. Mag. Lett., vol. 83, pp. 1–8, 2003.

[58] G. Dehm, T. Wagner, T. Balk, and E. Arzt, "Plasticity and interfacial dislocation mechanisms in epitaxial and polycrystalline al films constrained by substrates," J. Mater. Sci. Technol., vol. 18. pp. 113–117, 2002.

[59] G. Dehm and E. Arzt, “In situ transmission electron microscopy study of dislocations in a polycrystalline Cu thin film constrained by a substrate,” Appl. Phys. Lett., vol. 77, pp. 1126–1128, 2000.

[60] R. Keller, S. P. Baker, and E. Arzt, “Quantitative analysis of strengthening mechanisms in thin Cu films: Effects of film thickness, grain size, and passivation,” J. Mater. Res., vol. 13, pp. 1307–1317, 1998.

[61] R. Vinci, E. Zielinski, and J. Bravman, “Thermal strain and stress in copper thin films,” Thin Solid Films, vol. 262, pp. 142–153, 1995.

[62] D. A. Berlincourt, C. Cmolik, and H. Jaffe, “Piezoelectric properties of polycrystalline lead titanate zirconate compositions,” Proc. IRE, vol. 48, 1960.

[63] M. Dekkers, H. Boschker, M. van Zalk, M. Nguyen, H. Nazeer, E. Houwman, and G. Rijnders, “The significance of the piezoelectric coefficient $d_{31,eff}$ determined from cantilever structures”. J. Micromech. Microeng., vol. 23, pp. 1-7, 2013.

[64] K. R. Oldham, J. S. Pulskamp, R. G. Polcawich, and M. Dubey, “Thin-film PZT lateral actuators with extended stroke,” J. Microelectromech. Syst., vol. 17, pp. 890-899. 2008.

[65] D. Das, B. Power, J. P. Martin, R. G. Polcawich, and I. Chasiotis, “Role of oxide seed layer in plastic response of epitaxially grown textured metal films”, Acta Mater., vol.112, pp. 390–402, 2016.

[66] D. Das, L. Sanchez, J. Martin, B. Power, S. Isaacson, R. G. Polcawich, and I. Chasiotis, “Control of mechanical response of freestanding $PbZr_{0.52}Ti_{0.48}O_3$ films through texture”. Applied Physics Letters, vol. 109, p. 131905, 2016.

[67] K. N. Jonnalagadda, I. Chasiotis, S. Yagnamurthy, J. Lambros, J. Pulskamp, R. Polcawich, and M. Dubey, “Experimental investigation of strain rate dependence of nanocrystalline Pt films”, Exp Mech, vol. 50, pp. 25-35, 2010.

[68] J. Mencik, and M. V. Swain, “Mechanical Properties of Platinum Films on Silicon and Glass determined by ultra-microindentation”, Materials Research Society Symposium Proceedings, vol. 356, p. 729, 1994.

[69] M. V. Swain, and J. Menčík. "Mechanical property characterization of thin films using spherical tipped indenters", Thin Solid Films, vol. 253, pp. 204-211, 1994.

[70] H. Lee, R. A. Coutu, S. Mall, and K. D. Leddy, “Characterization of metal and metal alloy films as contact materials in MEMS switches”, J. Micromech. Microeng., vol.16, pp. 557, 2006.

[71] S. Hyun, O. Kraft, and R. P. Vinci, “Mechanical behavior of Pt and Pt–Ru solid solution alloy thin films”, Acta Mater., vol. 52, pp. 4199–4211, 2004.

[72] A. L. Romasco, L. H. Friedman, L. Fang, R. A. Meirom, T. E. Clark, R. G. Polcawich, J. S. Pulskamp, M. Dubey, and C. L. Muhlstein, “Deformation behavior of nanograined platinum films”, Thin Solid Films, vol. 518, pp. 3866-3874, 2010.

[73] Y. Xiang, and J. J. Vlassak. "Bauschinger effect in thin metal films." Scripta Materialia, vol. 53, pp. 177-182, 2005.

[74] H. Nazeer, M. D. Nguyen, L. A. Woldering, L. Abelmann, G. Rijnders, and M. C. Elwenspoek, “Determination of the Young's modulus of pulsed laser deposited epitaxial

PZT thin films", Journal of Micromechanics and Microengineering, vol. 21, p. 074008, 2011.

[75] M. C. Salvadori, I. G. Brown, A. R. Vaz, L. L. Melo, and M. Cattani, "Measurement of the elastic modulus of nanostructured gold and platinum thin films", Phys Rev. B, vol. 67, pp. 153404 1-4, 2003.

[76] D. C. Hurley, V. K. Tewary, and A. J. Richards. "Thin-film elastic-property measurements with laser-ultrasonic SAW spectrometry", Thin Solid Films, vol. 398, pp. 326-330, 2001.

[77] C. J. Shute and J. B. Cohen, "Determination of yielding and debinding in Al–Cu thin films from residual stress measurements via diffraction", J. Mater. Res., vol. 6, p. 950, 1991.

[78] S. Bader, E. M. Kalaugher, and E. Arzt, "Comparison of mechanical properties and microstructure of Al(1 wt.%Si) and Al(1 wt.%Si, 0.5 wt.%Cu) thin films", Thin Solid Films, vol. 263, pp. 175-184, 1995.

[79] I. Chasiotis, and W. G. Knauss, "Experimentation at the micron and submicron Scale", in Comprehensive Structural Integrity Vol. 8. Interfacial and Nanoscale Failure. Volume Editors: W. Gerberich and W. Yang, Elsevier Science, Oxford, U.K., pp. 41-87, 2003.

[80] G. M. Pharr and W. C. Oliver, "Measurement of thin film mechanical properties using nanoindentation", MRS Bulletin, vol. 17, pp. 28-28, 1992.

[81] R. Saha and W. D. Nix, "Effects of the substrate on the determination of thin film mechanical properties by nanoindentation", Acta Materialia, vol. 50, pp. 23-38, 2002.

[82] H. Buckle, in J. W. Westbrook and H. Conrad, Eds., "The science of hardness testing and its applications", American Society for Metals, Metal Park, OH, pp. 453-491, 1973.

[83] J. Mencik, D. Munz, E. Quandt, E. R. Weppelmann, and M. V. Swain, "Determination of elastic modulus of thin layers using nanoindentation," Journal of Materials Research, vol. 12, pp. 2475-2484, 1997.

[84] P. Delobelle, G. S. Wang, E. Fribourg-Blanc, and D. Remiens. "Mechanical properties measured by nano-indentation of Pb $(Zr,Ti)O_3$ sol–gel films deposited on Pt and $LaNiO_3$ electrodes." Surface and Coatings Technology, vol. 201, pp. 3155-3162, 2006.

[85] I. Chasiotis, and W. G. Knauss, "A new microtensile tester for the study of MEMS materials with the aid of atomic force microscopy", Experimental Mechanics, vol. 42, pp. 51-57, 2002.

[86] S. W. Cho, and I. Chasiotis. "Elastic properties and representative volume element of polycrystalline silicon for MEMS." Experimental mechanics, vol. 47, pp. 37-49, 2007.

[87] M. Naraghi, I. Chasiotis, H. Kahn, Y. Wen and Y. Dzenis, "Novel method for mechanical characterization of polymeric nanofibers", Review of Scientific Instruments, vol. 78, p. 085108, 2007.

[88] D. M. Newns, B. G. Elmegreen, X. H. Liu, and G. J. Martyna, "The piezoelectronic transistor: A nanoactuator-based post-CMOS digital switch with high speed and low power", MRS bulletin, vol. 37, pp. 1071-1076, 2012.

[89] C. B. Eom, and S. Trolier-McKinstry. “Thin-film piezoelectric MEMS”, MRS Bulletin, vol. 37, pp. 1007-1017, 2011.

[90] M. A. Dubois, and P. Muralt, “Measurement of the effective transverse piezoelectric coefficient $e_{31,f}$ of AlN and $Pb(Zr_x,Ti_{1-x})O_3$ thin films”, Sensors Actuators, A Phys., vol. 77, pp. 106–112, 1999.

[91] B. Piekarski, "Lead zirconate titanate thin films for piezoelectric actuation and sensing of MEMS resonators", PhD thesis, University of Maryland, 2005.

[92] J. B. Vechembre, and G. R. Fox. "Sintering of screen-printed platinum thick films for electrode applications", Journal of Materials Research, vol. 16, pp. 922-931, 2001.

[93] A. J. Kalkman, A. H. Verbruggen, G. C. A. M. Janssen, and S. Radelaar, “Transient creep in free-standing thin polycrystalline aluminum films”, J. Appl. Phys., vol. 92, pp. 4968-4975, 2002.

[94] K. Jonnalagadda, N. Karanjgaokar, I. Chasiotis, J. Chee, and D. Peroulis, “Strain rate sensitivity of nanocrystalline Au films at room temperature”, Acta Materialia, vol. 58, pp. 4674-4684, 2010.

[95] P. Ekkels, X. Rottenberg, R. Puers, and H. A. C. Tilmans, “Evaluation of platinum as a structural thin film material for RF-MEMS devices”, J. Micromech. Microeng., vol. 19, pp. 065010 1-8, 2009.

[96] G. R. Fox, S. Trolier-McKinstry, S. B. Krupanidhi, and L. M. Casas, “$Pt/Ti/SiO_2/Si$ substrates”, Journal of materials research, vol. 10, pp. 1508-1515, 1995.

[97] L. M. Sanchez, D. M. Potrepka, G. R. Fox, I. Takeuchi, and R. G. Polcawich, “Improving PZT thin film texture through Pt metallization and seed layers”, MRS Proceedings, vol.1299, pp. 53-58, 2011.

[98] R. A. Meirom, D. H. Alsem, A. L. Romasco, T. Clark, R. G. Polcawich, J. S. Pulskamp, M. Dube, R. O. Ritchie, and C. L. Muhlstein, “Fatigue-induced grain coarsening in nanocrystalline platinum films”, Acta Materialia, vol. 59, pp.1141-1149, 2011.

[99] M. J. Kobrinsky, and C. V. Thompson, “The thickness dependence of the flow stress of capped and uncapped polycrystalline Ag thin films”, Appl. Phys. Lett., vol. 73, pp. 2429–2431, 1998.

[100] H. D. Espinosa, B. C. Prorok, and B. Peng, “Plasticity size effects in free-standing submicron polycrystalline FCC films subjected to pure tension”, J. Mech. Phys. Solids, vol. 52, pp. 667–689, 2004.

[101] A. A. Taylor, S. H. Oh, and G. Dehm, “Microplasticity phenomena in thermomechanically strained nickel thin films”, J. Mater. Sci., vol. 45, pp. 3874–3881, 2010.

[102] M. Murakami, “Thermal strain in thin lead films III: Dependences of the strain on film thickness and on grain size”, Thin Solid Films, vol. 59, pp. 105–116, 1979.

[103] P. Majumder, R. Katamreddy, and C. G. Takoudis, “Characterization of atomic layer deposited ultrathin HfO_2 film as a diffusion barrier in Cu metallization”, MRS Proc., vol. 990, pp. 97–102, 2007.

[104] J. S. Reid, E. Kolawa, C. M. Garland, M. A. Nicolet, F. Cardone, D. Gupta, and R. P. Ruiz, “Amorphous (Mo, Ta, or W)–Si–N diffusion barriers for Al metallizations”, J. Appl. Phys., vol. 79, p. 1109, 1996.

[105] G. R. Fox, R. G. Polcawich, and D. M. Potrepka, “Thermally oxidized seed layers for the production of {001} textured electrodes and PZT devices and method of making”, US 8866367 B2, 2014.

[106] D. M. Potrepka, G. R. Fox, L. M. Sanchez, and R. G. Polcawich, “Pt/TiO_2 growth templates for enhanced PZT films and MEMS devices”, MRS Proc., vol. 1299, pp. 67–72, 2011.

[107] P. A. Beck, M. L. Holzworth, and P. R. Sperry, “Effect of a dispersed phase on grain growth in Al-Mn alloys”, Trans. Am. Inst. Min. Met. Eng, vol. 180, pp. 163–192, 1949.

[108] W. W. Mullins, “The effect of thermal grooving on grain boundary motion”, Acta Metall., vol. 6, pp. 414–427, 1958.

[109] K. Barmak, E. Eggeling, D. Kinderlehrer, R. Sharp, S. Ta’asan, A. D. Rollett, and K. R. Coffey, “Grain growth and the puzzle of its stagnation in thin films: The curious tale of a tail and an ear”, Prog. Mater. Sci., vol. 58, pp. 987–1055, 2013.

[110] D. T. Carpenter, J. M. Rickman, and K. Barmak, “A methodology for automated quantitative microstructural analysis of transmission electron micrographs”, J. Appl. Phys., vol. 84 p. 5843, 1998.

[111] C. R. M. Grovenor, H. T. G. Hentzell, and D. A. Smith, “The development of grain structure during growth of metallic films”, Acta Metall., vol. 32, pp. 773–781, 1984.

[112] J. F. Nye, “Physical properties of crystals: their representation by tensors and matrices”, Oxford: At the Clarendon Press, 1957.

[113] S. M. Collard, and R. B. McLellan, “High-temperature elastic constants of platinum single crystals”, Acta Metall. Mater., vol. 40, pp. 699–702, 1992.

[114] V. Swamy, and J. D. Gale, “Transferable variable-charge interatomic potential for atomistic simulation of titanium oxides”, Phys. Rev. B, vol. 62, pp. 5406–5412, 2000.

[115] J. M. Gere, and B. J. Goodno, “Mechanics of materials”, Seventh Edition, Cengage Learning, 2009.

[116] R. Hill, “The elastic behavior of a crystalline aggregate”, Proc. Phys. Soc. A, vol. 65, p. 349, 1952.

[117] R. Carel, “Grain growth and texture evolution in thin films”, PhD Thesis, MIT, 1995.

[118] L. B. Freund, and S. Suresh, “Thin film materials - stress, defect formation and surface evolution”, Cambridge University Press, 2004.

[119] W. G. Wolfer, T. Okita, and D. M. Barnett, “Motion and rotation of small glissile dislocation loops in stress fields”, Phys. Rev. Lett., vol. 92, p. 085507, 2004.

[120] H. Gao, “Stress concentration at slightly undulating surfaces”, J. Mech. Phys. Solids, vol. 39, pp. 443–458, 1991.

[121] G. E. Beltz, and L.B. Freund, “On the nucleation of dislocations at a crystal surface”, Phys. Stat. Sol., vol. 180, pp. 303–313, 1993.

[122] L. Y. Chen, M. He, J. Shin, G. Richter, and D. S. Gianola, “Measuring surface dislocation nucleation in defect-scarce nanostructures”, Nat. Mater., vol. 14, pp. 707–713, 2015.

[123] W. F. Hosford, “Mechanical behavior of materials”, Cambridge University Press, 2005.

[124] M. F. Ashby, “The deformation of plastically non-homogeneous materials”, Philos. Mag., vol. 21, pp. 399–424, 1970.

[125] K. T. Ramesh, “Nanomaterials”, Springer US, Boston, MA, 2009.

[126] W. O. Soboyejo, and T. S. Srivatsan, “Advanced structural materials”, CRC Press, 2006.

[127] N. Hansen, “Boundary strengthening in undeformed and deformed polycrystals”, Mater. Sci. Eng. A, vol. 409, pp. 39–45, 2005.

[128] T. J. Rupert, “Strain localization in a nanocrystalline metal: atomic mechanisms and the effect of testing conditions”, J. Appl. Phys., vol. 114, pp. 033527, 2013.

[129] M. Chen, E. Ma, K. J. Hemker, H. Sheng, Y. Wang, and X. Cheng, “Deformation twinning in nanocrystalline aluminum”, Science, vol. 300, pp. 1275–1277, 2003.

[130] S. H. Oh, M. Legros, D. Kiener, P. Gruber, and G. Dehm, “In situ TEM straining of single crystal Au films on polyimide: change of deformation mechanisms at the nanoscale”, Acta Mater., vol. 55, pp. 5558–5571, 2007.

[131] P. A. Gruber, E. Arzt, and R. Spolenak, “Brittle-to-ductile transition in ultrathin Ta/Cu film systems”, J. Mater. Res., vol. 24, pp. 1906–1918, 2011.

[132] L. Dan, "Investigation into the effect of substrate on $Pb(Zr_{0.52}Ti_{0.48})O_3$ films for MEMS application", PhD Thesis, Auburn University, 2011.

[133] L. M. Sanchez, “Optimization of PZT (52/48) through improved platinum metallization, use of a $PbTiO_3$ seed layer, and fine tuning of annealing conditions for applications in multilayer actuator MEMS technology”, PhD Thesis, University of Maryland, 2014.

[134] K. D. Budd, S. K. Key, and D. A. Payne, “Sol-gel processing of PbTiO3, PbZrO3, PZT, and PLZT thin films”, Br. Ceram. Proc., vol. 36, p. 107, 1985.

[135] F. K. Lotgering, “Topotactical reactions with ferrimagnetic oxides having hexagonal crystal structures—II”, J. Inorg. Nucl. Chem., vol. 16, pp. 100–108, 1960.

[136] M. Birkholz, “Thin film analysis by X-Ray scattering”, Wiley-VCH Verlag GmbH & Co. KGaA, Weinheim, FRG, 2005.

[137] G. R. Fox, “X-Ray diffraction method for determining textured volume fractions in PZT thin films”, MRS Proc., vol. 541, p. 529, 1998.

[138] M. D. Vaudin, and G. R. Fox, “Measuring bimodal crystallographic texture in ferroelectric $PbZr_xTi_{1-x}O_3$ thin films”, MRS Proc., p. 363, 1999.

[139] J. H. Hubbell, and S. M. Seltzer, “Tables of X-ray mass attenuation coefficients and mass energy-absorption coefficients 1 keV to 20 MeV for elements Z=1 to 92 and 48 additional substances of dosimetric interest”, 1995.

[140] D. Y. W. Yu and F. Spaepen, "The yield strength of thin copper films on Kapton", J. Appl. Phys., vol. 95, p. 2991, 2004.

[141] F. Macionczyk and W. Brückner, "Tensile testing of AlCu thin films on polyimide foils." J. Appl. Phys., vol. 86, p. 4922, 1999.

[142] C. F. Herrmann, F. W. DelRio, S. M. George, and V. M. Bright, “Properties of atomic layer deposited Al_2O_3/ZnO dielectric films grown at low temperature for RF MEMS”, Micromach. Microfabr. Process Technol. X, vol. 5715, pp. 159–166, 2005.

[143] J. Y. Li, R. C. Rogan, E. Ustündag, and K. Bhattacharya, "Domain switching in polycrystalline ferroelectric ceramics", Nat. Mater., vol. 4, p. 776, 2005.

[144] T. Tanimoto, K. Yamamoto, and T. Morii, "Nonlinear stress-strain behavior of piezoelectric ceramics under tensile loading", in Proc. 1994 IEEE Int. Symp. Appl. Ferroelectr. (IEEE, 1994), pp. 394–397, 1994.

[145] H. Cao and A.G. Evans, "Nonlinear deformation of ferroelectric ceramics.", J. Am. Ceram. Soc., vol. 76, pp. 890-896, 1993.

[146] F. Li and D. Fang, "Simulations of domain switching in ferroelectrics by a three-dimensional finite element model", Mech. Mater., vol. 36, pp. 959-973, 2004.

[147] C. M. Landis, "On the strain saturation conditions for polycrystalline ferroelastic materials.", J. Appl. Mech., vol. 70, pp. 470-478, 2003.

[148] P. M. Chaplya and G. P. Carman, "Compression of piezoelectric ceramic at constant electric field: energy absorption through non-180 domain-wall motion”, J. Appl. Phys., vol. 90, pp. 1504-1510, 2002.

[149] S. C. Hwang, C. S. Lynch, and R. M. McMeeking, "Ferroelectric/ferroelastic interactions and a polarization switching model”, Acta Metall. Mater., vol. 43, pp. 2073-2084, 1995.

[150] Y. Fotinich and G. P. Carman, "Stresses in piezoceramics undergoing polarization switchings”, vol. 88, pp. 6715-6725, 2016.

[151] F. X. Li and R. K. N. D. Rajapakse, "A constrained domain-switching model for polycrystalline ferroelectric ceramics. Part I: model formulation and application to tetragonal materials”, Acta Mater., vol. 55, pp. 6472-6480, 2007.

[152] W. Yang, H. T. Wang, F. Fang, and Y. Q. Cui, "Unconventional domain band structure at the crack tip in ferroelectric ceramics”, Theor. Appl. Fract. Mech., vol. 37, pp. 397-408, 2001.

[153] T. Mura, “Micromechanics of Defects in Solids”, 2nd ed. Martinus Nijhof, Dordrecht, 1987.

[154] A. E. Romanov, A. Vojta, W. Pompe, M. J. Lefevre, and J. S. Speck, "Domain patterns in (111) oriented tetragonal ferroelectric films.", Phys. Status Solidi, vol. 172, pp.225-253, 1999.

[155] R. Xu, S. Liu, I. Grinberg, J. Karthik, A. R. Damodaran, A. M. Rappe, and L. W. Martin, "Ferroelectric polarization reversal via successive ferroelastic transitions”, Nat. Mater., vol. 14, pp. 79-86, 2015.

[156] B. J. Rodriguez, A. Gruverman, A. I. Kingon, R. J. Nemanich, and J. S. Cross, "Investigation of the mechanism of polarization switching in ferroelectric capacitors by three-dimensional piezoresponse force microscopy”, Appl. Phys. A Mater. Sci. Process, vol. 80, pp.99-103, 2005.

[157] F. Xu, S. Trolier-McKinstry, W. Ren, B. Xu, Z. L. Xie, and K.J. Hemker, "Domain wall motion and its contribution to the dielectric and piezoelectric properties of lead zirconate titanate films", J. Appl. Phys., vol. 89, pp. 1336-1348, 2001.

[158] M. Kohli, P. Muralt, and N. Setter, "Removal of 90° domain pinning in (100) $Pb(Zr_{0.15}Ti_{0.85})O_3$ thin films by pulsed operation", Appl. Phys. Lett., vol. 72, pp. 3217-3219, 1998.

[159] V. Nagarajan, A. Roytburd, A. Stanishevsky, S. Prasertchoung, T. Zhao, L. Chen, J. Melngailis, O. Auciello, and R. Ramesh, "Dynamics of ferroelastic domains in ferroelectric thin films", Nat. Mater., vol.2, pp. 43-47, 2003.

[160] M. J. Hoffmann, M. Hammer, A. Endriss, and D. C. Lupascu, "Correlation between microstructure, strain behavior, and acoustic emission of soft PZT ceramics", Acta Mater. vol. 49, pp. 1301-1310, 2001.

[161] S. S. N. Bharadwaja, F. Griggio, J. Kulik, and S. Trolier-McKinstry, "Highly textured laser annealed $Pb(Zr_{0.52}Ti_{0.48})O_3$ thin films", Appl. Phys. Lett., vol. 99, p. 42903, 2011.

[162] L. Lian, and N. R. Sottos, "Effects of thickness on the piezoelectric and dielectric properties of lead zirconate titanate thin films", J. Appl. Phys., vol. 87, p. 3941, 2000.

[163] W. Fang, and J. A Wickert, "Determining mean and gradient residual stresses in thin films using micromachined cantilevers", J. Micromechanics Microengineering, vol. 6, pp. 301–309, 1996.

[164] S. F. Liu, S. E. Park, T. R. Shrout, and L. Eric Cross, "Electric field dependence of piezoelectric properties for rhombohedral 0.955 $Pb(Zn_{1/3}Nb_{2/3})O_3$ - 0.045 $PbTiO_3$ single crystals", J. Appl. Phys., vol. 85, p. 2810, 1999.

[165] H. G. Yeo, and S. Trolier-McKinstry, "{001} Oriented piezoelectric films prepared by chemical solution deposition on Ni foils", J. Appl. Phys., vol. 116, p. 14105, 2014.

[166] M. Selten, G.A. Schneider, V. Knoblauch, and R.M. McMeeking, "On the evolution of the linear material properties of PZT during loading history-an experimental study", Int. J. Solids Struct., vol. 42, pp. 3953–3966. 2005.

[167] D. Damjanovic, "Hysteresis in piezoelectric and ferroelectric materials." The science of hysteresis, vol. 3, pp. 337-465, 2006.